©Copyright 2022
Jun Hui See Toh

Interaction-driven dynamical delocalization in a kicked one-dimensional ultracold gas

Jun Hui See Toh

A dissertation
submitted in partial fulfillment of the
requirements for the degree of

Doctor of Philosophy

University of Washington

2022

Reading Committee:
Subhadeep Gupta, Chair
Boris Blinov
Mark Rudner

Program Authorized to Offer Degree:
Physics

University of Washington

Abstract

Interaction-driven dynamical delocalization in a kicked one-dimensional ultracold gas

Jun Hui See Toh

Chair of the Supervisory Committee:
Professor Subhadeep Gupta
Department of Physics

This dissertation reports on the experimental observation of interaction-driven dynamical delocalization in a kicked one-dimensional ultracold gas. In the absence of interactions, particles in a one-dimensional disordered medium are localized due to quantum interference as predicted by the Anderson model. The evolution of this well-known localization phenomenon in the presence of interactions has been the subject of intense scrutiny in the past decades, including conflicting theoretical predictions in some cases. Using the quantum kicked rotor (QKR), we engineered the Anderson model in the synthetic momentum space where the equivalent localization phenomenon is termed dynamical localization. However, interaction effects had not been observed in earlier experimental observations of dynamical localization. We detail the implementation of a three-dimensional optical lattice that is used to control the interactions in the system and to realize the QKR Hamiltonian. Using ultracold gases in 1D tubes, we perform a quantum simulation of the QKR Hamiltonian in the presence of interactions and find that interactions destroy the localization and lead to slower-than-linear energy growth or sub-diffusive dynamics. The measured sub-diffusive exponents are not universal or monotonically varying with the various experimental parameters. However, we find that the onset time of delocalization is always shorter with stronger interaction or kick strengths. By temporally modulating the kick strength with incommensurate frequencies, we also engineered higher dimensional Anderson models and observed similar interaction-

driven delocalization phenomena. The metal-insulator Anderson transition in the presence of interactions is also studied in the 3D case with varying kick strength. Our results shed light on interaction-driven transport, in a regime where theoretical approaches are extremely challenging and predict drastically different dynamics.

ACKNOWLEDGMENTS

The past six years in graduate school have been an amazing adventure for me to learn and do physics. I would like to thank those who have supported me throughout this journey.

I thank Deep for the opportunity to work in his research group. I have learned a lot about the physics of ultracold atoms in the past six years. His intuitive explanations of different physics problems have taught me different ways of approaching and thinking about a problem. His insightful feedback and patient guidance have also helped me overcome different experimental hurdles in the lab. I am grateful for his unwavering support throughout the doctoral program.

I worked closely with Alaina Green in the first three years in the lab. I consider myself incredibly lucky to have had the opportunity to learn from Alaina, who is an excellent experimentalist. I learn everything about our machines and equipment from her, and I am thankful for her patient explanations of the various details of our experiments. Alaina is creative and skillful when dealing with a problem with limited resources. I have enjoyed our collaboration in tackling different technical problems of the machine and our coordination in taking data for long hours.

I would also like to thank my other labmates. Xinxin Tang has helped take some of the data of the 1D kicked rotor experiment. I am also thankful for his pretty gif images of the atoms in the early days of the data taking. His quirkiness has also often brought joy to the lab. Nicolas Williams and Carson Patterson who joined our group in recent years have also been extremely helpful in fixing different lasers and setting up optics for the new experiment.

Throughout the six years, I have had the opportunity to work with two post-docs − Ryan Bowler and Katie McCormick. I worked on several electronics projects in my first year and

learned several experimental skills under Ryan's guidance. Katie McCormick who joined us later had helped set up part of the optical lattice and simulated the kicked rotor dynamics. I am thankful for her insightful feedback on the experiment and her effort in organizing the journal club.

I have also enjoyed the wonderful experience of working with many of our amazing undergraduate students including Khang Ton, Frank Fu, Yifei Bai, and Tristan Rojo. Mentoring them and explaining technical details to them have reinforced my physics knowledge. Khang contributed to the lattice optics setup and its electronics. Frank fixed several RF drivers. Yifei was involved in many electronics projects including switch drivers and magnetic field detection circuits. Tristan, who is our REU student, joined the group virtually during the COVID pandemic. He has contributed to the work on the quasiperiodic kicked rotor presented in this thesis. His numerical simulation of the 3D Anderson model guided our experiment. His dedication and determination in tackling challenging tasks have also been inspiring.

I want to thank other group members in the interferometry lab − Katie McAlpine, Daniel Gochnauer, Tahiyat Rahman, and Anna Wirth. They have been a great resource for exchanging ideas and equipment.

I would also like to thank our theory collaborators − Ying Su, Mengxin Du, Xi-Wang Luo, and Chuanwei Zhang at The University of Texas at Dallas. They performed numerical simulations for the work presented in this thesis. I appreciate their meticulousness in dealing with complex simulations. Their useful insights and feedback have also helped us understand the interacting Anderson model better.

Last but not least, I would like to thank my family for their support and encouragement throughout this doctoral program.

TABLE OF CONTENTS

LIST OF FIGURES

Chapter 1

INTRODUCTION

Ultracold atoms provide an excellent platform to study many interesting and scientifically important phenomena in a near-ideal environment. The ultralow temperature suppresses the noise and decoherence of the system, allowing us to probe delicate effects that are otherwise too challenging to observe in other experimental settings. The pure systems prepared using the highly-selective optical transition (internal state preparation) and atom trapping (external state preparation) also enhance the signal-to-noise ratio of the measurement. Furthermore, the efficient production of quantum degenerate gases enables a wide range of studies that require certain macroscopic phase coherence and quantum statistics. The ability to tune the interactions between atoms using Feshbach resonance also facilitates the study of many-body systems. All of these crucial tools and techniques in ultracold atoms empower a plethora of research from the collective dynamics of an ensemble of quantum gases to the motion of a single atom.

With the precise controllability and manipulation of atoms achieved over the past few decades, atomic physicists can now tackle new problems using a bottom-up approach by assembling atoms together either in the form of a molecule or in a crystalline structure. Ultracold molecules can be prepared coherently by sweeping light or magnetic fields in a certain way, and they have rich applications in quantum chemistry, quantum information, and precision measurement. Trapping atoms in a periodic structure using optical lattices enables quantum simulation of condensed-matter many-body systems. This analog quantum simulation of a physical system is extremely useful for problems that are too challenging to be solved numerically using a classical computer. It works by mapping the Hamiltonian of

one complex quantum system to the other Hamiltonian that we can control with the atom assembly.

In this thesis, we will look at a particular kind of quantum simulation where the Anderson Hamiltonian in position space is engineered in the synthetic momentum space to investigate the dynamics in a disordered medium. We achieve this using the quantum kicked rotor technique by loading the ultracold atoms in a periodically-pulsed optical lattice. The flexibility of this method enables us to scale up to higher dimensions easily, instead of adding more optical lattices if the simulation is done in the position space. We will examine an interesting effect called dynamical localization where a system stops absorbing energy after some time even if we keep injecting energy into the system. This is in contrast to the classical case in which we would expect the system to heat up indefinitely. This dynamical localization is simply the Anderson localization in the momentum space, and it arises due to the quantum interference of wave functions in a disordered medium. Anderson physics is extremely rich and has deep connections to different areas of mathematics including random walk, chaos, and fractals. The famous saying in the study of random walk *"A drunk man will find his way home, but a drunk bird may get lost forever"* echoes with the existence of an Anderson metal-insulator transition in three-dimensional space.

The work presented in this thesis investigates the effect of interaction on dynamical localization in different dimensions, a problem that has so far remained unexplored experimentally despite extensively studied theoretically. The first chapter of this thesis gives an overview of the Anderson model and explains the dynamics of a wave packet in different dimensions of a disordered medium. We will show how the quantum kicked rotor can be used to engineer the Anderson Hamiltonian in the synthetic momentum space. We will also give an overview of the different theoretical predictions on the Anderson model with interactions. Chapter 2 describes the basics of optical lattices and Kapitza-Dirac diffraction, which are fundamental to the quantum kicked rotor. Chapter 3 discusses the experimental setup and the implementation of the optical lattices. We will address the design problems and implementation challenges faced while constructing the lattices. After presenting the

optical lattice calibration technique using Kapitza-Dirac diffraction, we show our observation of the superfluid-to-Mott insulator transition in a three-dimensional lattice.

In Chapters 4 and 5, we report on the observation of interaction-driven dynamical delocalization in $d = 1$ and $d = 3$ Anderson models, respectively. We first discuss the details of our system and then present the observation of quantum resonance and anti-resonance of a non-interacting QKR. We then present our observation of interaction-driven delocalization, demonstrating that interactions do indeed destroy dynamical localization. We study the sub-diffusive delocalization dynamics with different experimental parameters. We describe how the amplitude-modulated kick pulses can be used to engineer the Anderson models with arbitrary dimension d. We observe similar delocalization up to $d = 4$ and show how the Anderson transition is affected by the interactions.

The work presented in this thesis sheds light on interaction-driven transport in a disordered medium. We hope that the results shown will motivate other theoretical and experimental studies on this challenging problem. Future detailed studies on the sub-diffusive exponent and the dynamics around the localized-delocalized transition with a larger parameter space would be exciting.

Chapter 2

ANDERSON MODEL AND QUANTUM KICKED ROTOR

In this chapter, we will first present an overall introduction to the Anderson model. We will discuss the relevant condensed matter system and the phenomenon of Anderson localization. We will then introduce the idea of scaling theory to explain how the dynamics of a system differ across dimensions. Particularly, we will see that there exists a metal-insulator transition in a 3D disordered medium. Next, we will briefly discuss the classical kicked rotor and chaos, which will help us understand better the quantum kicked rotor (QKR) presented subsequently. In the section on the quantum kicked rotor, we will introduce several important parameters that will be tuned experimentally later. We will also show how the quantum kicked rotor can be used to engineer the Anderson model by deriving the mapping between the QKR Hamiltonian and the Anderson tight-binding model. The QKR can exhibit dynamical localization, which is simply the Anderson localization in momentum space. Finally, we ask the big question that this work tries to answer: What effect does interaction have on the Anderson model? Specifically, how does interaction affect Anderson localization?

2.1 Anderson Model

Bloch theory predicts that the wavefunction of an electron in a periodic crystal is fully delocalized, i.e., the electron can propagate freely through the crystal [1]. However, it's also known that this theory fails when we consider an imperfect crystal in which the discrete translation symmetry is broken by the disorder arising from impurities or defects. Such an imperfect crystal has a lower electrical conductivity because the electron mobility is restricted. In 1958, Philip W. Anderson explained the dynamics of an electron in an imperfect

crystal by postulating that the energy of each lattice site is altered randomly by the disorder [2]. He approached the problem using the tight-binding approximation with random onsite energy, and this formulation of the problem is what's now called the Anderson model.

The Anderson model has been an important model for describing the physics of a particle in a disordered medium since its formulation decades ago. Anderson's conjecture also predicts the localization of the wavefunction in a disordered medium by considering the scattering of the particle off the random potentials and its interference effects. This treatment also makes the Anderson model one of the physics models that distinguishes quantum mechanics from everyday classical mechanics by considering the electron as a wave. Let us first consider a classical particle scattering off a potential $V(z)$. We know that if the particle's kinetic energy is larger than the potential height, the particle will simply fly over the potential unaffected; otherwise, if its kinetic energy is lower than the potential height, it will simply be reflected off by the potential. Quantum mechanically, however, the particle is treated as a wave, and there is a probability for a particle to tunnel out of the potential. We will then have to consider the transmission and reflection parts of the wavefunction. In a disordered medium, the scattered waves interfere destructively in the forward direction and the amplitude of the total wavefunction decays exponentially, and thus the particle wave is localized [3]. Anderson localization is fundamentally a wave phenomenon and it has been observed with other kinds of waves including light [4–6] and acoustic waves [7].

Next, we will follow the treatment in Ref. [8, 9] to discuss the Anderson localization in systems of different strengths of disorder and different dimensions. The Anderson Hamiltonian is given by

$$H = \sum_n \epsilon_n \hat{c}_n^\dagger \hat{c}_n + t \sum_{<n,m>} \left(\hat{c}_n^\dagger \hat{c}_m + h.c. \right) \tag{2.1}$$

where the onsite energy is $\epsilon_n \in [-W/2, W/2]$ with the disorder parameter W, and t is the tunneling energy. An electron can still hop from site to site even with the disorder, but it needs to overcome the energy difference between different sites. A site with a smaller energy defect ΔE due to the energy shift by the disorder is always more favorable because

the electron can only stay at a site for a time $\tau \sim \hbar/\Delta E \sim \hbar/W$, while the timescale for hopping to a neighbor is $\hbar/t$. Thus, for the case of strong disorder $t \ll W$, the electron can't travel far away from its initial site. The wavefunction will be exponentially localized $\psi \sim e^{-x/\xi}$ where ξ is the localization length.

The case of weak disorder $t \gg W$ is more counter-intuitive because one would think that the electron can now propagate more freely and the dynamics will be more diffusive instead of localized. However, the "Gang of four" − Abrahams, Anderson, Licciardello, Ramakrishnan − later found using the renormalization group arguments that localization can still occur depending on the dimension of the system [10]. Their scaling theory of localization shows that localization always occurs in 1D and 2D systems regardless of the disorder W. For a 3D system, however, localization only occurs above a critical disorder. This separation of localized and delocalized phases allows for the Anderson metal-insulator transition (MIT).

Here we will only give an intuitive explanation of the scaling arguments. Consider a material with length L and cross-section area L^{d-1}, where d is the dimension of the material. Define g as the dimensionless conductance of a material with transmission T,

$$g = \frac{T(L)}{1 - T(L)} \tag{2.2}$$

The scaling theory examines how the conductance g changes with the size L using the parameter $\beta = \frac{d\ln(g)}{d\ln(L)}$. We will first consider the limiting behavior when g is extremely large ($g \to \infty$), i.e. when the disorder is weak and the material is a good conductor. According to Ohm's law, the resistance R of a material with resistivity ρ is

$$R = \rho\frac{L}{A} = \rho\frac{L}{L^{d-1}} \tag{2.3}$$

and thus

$$g \sim bL^{d-2} \tag{2.4}$$

where b is some constant. We then have

$$\lim_{g\to\infty} \beta(g) = \lim_{g\to\infty} \frac{d\ln(g)}{d\ln(L)} = d - 2 \tag{2.5}$$

In the opposite limit when g is vanishing ($g \to 0$), i.e. with a strong disorder, the wavefunction will be exponentially localized and thus

$$g(L) \sim e^{-L/\xi} \tag{2.6}$$

and

$$\frac{d\ln(g)}{d\ln(L)} = \ln(g) = -\frac{L}{\xi} \tag{2.7}$$

which gives

$$\lim_{g\to 0} \beta(g) = \ln(g). \tag{2.8}$$

Figure 2.1 shows the plots of $\beta(g)$ for different dimensions. The equation used for the plot is $\beta(g) = (d-1) - (1+g)\ln(1+g^{-1})$ [9]. Note that this equation and the plots show only the approximation of the conductance of the material, particularly they are most accurate around the two limiting cases we considered above. To obtain the exact conductance of the material, one will have to solve for the wavefunction independently for different dimensions [10].

We can thus see from Fig. 2.1 that $\beta < 0$ for all g for 1D and 2D systems. This means that as the size of the system increases, the conductance will decrease, and thus the system will be an insulator (localized wavefunction) regardless of the disorder. For a 3D system, however, there is a critical point such that $\beta(g_c) = 0$, above which the conductance will increase with the system size, and thus the system becomes a conductor (delocalized wavefunction). This critical point separates the system into metal and insulator states, and therefore there exists a transition between localized and diffusive states for a 3D system − the Anderson metal-insulator transition.

It is challenging to study the Anderson model in condensed matter because one has no direct access to the electronic wavefunction in a crystal, and thus can't directly observe Anderson localization. Also, the material will have to be kept at a very low temperature to suppress decoherence. Therefore, the Anderson model is often studied by engineering and simulating the similar Hamiltonian using another more controllable system. Ultracold

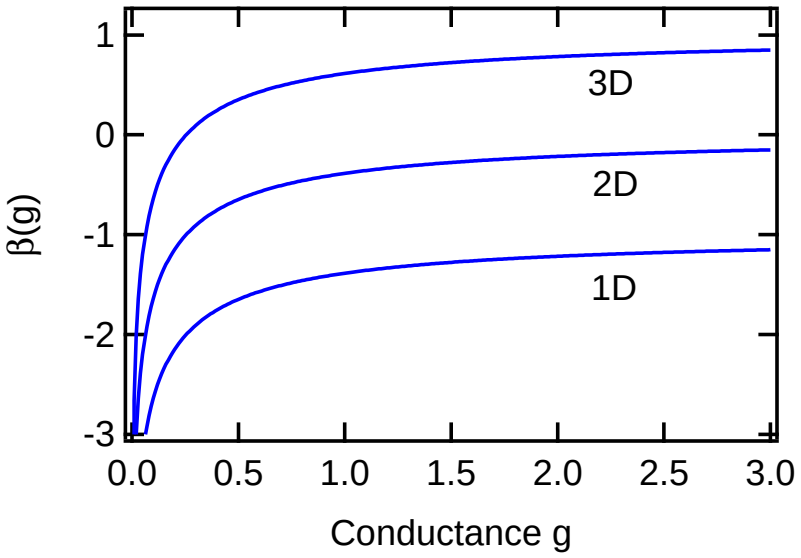

Figure 2.1: Scaling function β for 1-3 dimensions. For 1D and 2D systems, the scaling function is always negative, i.e. $\beta < 0$ for all g. This means that the system would be an insulator since the conductance would decrease as $L \to \infty$. For 3D and higher dimensional systems, however, there is a critical point such that $\beta(g_c) = 0$ marks a metal-insulator phase transition.

atom systems are excellent platforms for quantum simulations for condensed matter systems [11, 12]. For the case of the Anderson model, Anderson localization had been observed experimentally in 1D to 3D systems by observing the spread of an atom cloud in a speckle potential which simulates the disordered medium [13–15]. Such a method allows one to examine directly the wavefunction in real space, but the implementation becomes more and more difficult for higher dimensional systems. The work presented in this thesis uses another approach for studying the same physics in the synthetic dimension of momentum space by using a system called the quantum kicked rotor (QKR). It provides more flexibility in simulating higher dimensional disordered systems and allows direct access to the momentum wavefunction. This method also allows the observation of dynamical localization – the

equivalent of Anderson localization in momentum space.

2.2 Classical Kicked Rotor

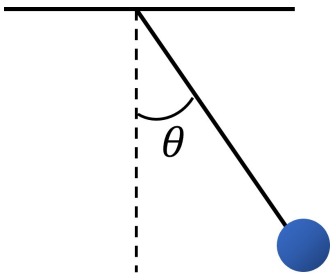

Figure 2.2: Classical swinging pendulum. A swinging pendulum is the classical analog of the quantum kicked rotor if the gravitational potential is pulsing on and off.

Before we discuss the details of the quantum kicked rotor, let us first take a look at its classical analog − a kicked swinging pendulum, as shown in Fig 2.2. If we ignore the kicking part and consider just a classical swinging pendulum for now, we can write the Hamiltonian of the system as

$$H = \frac{P_\theta^2}{2ml^2} - mgl\cos\theta \tag{2.9}$$

where P_θ is the angular momentum. The first term is the kinetic energy of a general rotor, and hence the name "kicked rotor". We can express it in terms of the moment of inertia $I = ml^2$. The second term is the potential energy term due to the gravitational potential. If we now consider the gravity pulsing off and on at some period T, we then have a classical kicked rotor Hamiltonian

$$H = \frac{P_\theta^2}{2I} - V_0\cos\theta\sum_{n=1}\delta(t - nT) \tag{2.10}$$

where $V_0 = mgl$ and n is the number of pulses. Multiplying through by T^2/I, we have the dimensionless Hamiltonian

$$H = \frac{\rho^2}{2} - \kappa\cos\theta\sum_{n=1}\delta(\tau - n) \tag{2.11}$$

where $\kappa = V_0 T^2/I$ is the stochasticity parameter and $\rho = P_\theta T/I$ is the dimensionless momentum [16]. The classical kicked rotor is a system that has been extensively used in the study of classical chaos. To understand the dynamics of the system, one can simplify the equations of motion of the system to a Chirikov's standard map given by

$$\begin{aligned} \theta_n &= \theta_{n-1} + \rho_n \pmod{2\pi} \\ \rho_n &= \rho_{n-1} - \kappa \sin\theta_{n-1} \pmod{2\pi} \end{aligned} \tag{2.12}$$

Because of the periodicity of $\sin\theta$, we consider only the $[0,2\pi]$ range for θ and ρ, and the dynamics can be considered on a torus. When the stochasticity parameter κ is large enough, the outcome of the term with $\sin\theta_{n-1}$ essentially becomes random for successive n values and results in random dynamics. We can see from the phase space plots (Fig. 2.3) that for small κ the dynamics retain some of the oscillatory behavior as shown by islands of stability. These islands of stability gradually shrink as κ grows, and eventually the dynamics become completely chaotic for $\kappa > 5$.

Note that it is easy for one to think that chaotic dynamics are completely random, but when we talk of chaos, we have to distinguish between "predictability" and "determinism" [16]. Chaos often refers to some dynamics that have "deterministic randomness" [17]. The dynamics are unpredictable because they are highly sensitive to the initial conditions. This can be seen by simulating the dynamics on different computers. Because of the different numerical rounding and storing methods of double precision numbers of different computer processors, the results can differ vastly after some large number of iterations. This is similar to how Lorentz discovered the butterfly effect (a more poetic term for chaos) when he changed the initial conditions for his weather simulation slightly [18]. However, once the initial conditions are known, the dynamics are completely determined by the standard map (Eq. 2.12).

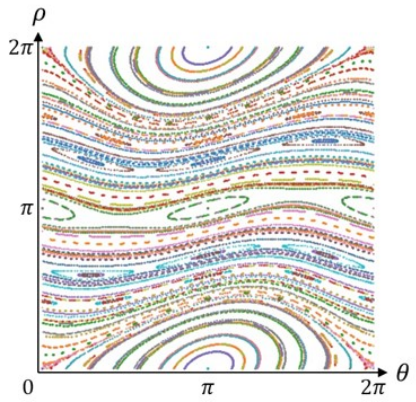

(a) $\kappa = 0.5$

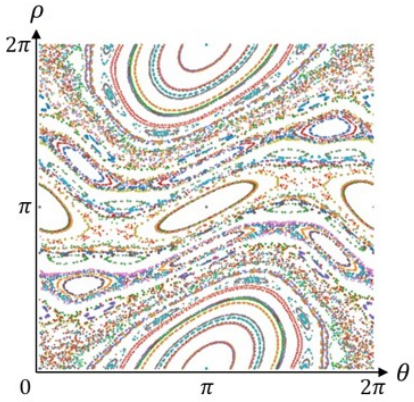

(b) $\kappa = 1$

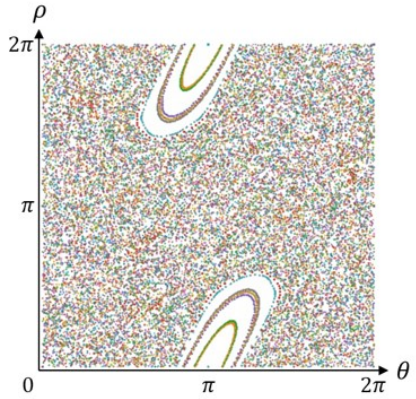

(c) $\kappa = 3$

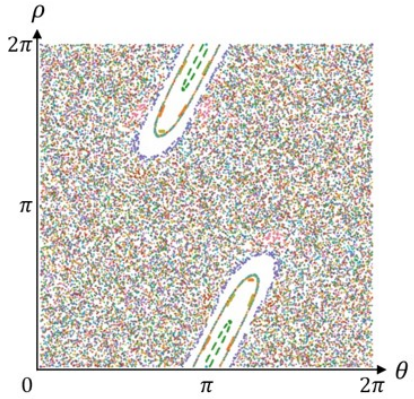

(d) $\kappa = 4$

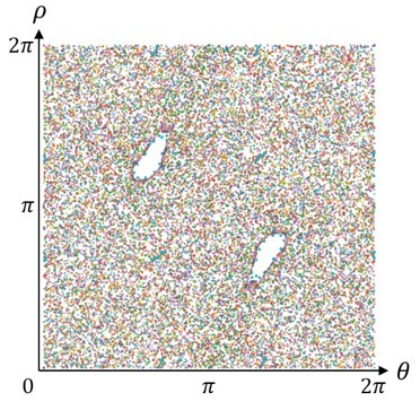

(e) $\kappa = 5$

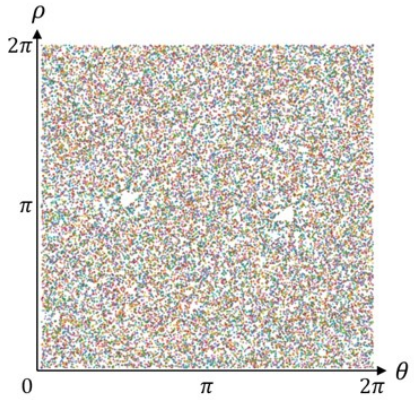

(f) $\kappa = 6$

Figure 2.3: Dynamics of the classical kicked rotor in phase space for various κ.

2.3 Quantum Kicked Rotor (QKR)

Let us now turn to the quantum version of the kicked rotor. The quantum kicked rotor has been extensively studied with ultracold neutral atoms and dynamical localization has been observed [8, 19–30]. A quantum kicked rotor is realized with an atom cloud loaded into a periodically pulsing optical lattice. Such a setup is common and easily implemented in any cold atom lab. The quantum kicked rotor has been a paradigmatic system to simulate the Anderson model because of its flexibility and simplicity. The QKR allows one to control the different parameters such as the tunneling rate and disorder of the Anderson model by controlling the kick strength and kick period. More interestingly, because the Anderson model is engineered in the synthetic momentum dimension, it also allows experimental simulation of the Anderson model in arbitrary dimension by simply modulating the amplitude of the pulses. Due to the low temperature of ultracold atoms, the QKR also has the advantage that the decoherence is low and the different momenta after the kicks are better resolved.

The Hamiltonian of a non-interacting BEC in a pulsed standing wave can be written as

$$\begin{aligned} H &= \frac{P^2}{2m} - V_{\text{lat}} \cos^2 k_L z \sum_{n_p=1}^{N} \delta_{t_p}(t - n_p T) \\ &= \frac{P^2}{2m} - \frac{V_{\text{lat}}}{2} \cos 2k_L z \sum_{n_p=1}^{N} \delta_{t_p}(t - n_p T) \end{aligned} \tag{2.13}$$

where $V_{\text{lat}} = 4V_{\text{dip}}$ is the lattice depth, T is the kicked period, and t_p is the pulse length. The difference between this Hamiltonian compared with the classical one is that the position and momentum variables are now quantum operators. The pulse function $\delta_{t_p}(\tau) = 1/t_p$ if $|\tau| \leq t_p/2$ and zero otherwise, and tends to the Dirac δ function as $t_p \to 0$. We will use the following dimensionless parameters to rescale the Hamiltonian

$$\theta = 2k_L z \tag{2.14}$$

$$\tau = t/T \tag{2.15}$$

$$p = \frac{\bar{k}}{2\hbar k_L} P \tag{2.16}$$

$$\bar{k} = 8\omega_{\text{rec}} T \tag{2.17}$$

where $\omega_{\text{rec}} = \hbar k_L^2/2m$ is the recoil frequency. The dimensionless reduced Planck constant $\bar{k}$ also satisfies the commutation relation $[\theta, p] = i\bar{k}$. Eq. 2.13 then becomes

$$H = \left(\frac{2\hbar k_L}{\bar{k}}\right)^2 \frac{p^2}{2m} - \frac{V_{\text{lat}}}{2} \cos\theta \sum_{n_p=1}^{N} \delta(\tau - n_p)$$

Multiply through by $\bar{k}T/\hbar$, we then get the dimensionless QKR Hamiltonian

$$H = \frac{p^2}{2} - K \cos\theta \sum_{n_p=1}^{N} \delta(\tau - n_p) \tag{2.18}$$

where

$$K = \bar{k}\phi_{\text{kick}} \tag{2.19}$$

$$\phi_{\text{kick}} = \frac{V_{\text{lat}} t_p}{2\hbar} \tag{2.20}$$

are the kick strength and the pulse area, respectively, and n_p is the pulse number. Note that due to the finite and short ($t_p \ll T$) pulses, the kick strength K had absorbed an additional factor of t_p/T from the dimensionless transformation of the delta function.

Next, we will show how the quantum kicked rotor can be used to engineer the Anderson model by showing the mapping of the QKR hamiltonian to the Anderson tight-binding model following the treatment in [29, 31]. From Eq. 2.18, we can see that the unitary evolution from one kick to the next is

$$U = e^{-iK\cos\theta/\bar{k}} e^{-ip^2/2\bar{k}}. \tag{2.21}$$

The eigenstates of this evolution operator are Floquet states $|\phi\rangle$ with quasienergy ω, defined modulo 2π

$$U|\phi_\omega\rangle = e^{-i\omega}|\phi_\omega\rangle \tag{2.22}$$

Now, we rewrite the kick operator as

$$e^{-iK\cos\theta/\hbar} = \frac{1+iW(\theta)}{1-iW(\theta)} \tag{2.23}$$

with

$$W(\theta) = -\tan\left(K\cos\theta/2\hbar\right) \tag{2.24}$$

Since the function $W(\theta)$ is periodic, it can be expressed as the Fourier series

$$W(\theta) = \sum_r W_r e^{ir\theta} \tag{2.25}$$

Similarly, the kinetic part can be written as

$$e^{-i(p^2/2\hbar-\omega)} = \frac{1+iV}{1-iV} \tag{2.26}$$

where V is diagonal in the momentum eigenbasis $|m\rangle = |p = m\hbar\rangle$. Next, we make the following expansion in the momentum eigenbasis

$$\frac{1}{1-iW(\theta)}|\phi_\omega\rangle = \sum_m \Phi_m|m\rangle \tag{2.27}$$

The eigenequation for the Floquet state can then be written as

$$\epsilon_m\Phi_m + \sum_{r\neq 0} W_r\Phi_{m-r} = -W_0\Phi_m \tag{2.28}$$

with $\epsilon_m = \tan\left[\frac{1}{2}(\omega - m^2\hbar/2)\right]$. Equation (2.28) is now in the form of a tight-binding model with onsite energy ϵ_m, hopping element W_r, and eigenenergy W_0. As an intuitive explanation of the mapping between the kicked rotor and the Anderson tight-binding model, we can see that for a fixed $\hbar$, the kick strength K corresponds to the tunneling energy between sites given by Eq. 2.24, while the phase accumulated by atoms of different momenta corresponds to the disorder in each site, as illustrated in Fig. 2.4. Because of the tangent function in the onsite energy term ϵ_m, the resulting distribution of the onsite energies for a range of m values is pseudorandom, which has been shown to be enough to mimic the disorder in Anderson model [32]. However, we note that for the case when $\hbar$ is a rational multiple of 2π, the ϵ_m will be periodic in m and thus is no longer pseudorandom. These special cases are known as the quantum resonances of the kicked rotor, where the states are delocalized.

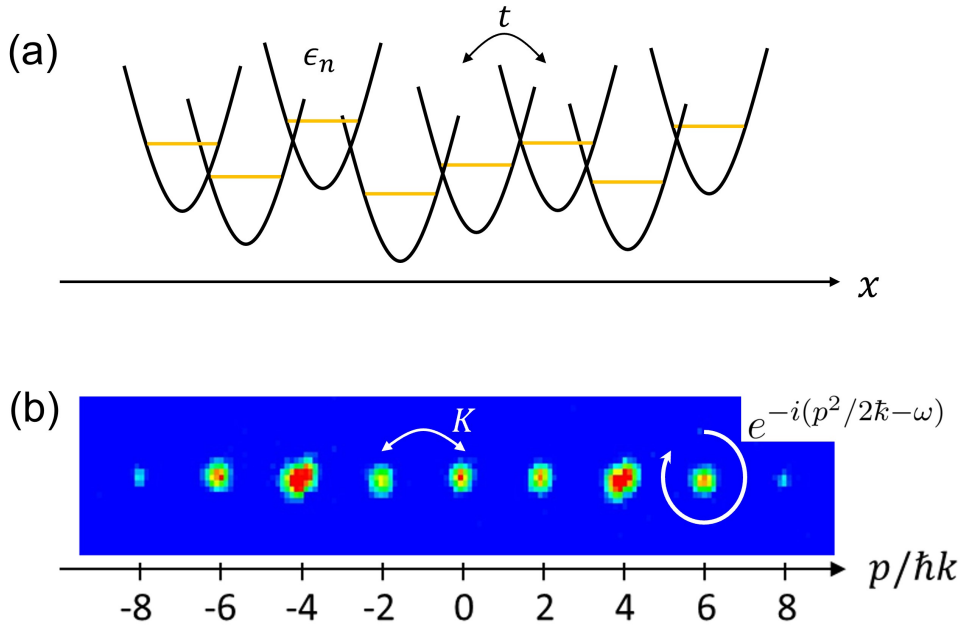

Figure 2.4: Correspondence of the quantum kicked rotor (QKR) and Anderson tight-binding model. (a) In the Anderson tight-binding model, the disorder in each lattice site in position space leads to different onsite energies ϵ_n. A particle can hop between different sites with tunneling rate t. (b) An absorption image of a quantum kicked rotor (QKR) showing the diffraction pattern of the BEC after some kicks. The population in each order of diffraction depends on the kick strength K, and each momentum space lattice site will accumulate a phase that is a function of its momentum during the free evolution time in between kicks.

2.4 Effect of Interactions on the Anderson Model

The Anderson model has been studied heavily both theoretically and experimentally over the past few decades. Experimentally, both Anderson localization in position space and dynamical localization in momentum space [19–24] have been observed. The different factors of parameters affecting the dynamical localization has also been investigated using the quantum kicked rotor [24, 26, 33, 34]. Besides, the Anderson metal-insulator transition has also been observed recently [27, 29, 30]. Despite the extensive study on the Anderson model, the effect of interaction on the dynamical localization remains unexplored experimentally. Although many different theoretical studies have been carried out, the different approximations, models, and numerical methods applied led to vastly different results. Most theories predict that the interactions would destroy dynamical localization, while some predicts that localization should persist if the atoms are in a ring trap [35] or in the regime of few body limit [36].

The delocalization dynamics are predicted to take the power-law form $E \sim t^{\alpha}$. For the theories that predict delocalization, the predicted subdiffusion exponent α also differs significantly. Using the mean-field theory and argument based on the Chirikov resonance overlapping criterion, Ref. [37] showed that the subdiffusion exponent is universally 0.4. On the other hand, Ref. [38] used mean field theory and techniques of averaging and local derivatives on logarithmic scales to show that the subdiffusion exponent is 1/3 for weak chaos regime but 1/2 for the intermediate strong-chaos regime. Ref. [39] approached the problem starting from coupled quantum kicked rotors, and then by mapping the infinite range coupled QKR over an infinite range coupled interacting bosonic particles, they found the subdiffusion exponent to be 0.6. Ref. [40] compared the results obtained from exact mean-field theory, local momentum approximation (LMA), and phase averaging approximation (PAA), and found that not only is the subdiffusion exponent not universal, but it can span over the range of $0.25 - 1.0$. For the interaction effect on Anderson transition, Ref. [41] predicts that with the presence of interaction, the initially localized regime will be delocalized with

a subdiffusion exponent of 0.4, while the initially delocalized regime will remain unaffected [42].

Our work presented here shows the first experimental study of the interaction effect on dynamical localization and Anderson transition. We found that interaction indeed destroys dynamical localization. We probe the subdiffusion exponent for different interaction strengths, kick strengths, and modulation strengths. Our results show that the delocalization dynamics have exponent ranges over $0.3 - 1.0$ with no obvious dependence on the different experimental parameters. Our work will illuminate further detailed studies, both theoretical and experimental, on the effect of interactions on the Anderson model.

Chapter 3

OPTICAL LATTICE

Harmonic optical dipole traps (ODT) and sinusoidal optical lattices are the primary optical potentials we use throughout the experiments described in this thesis. In this chapter, we will discuss in detail the optical potential of these traps and the behavior of atoms confined in them. We will first review the light shift of a 2-level atom in a far-detuned laser field and the basics of the optical dipole trap that can be produced at the focus of such a laser field. We will derive its optical potential and trapping frequencies. We then apply a similar derivation for one and two-dimensional optical lattices and describe the behavior of ultracold atoms confined therein. We will look particularly at the band structure of atoms in a periodic potential and the strongly-interacting 1D gas, which is also known as the Tonks-Girardeau gas. We will then examine the theory of Kapitza-Dirac (KD) diffraction of atoms in a pulsed 1D optical lattice to understand the transfer of amplitudes between different momentum states during each kick of the quantum kick rotor.

3.1 AC Stark Shift

Atom trapping in optical dipole potentials requires far-detuned light. In this section, we will review the principles of the AC Stark shift to lay the foundation for discussing such traps. Here we will consider the atom-light interaction when atoms are placed in a light field with a frequency far-detuned from resonance. The electric field of the light will induce an oscillating electric dipole moment in the atoms, and the interaction between this dipole moment with the electric field will shift the energy levels of the atoms.

Consider a 2-level atom placed in a far-detuned light field as illustrated in Fig. 3.1. States $|1\rangle$ and $|2\rangle$ are separated by a frequency ω_0, and the light field has frequency ω and detuning

$\Delta = \omega - \omega_0$.

The interaction between the light field $E_0 \cos\omega t$ and the induced dipole can be written as

$$H_{\text{int}} = -exE_0 \cos\omega t = -\frac{exE_0}{2}\left(e^{i\omega t} + e^{-i\omega t}\right). \tag{3.1}$$

The overall Hamiltonian $H = H_0 + H_{\text{int}}$ of the system in the semi-classical dressed-state picture is then [43]

$$H = \hbar \begin{pmatrix} 0 & \Omega/2 \\ \Omega/2 & \Delta \end{pmatrix} \tag{3.2}$$

where we have defined the Rabi frequency Ω as $\hbar\Omega = -e\langle 1|x|2\rangle E_0$. Solving the Hamiltonian we get eigenenergies $\epsilon_\pm$ and eigenstates $\Phi_\pm$

$$\epsilon_\pm = \frac{\hbar}{2}\left(\Delta \pm \sqrt{\Delta^2 + \Omega^2}\right) \tag{3.3}$$

$$\Phi_+ = \sin\theta|1\rangle + \cos\theta|2\rangle \tag{3.4}$$

$$\Phi_- = \cos\theta|1\rangle - \sin\theta|2\rangle\ . \tag{3.5}$$

where

$$\sin 2\theta = \frac{\Omega}{\sqrt{\Omega^2 + \Delta^2}} \quad , \quad \cos 2\theta = \frac{\Delta}{\sqrt{\Omega^2 + \Delta^2}}. \tag{3.6}$$

In the limit of large detuning ($\Delta \gg \Omega$), we can simplify Eq. 3.3 and see that the light shift experienced by each unperturbed state is

$$\hbar\delta_{\text{light}} \simeq \frac{\hbar\Omega^2}{4\Delta}\,. \tag{3.7}$$

Equation. 3.7 is also the dipole potential felt by the atoms in the light field. When expressed in terms of intensity, Eq. 3.7 provides a quick estimate of the potential depth because we can directly measure the optical power of a light beam in the lab.

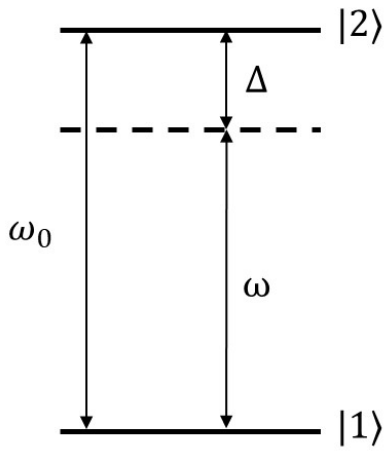

Figure 3.1: Two-level atom interacting with a light field. A two-level atom consists of state $|1\rangle$ and $|2\rangle$ with resonance frequency ω_0. The far-detuned light field has frequency ω and detuning $\Delta = \omega - \omega_0$.

3.2 One-Dimensional Optical Dipole Trap

An optical dipole trap (ODT) is an essential tool in many AMO experiments. In essentially all experiments, atoms are not cold enough to reach quantum degeneracy after the usual laser cooling process in the magneto-optical trap (MOT). In this case, atoms are often transferred into an ODT for evaporative cooling. An ODT can be simply set up by focusing a laser beam onto the atoms. As mentioned before, the electric field will polarize the atoms and induce an electric dipole moment in the atoms; these dipole moments in turn will get attracted by the electric field and thus the atoms are trapped at the focus of the light beam.

We now derive the potential of an ODT and its trapping frequencies, and this will serve as the basis of a similar derivation for optical lattices.

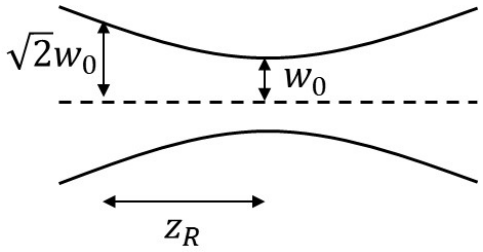

Figure 3.2: Gaussian beam. A Gaussian beam with beam waist w_0 has a beam size of $\sqrt{2}w_0$ at the Rayleigh range z_R.

Consider a circular Gaussian beam (Fig. 3.2) with power P and intensity

$$I(x,y,z) = \frac{2P}{\pi w(z)^2} e^{-\frac{2(x^2+y^2)}{w(z)^2}} \tag{3.8}$$

where the beam waist is $w(z) = w_0\sqrt{1+z^2/z_R^2}$ with value w_0 at the origin and Rayleigh range $z_R = \pi w_0^2/\lambda$. The dipole potential can be expressed as

$$V_{\text{dip}}^{\text{1D}}(x,y,z) = -\frac{\alpha(\lambda)}{2\epsilon_0 c} I(x,y,z) = -\frac{\alpha(\lambda)}{2\epsilon_0 c}\frac{2P}{\pi w(z)^2} e^{-\frac{2(x^2+y^2)}{w(z)^2}} \tag{3.9}$$

$$= \frac{V_{\text{dip}}}{1+z^2/z_R^2} e^{-\frac{2(x^2+y^2)}{w(z)^2}} \tag{3.10}$$

where the potential depth is

$$V_{\text{dip}} = -\frac{\alpha(\lambda)}{2\epsilon_0 c}\frac{2P}{\pi w_0^2} \tag{3.11}$$

with polarizability α, laser wavelength λ, speed of light c, and vacuum permittivity ϵ_0. The polarizability of Yb in a 1064 nm laser, which is our ODT laser wavelength, is 3.7×10^{-37} m^{2}s. Writing the potential in a Taylor series under the conditions $z \ll z_R$ and $r^2 = x^2 + y^2 \ll w_0^2$, we have

$$V_{\text{dip}}^{\text{1D}}(x, y, z) \approx V_{\text{dip}}\left[1 - \frac{2r^2}{w_0^2} - \left(\frac{z}{z_R}\right)^2\right] \tag{3.12}$$

Comparing this to a harmonic oscillator potential, we obtain the radial/transverse and axial trap frequencies respectively as

$$\omega_r = \sqrt{\frac{4V_{\text{dip}}}{mw_0^2}} \quad , \quad \omega_z = \sqrt{\frac{2V_{\text{dip}}}{mz_R^2}} \tag{3.13}$$

Note that in the limit of large detuning, Eq. 3.11 can also be written as $\hbar\Omega^2/4\Delta$ (Eq. 3.7), which is the light shift experienced by the atoms.

When deciding on a laser wavelength for an ODT, one also has to consider the spontaneous scattering rate of the atoms in the laser field, given by [43]

$$R_{\text{scatt}} = \frac{\Gamma}{2}\frac{s}{1 + s + (2\Delta/\Gamma)^2)} \simeq \frac{\Gamma}{8}\frac{\Gamma^2}{\Delta^2}\frac{I}{I_{\text{sat}}} \tag{3.14}$$

where Γ is the linewidth of the transition, I is the intensity of the light field, $I_{\text{sat}} = \frac{\hbar\omega^3\Gamma}{12\pi c^2}$ is the saturation intensity, and $s = I/I_{\text{sat}}$. The last term is obtained using the large detuning approximation. Combining Eq. 3.14 and Eq. 3.7, we get

$$\frac{R_{\text{scatt}}}{V_{\text{dip}}/\hbar} = \frac{\Gamma}{\Delta}. \tag{3.15}$$

From this, we can see that it is important to have a large detuning to reduce the spontaneous scattering rate, but the laser intensity needs to be increased to compensate for the change in the trap depth. From Eq. 3.13, it can also be shown that the aspect ratio of a single-beam optical dipole trap is

$$\frac{\omega_r}{\omega_z} = \frac{\sqrt{2}z_R}{w_0} = \frac{\sqrt{2}\pi w_0}{\lambda}. \tag{3.16}$$

For our ODT, this is estimated to be 125 with $w_0 = 30$ μm and $\lambda = 1064$ nm, which is highly anisotropic. To have better control of the evaporative cooling at low trap depth, we use a crossed-beam configuration for our ODT setup. We intersect the first ODT beam with a second beam at some angle to provide additional confinement along the axial direction. The readers are encouraged to refer to Richard Roy's works [44, 45] for more details on the ODT setup for our experiment.

3.3 One-Dimensional Optical Lattice

An optical lattice is a standing light wave that forms a periodic potential, and atoms can be trapped at the antinodes of the standing wave for a red-detuned lattice. It can be set up by interfering two counter-propagating lasers of the same polarization. Optical lattices have been an excellent platform for simulating condensed matter physics because atoms can be trapped in a crystalline structure and the systems are highly controllable. Compared to a typical solid-state crystal, optical lattices allow experimentalists to study condensed matter physics in an ultracold and defect-free environment. Tunneling and interactions can also be controlled through different lattice parameters, and by using a different number of laser beams in different configurations, one can construct different types of optical lattices such as square lattices, triangular lattices, and hexagonal lattices of different dimensions. In this section, we will consider a one-dimensional optical lattice that forms an array of 2D pancake-like traps as illustrated in Fig. 3.3.

Consider two counter-propagating beams of linearly-polarized light with wavenumber k_L producing a standing wave with an electric field

$$E = E_0 \left[\cos(\omega t - k_L z) + \cos(\omega t + k_L z)\right] \tag{3.17}$$

$$= 2E_0 \cos(k_L z)\cos(\omega t) \tag{3.18}$$

This means that the peak intensity of two counter-propagating beams forming an optical lattice is four times that of a single beam. Specifically,

$$I_{\text{lat}}^{\text{1D}} = \frac{8P}{\pi w(z)^2} e^{-\frac{2r^2}{w(z)^2}} \cos^2 k_L z = 4I_{\text{dip}}^{\text{1D}} \cos^2 k_L z \tag{3.19}$$

Figure 3.3: One-dimensional optical lattice. A one-dimensional optical lattice is formed by overlapping two linearly-polarized laser beams propagating in opposite directions. The resulting optical potential is a stack of 2D pancake-like traps.

where I_{dip} is the intensity of a single Gaussian beam, which is simply Eq. 3.8. The dipole potential of the optical lattice is then

$$\begin{aligned} V_{\text{lat}}^{\text{1D}}(x,y,z) &= -\frac{\alpha(\lambda)}{2\epsilon_0 c} I(x,y,z) = -\frac{\alpha(\lambda)}{2\epsilon_0 c}\frac{8P}{\pi w(z)^2} e^{-\frac{2r^2}{w(z)^2}} \cos^2 k_L z \\ &= \frac{4V_{\text{dip}}}{1+z^2/z_R^2} e^{-\frac{2r^2}{w(z)^2}} \cos^2 k_L z \\ &= \frac{V_{\text{lat}}}{1+z^2/z_R^2} e^{-\frac{2r^2}{w(z)^2}} \cos^2 k_L z \end{aligned} \tag{3.20}$$

where $V_{\text{lat}} = 4V_{\text{dip}}$. The peak lattice potential is four times that of the single-beam optical dipole trap. After Taylor expanding the potential under the conditions $z \ll z_R$ and $r^2 \ll w_0^2$, we get

$$\begin{aligned} V_{\text{lat}}^{\text{1D}} &\approx V_{\text{lat}} \left[1 - \frac{2r^2}{w_0^2} - \left(\frac{z}{z_R}\right)^2\right] \left[1 - (k_L z)^2\right] \\ &\approx V_{\text{lat}} \left[1 - \frac{2r^2}{w_0^2} - \left(\frac{1}{z_R^2} + k_L^2\right) z^2\right], \end{aligned}$$

and comparing this to a harmonic oscillator potential we get the trap frequencies to be

$$\omega_z = \sqrt{\frac{2V_{\text{lat}}}{m}\left(\frac{1}{z_R^2} + k_L^2\right)} \approx \sqrt{\frac{2V_{\text{lat}}k_L^2}{m}} \quad , \quad \omega_r = \sqrt{\frac{4V_{\text{lat}}}{mw_0^2}}\,. \tag{3.21}$$

It is conventional to define the dimensionless lattice depth parameter $s = V_{\text{lat}}/E_{\text{rec}}$ where $E_{\text{rec}} = \hbar\omega_{\text{rec}} = \frac{\hbar^2 k_L^2}{2m}$ is the recoil energy. The transverse and radial trap frequencies can then

be expressed as

$$\omega_z = 2\omega_{\rm rec}\sqrt{s} \qquad , \qquad \omega_r = \frac{\sqrt{2}\lambda}{\pi w_0}\omega_{\rm rec}\sqrt{s}\ . \tag{3.22}$$

3.3.1 Band structure

As in any periodic potential, the dispersion relation of atoms in an optical lattice is also modified depending on the lattice depth. To understand the band structure of a periodic potential, we have to solve the following Schrodinger equation [46]

$$-\frac{\hbar^2}{2m}\frac{d^2\psi(x)}{dx^2} + V(x)\psi(x) = E\psi(x) \tag{3.23}$$

where $V(x) = V_{\rm lat}\cos^2 kx$. According to Bloch's theorem,

$$\psi_q^{(n)}(x) = e^{iqx/\hbar}u_q^{(n)}(x) \tag{3.24}$$

$$u_q^{(n)}(x+a) = u_q^{(n)}(x) \tag{3.25}$$

where $a = \pi/k = \lambda/2$. Here we will refer to the new quantum number q as the quasi-momentum and n as the band index. Plugging Eq. 3.25 into Eq. 3.23, the problem reduces to solving the Hamiltonian [46]

$$\left[\frac{(p+q)^2}{2m} + V(x)\right] u_q^{(n)}(x) = E_q^{(n)}u_q^{(n)}(x). \tag{3.26}$$

Because both the potential $V(x)$ and functions $u_q^{(n)}(x)$ are periodic with the same periodicity a, we can write them in the form of Fourier sums

$$V(x) = \sum_r V_r e^{i2rkx} \tag{3.27}$$

$$u_q^{(n)}(x) = \sum_l c_l^{(n,q)} e^{i2lkx} \tag{3.28}$$

with some integers l and r. The kinetic and potential energy terms can then be written as

$$V(x)u_q^{(n)}(x) = \sum_l\sum_r V_r e^{i2(r+l)kx}c_l^{(n,q)} \tag{3.29}$$

$$\frac{(p+q)^2}{2m}u_q^{(n)}(x) = \sum_l \frac{(2\hbar kl+q)^2}{2m}c_l^{(n,q)}e^{i2lkx} \tag{3.30}$$

The optical lattice potential can also be written in terms of exponentials (for two counter-propagating plane waves)

$$V(x) = V_{\text{lat}} \cos^2 kx = \frac{1}{4} V_{\text{lat}} \left(e^{2ikx} + e^{-2ikx} + 2 \right). \tag{3.31}$$

Putting all these together and comparing the same e^{2iklx} terms, we can simplify the Hamiltonian further and see that only the diagonal and the first off-diagonal elements are nonzero

$$\sum_l H_{l,l'} c_l^{(n,q)} = E_q^{(n)} c_l^{(n,q)} \tag{3.32}$$

$$H_{l,l'} = \begin{cases} (2l + q/\hbar k)^2 E_r & \text{if } l = l' \\ -V_{\text{lat}}/4 & \text{if } |l - l'| = 1 \\ 0 & \text{otherwise.} \end{cases} \tag{3.33}$$

We can solve this simplified Hamiltonian numerically and obtain its eigenfunctions and eigenenergies. Fig. 3.4 shows the eigenenergies of the Hamiltonian for lattice depths solved using Mathematica. The plot shows the band structure in the first Brillouin zone, and for each q, there are infinitely many solutions with different discrete values n. This is the reason the label n is called the band index and the entire spectrum of solutions is the band structure of the system. As the lattice depth is increased, the different bands repel each other and bandgaps are opened up. We can see from the plot that as the lattice depth is increased, the bandgap increases while the bandwidth decreases.

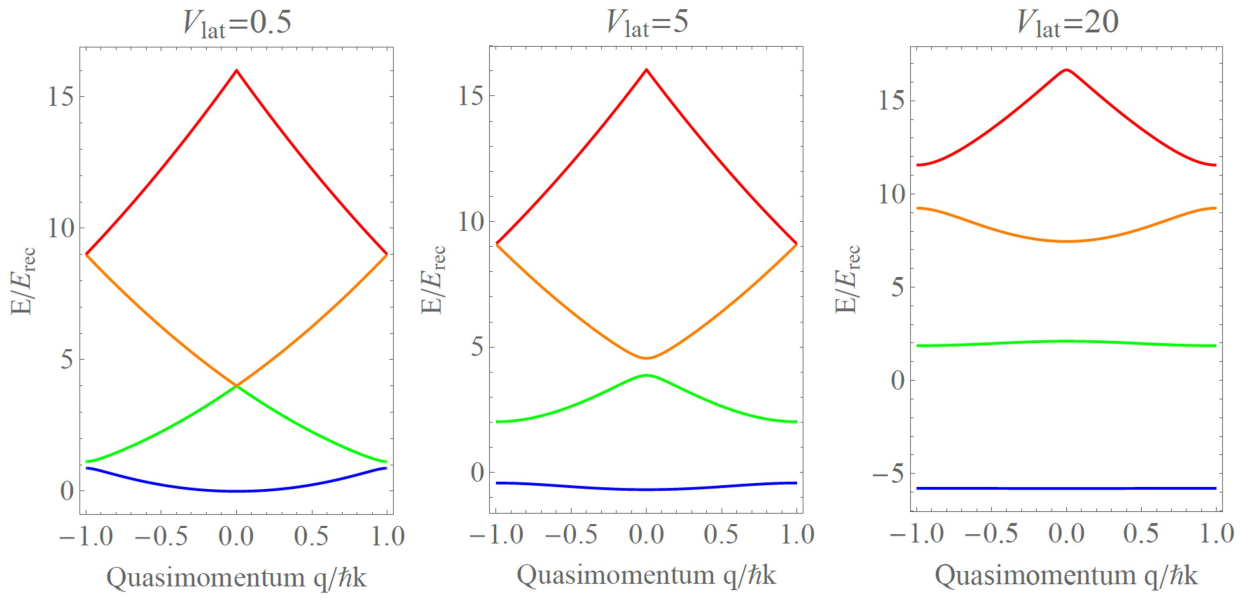

Figure 3.4: Band structure of atoms in a periodic potential plotted in the first Brillouin zone. As the lattice depth is increased, the bandgap increases and the bandwidth decreases.

3.4 Two-dimensional Optical Lattice

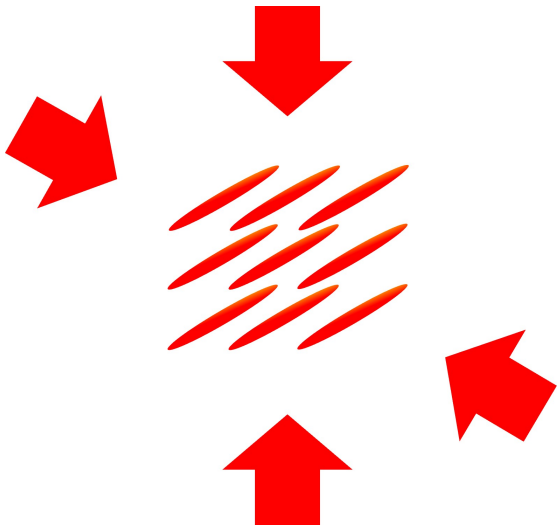

Figure 3.5: Two-dimensional lattice. A two-dimensional lattice is formed by two counter-propagating light waves along two orthogonal directions. The resulting optical potential is an array of 1D tubes.

A two-dimensional optical lattice can be set up by simply intersecting two one-dimensional lattices at some angle. For our experiments, the two lattices are set up with a relative angle of about 90 degrees to form an array of 1D tubes, as shown in Fig. 3.5. We will follow the same method as before to derive the optical potential of a two-dimensional lattice and its trapping frequencies.

Consider two pairs of counter-propagating beams, one along the x-axis and one along the y-axis. This two-dimensional lattice will form an array of 1D tubes with the axial direction along the z-axis.

$$I_{\text{lat}}^{\text{2D}}(x,y,z) = \frac{8P}{\pi w(x)^2} e^{-\frac{2(y^2+z^2)}{w(x)^2}} \cos^2 k_L x + \frac{8P}{\pi w(y)^2} e^{-\frac{2(x^2+z^2)^2}{w(y)^2}} \cos^2 k_L y \tag{3.34}$$

where $w(j) = w_j\sqrt{1+j^2/j_R^2}$ with beam waist w_j and Rayleigh range $j_R = \pi w_j^2/\lambda$ for the beam along the j^{th} direction.

Following the same procedure in Eq. 3.20, the two-dimensional lattice potential can then be expressed as

$$\begin{aligned} V_{\text{lat}}^{\text{2D}} &= -\frac{\alpha(\lambda)}{2\epsilon_0 c} I_{\text{lat}}^{\text{2D}}(x,y,z) \\ &= \frac{V_{\text{lat}}}{1+x^2/x_R^2} e^{-\frac{2(y^2+z^2)}{w_x^2(1+x^2/x_R^2)}} \cos^2 k_L x + \frac{V_{\text{lat}}}{1+y^2/y_R^2} e^{-\frac{2(x^2+z^2)}{w_y^2(1+y^2/y_R^2)}} \cos^2 k_L y \\ &\approx V_{\text{lat}} \left[2 - \frac{4}{w_z^2} z^2 - \left(\frac{2}{w_x^2} + \frac{1}{x_R^2} + k_L^2 \right) x^2 - \left(\frac{2}{w_y^2} + \frac{1}{y_R^2} + k_L^2 \right) y^2 \right] \end{aligned} \tag{3.35}$$

The radial and axial trap frequencies are

$$\omega_j = \sqrt{\frac{2V_{\text{lat}}}{m} \left(\frac{2}{w_j^2} + \frac{1}{j_R^2} + k_L^2 \right)} \approx \sqrt{\frac{2V_{\text{lat}} k_L^2}{m}} = 2\omega_{\text{rec}} \sqrt{s_\perp} = \omega_\perp \tag{3.36}$$

$$\omega_z = \sqrt{\frac{4V_{\text{lat}}}{m} \left(\frac{1}{w_x^2} + \frac{1}{w_y^2} \right)} = 2\frac{\lambda}{\pi \bar{w}} \omega_{\text{rec}} \sqrt{s_\perp} \tag{3.37}$$

where $2/\bar{w}^2 = 1/w_x^2 + 1/w_y^2$. Note that in the experiment, whenever we mention the BEC is loaded into a two-dimensional lattice of $s_\perp = 90$, it means that both the x and y lattices are at $s = 90$, such that $V_{\text{lat}} = V_{\text{lat}}^x = V_{\text{lat}}^y = 90 E_{\text{rec}}$.

3.4.1 Trapped 1D gases

A two-dimensional optical lattice can trap the atoms in an array of 1D tubes. The 1D regime is achieved if all of the relevant energies are lower than the radial trapping frequencies $\omega_\perp$ of the tubes so that the dynamics are only along the axial direction of the tubes. In particular, the condition

$$\mu, k_B T \ll \hbar\omega_\perp \tag{3.38}$$

must be fulfilled, where μ is the chemical potential and T is the temperature of the atoms. For a weakly interacting 1D Bose gas in a harmonic trap, the chemical potential is given by [47]

$$\mu = \hbar\omega_z \left(\frac{3N}{2\sqrt{2}} \frac{a_s a_z}{a_\perp^2} \right)^{2/3} \tag{3.39}$$

where ω_z is the axial trapping frequency, N is the atom number, a_s is the scattering length, $a_z = \sqrt{\hbar/m\omega_z}$ and $a_\perp = \sqrt{\hbar/m\omega_\perp}$ are the oscillator lengths in the axial and radial directions respectively.

The interaction between atoms will also be modified when trapped in a 1D geometry. Strongly interacting one-dimensional bosons will repel each other and become impenetrable, which is also known as a Tonks-Girardeau gas. If the radial extension of the wavefunction is much larger than the characteristic radius of the interatomic potential, the 1D coupling constant is [47, 48]

$$g_{1D} = -\frac{2\hbar^2}{m a_{1D}} \tag{3.40}$$

with

$$a_{1D} = -\frac{a_\perp^2}{a_s} \tag{3.41}$$

where a_{1D} is the 1D scattering length and m is the atomic mass. An important parameter of a 1D gas is the ratio of the kinetic energy to the interaction energy

$$\gamma = \frac{E_{int}}{E_{kin}} = \frac{g_{1D} n_{1D}}{\hbar^2 n_{1D}^2/m} = \frac{m g_{1D}}{\hbar^2 n_{1D}}. \tag{3.42}$$

For a high-density 1D bosonic gas with $\gamma \ll 1$, the atoms are weakly interacting and can be described by the mean-field theory. For low-density bosonic gas with $\gamma \gg 1$, the system becomes a Tonks-Girardeau gas where atoms acquire fermionic properties because of the strong repulsive interaction. It is challenging to experimentally realize the Tonks-Girardeau gas with a large γ. Although the interaction coupling constant, and thus the scattering length, can be tuned using a Feshbach resonance, one must ensure that the 1D conditions are still satisfied because the chemical potential also depends on the scattering length. The requirement of a low-density gas also presents difficulty in measurement due to a lower signal-to-noise ratio. Experimentally, TG gas with $\gamma = 5.7$ has been realized by trapping a very low-density gas in a blue-detuned two-dimensional lattice [49]. By adding a spatial modulation along the tubes with another lattice, TG gases with γ up to 200 has also been achieved [50].

3.5 Pulsed-Optical Lattice: Kapitza-Dirac Diffraction

In this section, we will discuss the theory of Kapitza-Dirac (KD) diffraction, which is an important part of the quantum kicked rotor. Kapitza-Dirac diffraction governs the transfer of amplitudes of the atoms to different momentum lattice sites during every kick of the QKR.

The Kapitza-Dirac effect was first predicted by Paul Dirac and Pytor Kapitsa in 1933 by considering the stimulated Compton scattering of an electron beam [51]. KD diffraction is part of the bigger topic of atom optics, where an ultracold atom cloud is treated as an optical beam and the role of light and matter are reversed. The phase coherence of ultracold quantum degenerate gases allows us to treat it as some coherent optical beam and the atoms are often coherently manipulated with a standing light wave playing the role of matter. This also means that when a BEC interacts with itself or a standing light wave, it will exhibit phenomena such as diffraction and interference. This method of coherently manipulating the momentum states of atoms in atom optics is important in many applications such as atom interferometers, atom kicked rotors, and atom lithography.

When a BEC is diffracted by the diffraction grating formed by a standing light wave, two different scenarios can happen depending on whether the different momentum states are resonantly coupled. In Bragg diffraction, the different momentum states are resonantly coupled by the light and the atoms can oscillate between the different states. If the different momenta are not resonantly coupled, diffraction can still occur if the interaction time is short enough. This is also called the Kapitza-Dirac diffraction. Mathematically, Kapitza-Dirac diffraction is within the limit of the Raman-Nath approximation, in which the atomic motion during the short interaction time is negligible compared to the wavelength of the standing light wave. The constraint on the interaction time t_p can then be expressed as t_p has to be much smaller than the inverse recoil frequency $1/\omega_{\text{rec}}$.

Next, we will follow the treatment in Ref. [52] to derive the effect of the KD diffraction on the atoms. As we have seen in the section on quantum kicked rotor and one-dimensional

optical lattice, the unitary operator of the standing wave interaction is

$$\begin{aligned} U(z,t) &= \frac{V_{\text{lat}}}{2} f^2(t) \cos 2k_L z = \frac{4V_{\text{dip}}}{2} f^2(t) \cos 2k_L z \\ &= \frac{\hbar\Omega^2}{2\Delta} f^2(t) \cos 2k_L z \end{aligned} \tag{3.43}$$

where $\Delta = \omega_L - \omega_0$ is the detuning of the standing light wave frequency ω_L from the atomic resonance ω_0, Ω is the resonant single-photon Rabi frequency of this transition, and $f(t)$ is the temporal envelope of the electric field. Note that we neglected the kinetic energy term since we are considering the Kapitza-Dirac limit or the Raman-Nath approximation. Consider the initial state of an atom to be $|g, 0\rangle$, i.e. it is in the ground energy level and zero momentum state. The atomic wavefunction after the interaction or after a single KD pulse is given by

$$\begin{aligned} |\psi\rangle &= e^{-\frac{i}{\hbar}\int dt' U(z,t')} |g, 0\rangle \\ &= e^{-\frac{i}{2\Delta}\Omega^2 t_p \cos 2k_L z} |g, 0\rangle \end{aligned} \tag{3.44}$$

where $t_p = \int dt' f^2(t')$ and the integral is over the interaction duration. Using the identity of the Bessel functions $e^{i\alpha\cos(\beta)} = \sum_{n=-\infty}^{\infty} i^n J_n(\alpha) e^{in\beta}$, we can then write the wavefunction as

$$\begin{aligned} |\psi\rangle &= \sum_{n=-\infty}^{\infty} i^n J_n\left(\frac{\Omega^2}{2\Delta} t_p\right) e^{i2nk_L z} |g, 0\rangle \\ &= \sum_{n=-\infty}^{\infty} i^n J_n\left(\frac{\Omega^2}{2\Delta} t_p\right) |g, 2n\hbar k_L\rangle. \end{aligned} \tag{3.45}$$

The final state of the atoms is a combination of different multiples of $2\hbar k_L$ momentum states. The interaction of an atom in a standing wave or optical lattice can often be thought of as the atom absorbing a photon from one lattice beam and emitting a photon into the other lattice beam, resulting in a net $2\hbar k_L$ change of momentum.

The probability of the atoms populating the $2n\hbar k_L$ state after the diffraction is then

$$P_n = \left[J_n(\phi_{\text{kick}})\right]^2 \quad \text{with} \quad n = 0, \pm 1, \pm 2, \ldots \tag{3.46}$$

where J_n is the n^{th} order Bessel functions and

$$\phi_{\text{kick}} = \frac{\Omega^2 t_p}{2\Delta} = \frac{V_{\text{lat}} t_p}{2\hbar} \tag{3.47}$$

is the pulse area. Here, we use the label ϕ_{kick} instead of a simpler symbol for several reasons. First, the KD diffraction is applied in the context of the quantum kicked rotor for our work, so it may be more straightforward to think of this as the pulse area for every kick we apply to our atom cloud. Second, since the QKR operator comprises a kick term and an evolution term, the term ϕ_{kick} can be seen as the counterpart of the phase ϕ_{free} accumulated by the atoms during the free evolution time. It is also more convenient to express it in terms of lattice depth V_{lat} instead of Rabi frequency Ω for lattice depth calibration, which will be discussed later.

Chapter 4

EXPERIMENTAL SETUP

The optical lattice is a new addition to our experimental setup for the work presented in this thesis. This chapter discusses the construction of the three-dimensional lattice and its depth calibration. The first two sections review the properties of ytterbium and the fundamental physics of laser cooling and atom trapping. We then present the details of the lattice laser setup, including the design decisions of the optics layout and the alignment of the lattice beam to the atoms. Because of the high-power IR laser involved, we will provide some guides on using the lattice and highlight the precautions needed. We then describe how we use Kapitza-Dirac diffraction to calibrate the lattice depth. Finally, we will show our observation of the superfluid-to-Mott insulator transition in the three-dimensional lattice.

4.1 Properties of Ytterbium

Ytterbium (Yb) is a lanthanide element with atomic number 70 ($[\mathrm{Xe}]4f^{14}6s^2$). It is an alkaline-earth-like element with two valence electrons and has two suitable transitions ($^1S_0 \rightarrow {}^1P_1$ and $^1S_0 \rightarrow {}^3P_1$) for laser cooling. It has several abundant bosonic and fermionic isotopes for studying different types of physics. We use the bosonic isotope ^{174}Yb for all the work presented in this thesis because its large natural abundance (32%) and convenient scattering length (5.55 nm) allow BECs with small initial momentum for the quantum kicked rotor experiment.

^{174}Yb has a nuclear spin of $I = 0$ and a ground state electronic spin of $S = 0$. The ground state is insensitive to the magnetic field, hence making it an appealing choice for precision measurements [53]. Fig. 4.1 shows the energy level structure of ^{174}Yb. The two main transitions we use are the $^1S_0 \rightarrow {}^1P_1$ and $^1S_0 \rightarrow {}^3P_1$ transitions. The singlet transition

($^1S_0 \rightarrow {}^1P_1$) is at 399 nm and has a broad linewidth of 29 MHz. It is utilized for Zeeman slowing and absorption imaging. The triplet inter-combination transition ($^1S_0 \rightarrow {}^3P_1$) is at 556 nm and has a narrow linewidth of 180 kHz that we utilize to load atoms into a magneto-optical trap (MOT) directly. The narrow linewidth allows a lower Doppler temperature for the atoms in the MOT. We modulate the

Figs. 4.2 and 4.3 show our laser setup for the 399 nm and 556 nm lasers. Both lasers are derived from the Toptica-SHG Pro diode lasers and are frequency-stabilized using saturation absorption spectroscopy. Each of the different beams in the setup is sent into an AOM that controls the frequency and amplitude of the lasers. Most of our AOM setups are in a double-pass cat's eye configuration that allows a larger frequency tuning range when the light is sent to the main experiment via optical fibers.

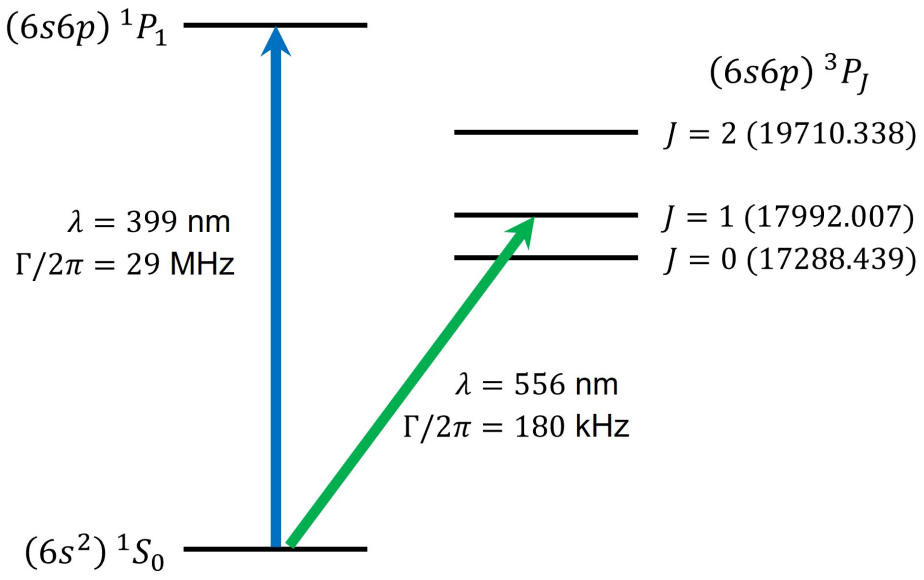

Figure 4.1: Energy level structure of ^{174}Yb. The relevant energy levels of ^{174}Yb used in this work are shown, and the primary transitions are indicated by the solid arrows. Note that the energy level separations are not to scale and the level energies for ^3P_J levels in the parentheses have units of cm^{-1}. The $^1S_0 \rightarrow {}^1P_1$ transition is used for Zeeman slowing and absorption imaging while the $^1S_0 \rightarrow {}^3P_1$ transition is used for magneto-optical trapping. The transition wavelength and linewidth are labeled next to the arrow.

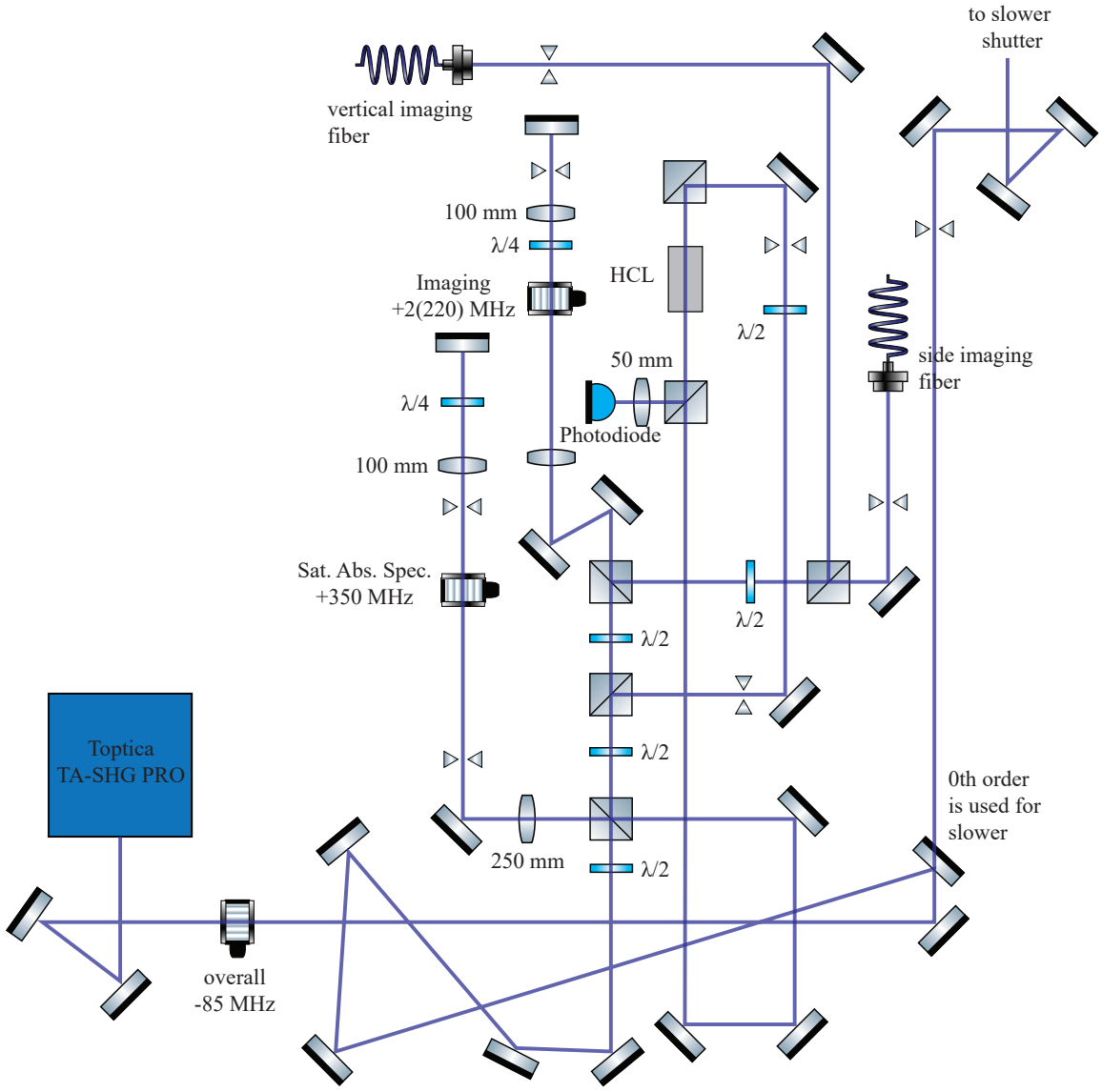

Figure 4.2: A schematic of the 399 nm laser setup. The output of the Toptica laser is about 220 mW and is divided into four beams − pump and probe beams for the saturation absorption spectroscopy, slowing beam, and imaging beam. The slowing beam is from the zeroth-order diffracted beam of the overall AOM, so its frequency can only be changed through the settings of the spectroscopy setup. A hollow cathode lamp (HCL) is used for saturation absorption spectroscopy. The imaging beam can be coupled into either the side or vertical imaging fiber for different experiments.

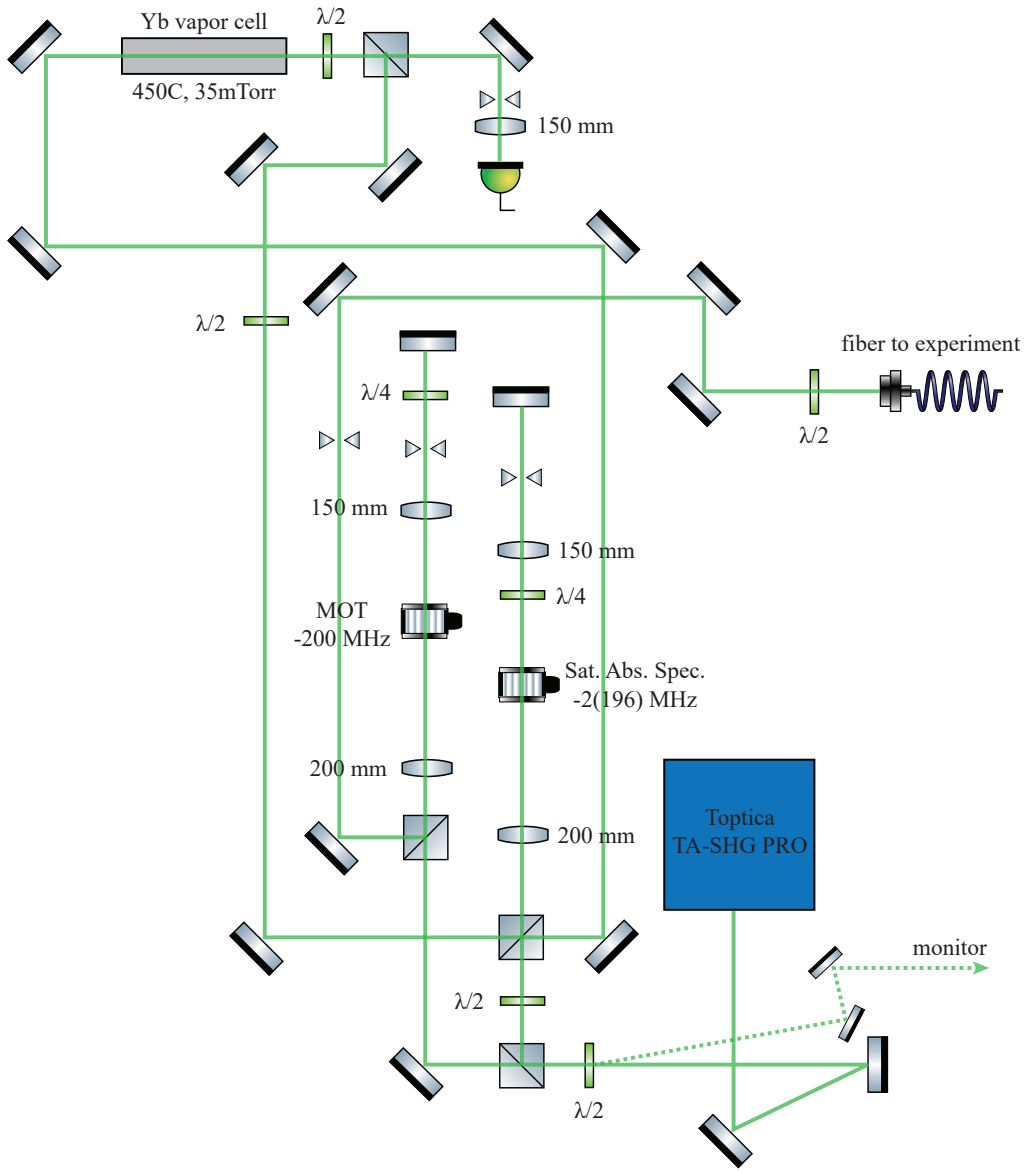

Figure 4.3: A schematic of the 556 nm laser setup. The output of the Toptica laser is about 500 mW and is divided into three beams − pump and probe beams for the saturation absorption spectroscopy and the MOT beam. The pump beam and the MOT beam are sent into an AOM respectively to shift the frequency of each beam. The MOT beam is sent to the main experiment through a fiber. The light reflected off the first waveplate is used for monitoring the wavelength.

4.2 Laser Cooling and Trapping of Yb

In this section, we will summarize the basic principles of laser cooling and atom trapping. We will also outline how these techniques are implemented in our experimental apparatus. The reader is referred to Foot's Atomic Physics [43] for more details on the physics of laser cooling and trapping, and to the thesis by Anders Hansen [54] for details on our experimental setup.

4.2.1 Atom source and Zeeman slower

Our vacuum chamber consists of several sections: the Yb and Li ovens, Zeeman slowers, and the main chamber, as shown in Fig. 4.4. The metals are heated up to about 450 degrees Celsius in the oven creating an effusive atomic beam that travels down the Zeeman slower to the main vacuum chamber maintained at a pressure of $\sim 10^{-11}$ Torr. As the hot vapor travels down the Zeeman slower, the atoms are slowed down by the radiation force from the slower beam propagating in the opposite direction. The resonance condition for the slowing process is maintained by the magnetic field produced by the solenoid of the Zeeman slower to compensate for the changing Doppler shift as the atoms are slowed down, which can be written as

$$\omega_0 + \frac{\Delta\mu\, B(z)}{\hbar} = \omega + kv\,. \tag{4.1}$$

Here, ω_0 is the bare atomic resonance, ω is the slower laser frequency, v is the velocity of the atoms, and $\Delta\mu$ is the change in the magnetic moment due to the laser excitation. For our setup, the magnetic field $B(z)$ of the Zeeman slower is increasing towards the main chamber and the slower light targets the σ^- transition, giving $\Delta\mu = -\mu_B$. The frequency of the slower light is optimized to minimize the effective detuning δ_{eff} along the Zeeman slower

$$\delta_{\text{eff}} = \delta_{\text{laser}} + kv - \frac{\Delta\mu\, B(z)}{\hbar}\,. \tag{4.2}$$

Typically, the laser frequency and field are also chosen such that the atom velocity is nonzero at the end of the slower so that the atoms can still travel to the center of a vacuum chamber

for further cooling and trapping by a magneto-optical trap (MOT). Our experimental setup also has a slower compensation coil on the opposite side of the Zeeman slower to cancel the fringe field from the slower coils at the center of the MOT.

4.2.2 Magneto-Optical Trap (MOT)

Once the Zeeman slowed atoms arrive in the main chamber, they are trapped by the magneto-optical trap (MOT). A MOT consists of three pairs of counter-propagating beams of circularly-polarized light and a magnetic field gradient produced by a pair of anti-Helmholtz coils. The velocity of the atoms at the end of the Zeeman slower coil should be optimized such that the atoms are able to travel to the center of the MOT but still be slow enough to be captured by the MOT.

For a given MOT beam with diameter D, if we assume that the atoms scatter photons at the maximum rate $\Gamma/2$ across the entire beam diameter, the capture velocity is then estimated to be

$$v_{\text{cap}} \simeq \sqrt{\frac{2F_{\max}D}{m}} \tag{4.3}$$

where $F_{\max} = \hbar k\Gamma/2$ is the maximum radiation force experienced by the atoms, m is the atomic mass, and $k = 2\pi/\lambda$ is the wavenumber of the MOT light. For our MOT with $\lambda = 556$nm, we estimate $v_{\text{cap}} \simeq 3$ m/s for a beam diameter of $D \sim 10$ mm. To compensate for this small capture velocity, we add a frequency sweep of the MOT beams of 10MHz peak-to-peak.

The opposite scattering forces keep the atoms always at the center of the MOT. The force on the atoms along a direction say z-axis, is given by [43]

$$F_{\text{MOT}} = F^{\sigma^+}_{\text{scatt}}(\omega - kv - (\omega_0 + \beta z)) - F^{\sigma^-}_{\text{scatt}}(\omega + kv - (\omega_0 - \beta z)) \tag{4.4}$$

$$\simeq -2\frac{\delta F}{\delta\omega}kv + 2\frac{\delta F}{\delta\omega}\beta z \tag{4.5}$$

$$= -2\frac{\delta F}{\delta\omega}(kv + \beta z) \tag{4.6}$$

$$= -\alpha v - \frac{\alpha\beta}{k}z \tag{4.7}$$

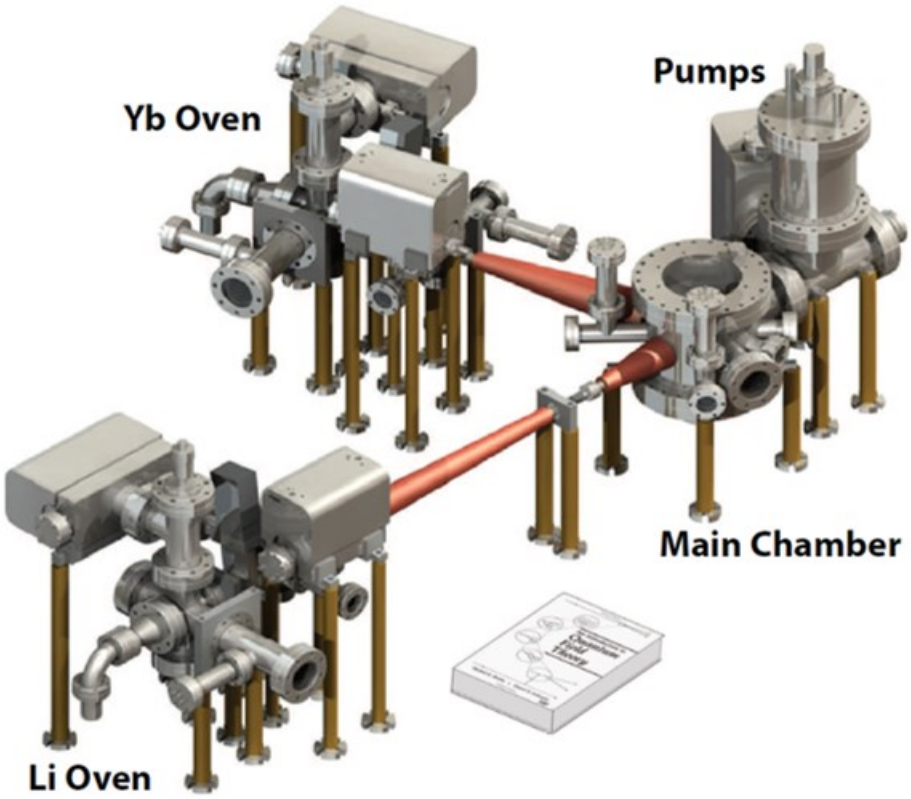

Figure 4.4: A schematic of the vacuum chambers. Our machine is constructed to trap both Yb and Li. Atoms are heated and vaporized in each oven, and then slowed down in a Zeeman slower together with a counter-propagating slower beam. Once the atoms are in the main chamber, they are trapped in a magneto-optical trap (MOT) before they are cooled further for our experiments. A physics textbook is shown for scale.

where

$$\beta z = \frac{g\mu_B}{\hbar}\frac{dB}{dz}z \tag{4.8}$$

is the Zeeman shift at position z due to the nonzero magnetic field. Eq. 4.7 shows that atoms in a MOT behave as a damped harmonic oscillator with damping coefficient α and spring constant $\alpha\beta/k$. Whenever an atom is displaced from the center of the trap, the imbalanced scattering forces push the atom back.

Once the atoms are in the MOT (Fig. 4.5), we further cool and compress the MOT into a compressed MOT (CMOT) by simultaneously ramping up the magnetic field gradient and ramping down the detuning and the intensity of the MOT light. This is to increase the phase space density of the atom cloud and to allow more atoms to be loaded into the optical dipole trap. For our experiment, we typically have about 1×10^8 atoms in a CMOT with a temperature of 30 μK using less than 4 seconds of load time, as shown in Fig. 4.6.

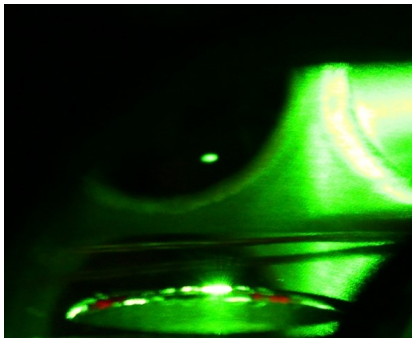

Figure 4.5: A photo of Yb MOT. A green blob of Yb MOT is floating in the vacuum chamber. The green fluorescence is from the ${}^1S_0 \rightarrow {}^3P_1$ MOT transition.

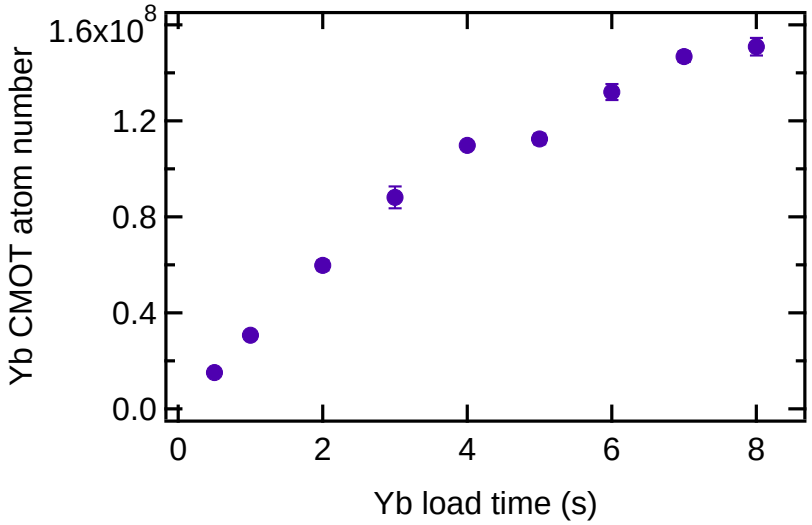

Figure 4.6: Yb CMOT atom number vs load time measured on Jan 26, 2020.

4.2.3 Optical Dipole Trap (ODT)

To cool the Yb atoms down to degeneracy, we need to load the atoms into an optical dipole trap (ODT) for evaporative cooling. As already explained in the previous chapter, an optical dipole trap is set up by illuminating the atoms with a tightly focused laser. The electric field of the light induces a dipole moment on the atoms, and these dipole moments are then attracted to the focus of the red-detuned laser beam, where the electric field is the strongest. The potential depth of the ODT is given by

$$V_{\text{dipole}} = -\alpha I = -\frac{\hbar\Gamma^2}{8I_{\text{sat}}}\left(\frac{1}{\omega_0 - \omega_L} + \frac{1}{\omega_0 + \omega_L}\right) I \tag{4.9}$$

where α is the polarizability of atoms, ω_L is the ODT laser frequency, ω_0 is the resonant frequency, Γ is the linewidth of the transition, I_{sat} is the saturation intensity, and I is the intensity of the laser. Our ODT laser has a wavelength of 1064 nm and a maximum power of about 50W. It is set up in a crossed-beam configuration: after the light is tightly-focused into the chamber, it is recycled and refocused into the chamber again through another viewport, with the two beams intersecting at an angle of about 64°. We also modulate the center position of the ODT beam, which we colloquially refer to as "painting", to increase the trap volume and thus the evaporation rate at low depths. The readers can refer to Richard Roy's works [44, 45] for more details on the setup.

We typically trap about 1.2×10^7 Yb atoms in the ODT at about 20 μK with the maximum laser power (45 W). We then cool the atoms evaporatively by lowering the laser power and painting to spill the hottest atoms and let the remaining atoms rethermalize. This process is repeated continuously and smoothly until quantum degeneracy is reached. We stabilize the intensity of our ODT laser through an AOM and two feedback photodiodes − one for coarse feedback used at high laser power, and one for fine feedback to allow more precise control at low laser power where the delicate BEC is obtained. During evaporative cooling, we ramp down the laser power exponentially in two stages (due to the different gain settings on the two photodiodes), and the entire process takes about 10 seconds. We typically have about 2.3×10^5 atoms in a Yb BEC with a lifetime of more than 5 seconds. Fig. 4.7 shows

the time-of-flight (ToF) absorption images of the Yb atom cloud at different ODT depths. At high trap depth, the momentum of the thermal cloud has a Gaussian distribution after the ToF, and as quantum degeneracy is approached, a bimodal distribution can be seen. When the atoms are fully degenerate, the momentum of the BEC has a pure Thomas-Fermi distribution [43].

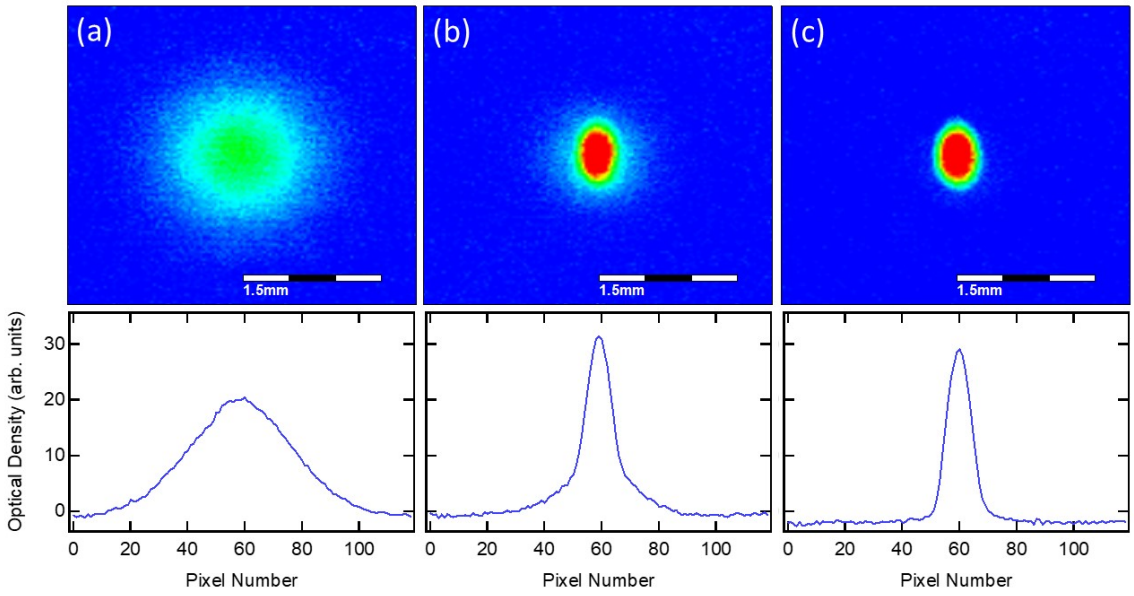

Figure 4.7: Time-of-flight (ToF) absorption images of the Yb atom cloud at different ODT depths and the corresponding momentum distribution. During the evaporation process, the hot atoms are spilled out and the rest of the atoms rethermalize to a lower temperature. (a) The momentum of the thermal cloud shows a Gaussian distribution. (b) The momentum has a bimodal distribution near quantum degeneracy. (c) The fully degenerate BEC shows a pure Thomas-Fermi distribution.

For the experiments presented in this thesis, once we obtain the BEC, we load it into a two-dimensional lattice to control the interactions between the atoms. We then carry out the kicked rotor experiments by exposing the atoms to a periodically-pulsed optical lattice along the weak (third) axis.

4.2.4 Absorption Imaging

Once the atoms are manipulated in the ODT or the optical lattice, we snap off all the trapping potentials and let the atom cloud expand in the vacuum. After some time-of-flight (ToF), we probe the atoms by passing resonant light through the atoms onto a CCD camera. The atoms absorb part of the light and cast a shadow onto the camera. By analyzing the spatial and momentum distribution of the atoms after the ToF, we can measure quantities like atom number and temperature of the atom cloud. We have a side imaging and a vertical imaging setup to probe the atoms from different directions. We use side imaging for daily optimization of the atom number and vertical imaging for most of the quantum kicked rotor experiments.

4.3 Design and Construction of the Three-Dimensional Optical Lattice

In recent years, ultracold atoms in optical lattices have proven to be an effective tool for quantum simulation of many-body systems [11, 55, 56], quantum computation [57], and precision measurement [58]. We built a three-dimensional optical lattice for the work presented in this thesis − one dimension for the kicks, and the other two forming 1D tubes to control the interactions of the atoms. In this section, we will describe the full details of the optical lattice setup including how the design decisions were made and implemented.

Our lattice laser is derived from a homebuilt external cavity diode laser (ECDL). Fig. 4.8 shows a schematic of the ECDL setup and Fig. 4.9 shows a photo of the actual implementation. The homebuilt ECDL is controlled by Thorlabs current and temperature controllers. With settings of 11 kΩ on the thermistor and 365 mA on the current, the diode typically outputs about 100 mW of light with a wavelength of 1073 nm. Figure 4.10 shows the characterization of the laser power for different diode currents. We optimize the optical feedback of the laser diode and measure the lasing threshold current of the diode to be around 20 mA. The light from the ECDL is shaped and collimated using some cylindrical lenses and then sent through an EOT optical isolator to prevent back-reflected light from damaging the laser diode. A small portion of the light is sent to a wavemeter for monitoring the wavelength of the light, and the rest of the light (about 80 mW) is directed to a commercial fiber amplifier (Nufern NUA-1064-PD-0050-D0) through a polarization-maintaining optical fiber, as shown in Fig. 4.11. The Nufern amplifier is capable of amplifying the seed light up to 50 W, and is water-cooled to prevent it from heating up at a high power setting. The power setting can be controlled using the Nufern software, as shown in Fig. 4.12. As with any laser amplifier, it is a good practice to ensure that the amplifier is injected with a seed beam when it is turned on, to prevent the amplifier from dumping all the power on itself and breaking down.

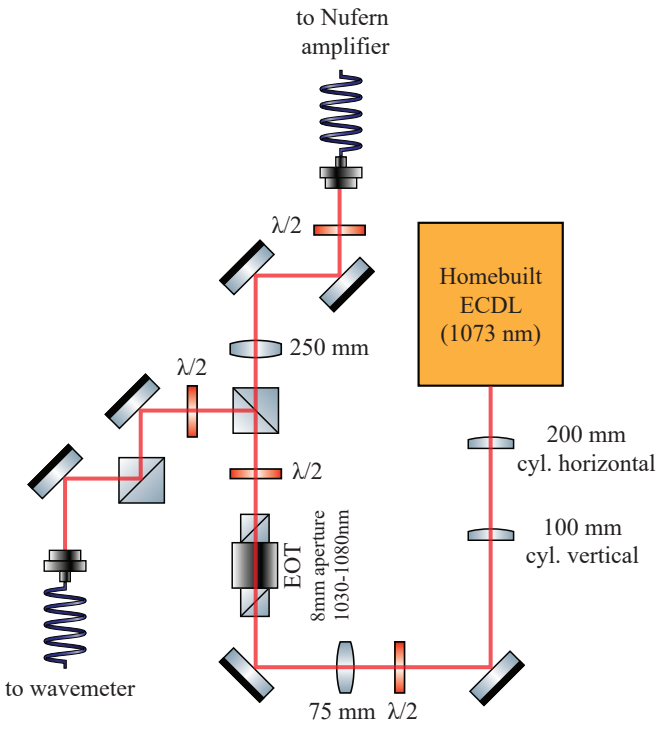

Figure 4.8: A schematic of the source of the lattice laser. The source light is from a homebuilt ECDL with a wavelength of about 1073 nm, and the beam is collimated using some lenses. A part of the beam is sent to the wavemeter for monitoring and the rest is sent to the Nufern amplifier.

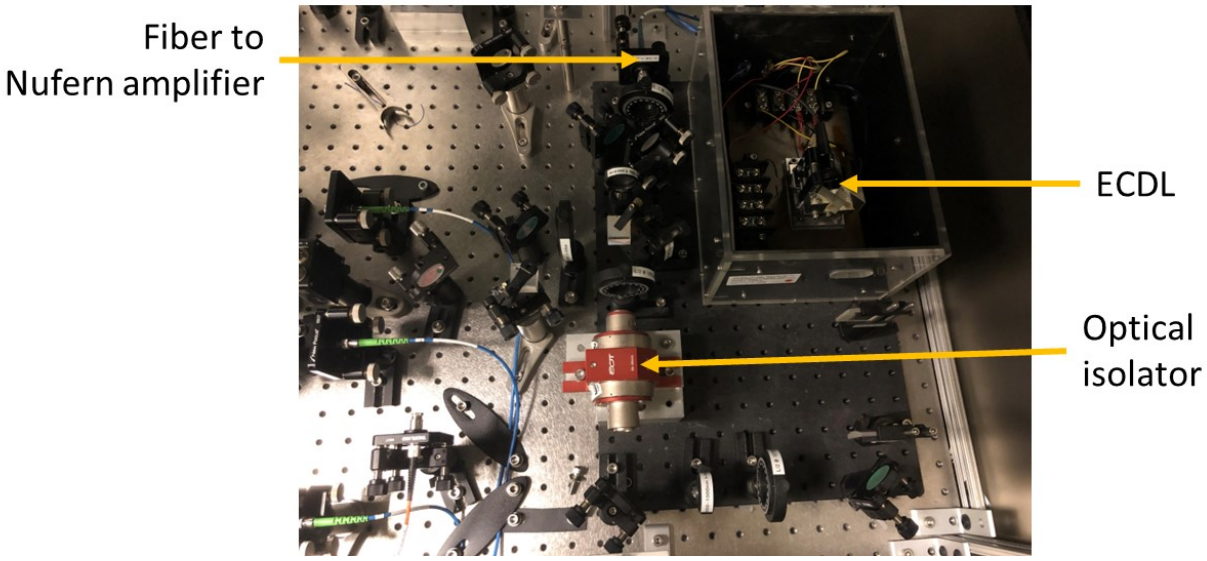

Figure 4.9: A photo of the master laser for the optical lattice. The light is derived from a homebuilt ECDL and sent to the Nufern amplifier through a fiber.

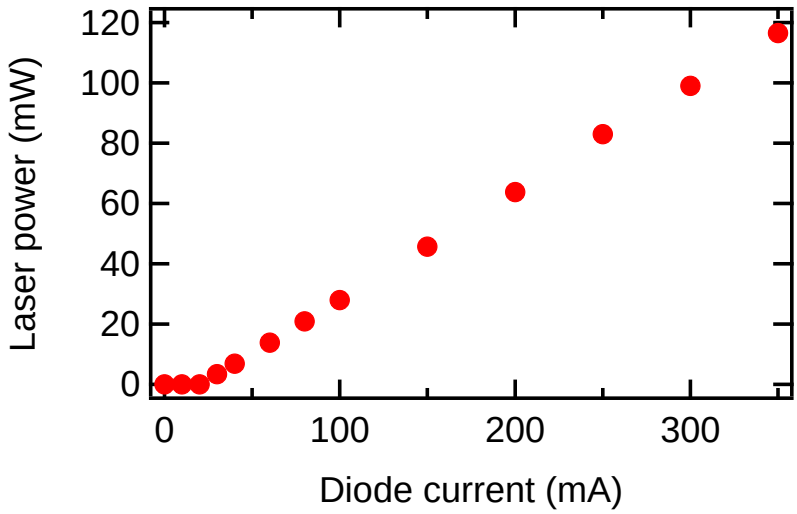

Figure 4.10: Laser power versus diode current measurement of the lattice master laser. The lasing threshold is about 20 mA.

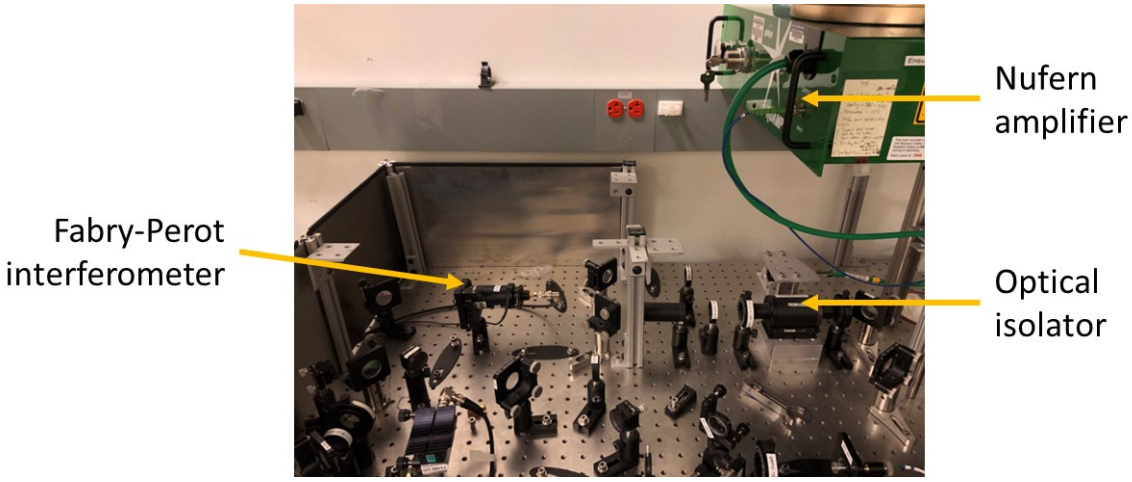

Figure 4.11: A photo of the Nufern amplifier and the optics at its output.

Figure 4.12: Graphical user interface (GUI) of the Nufern amplifier control software.

Below are the steps to turn on the Nufern amplifier:

1. Turn on seed laser.
2. Open the water valve and make sure the water is going through the amplifier cooling circuit.
3. Pull the red button.
4. Open up the Nufern control software on the computer. The GUI should display "NOT READY". Make sure the power control setting is at 0%.
5. Turn the key to the "fire" position. The GUI should now display "READY".
6. Measure the power at the output of the amplifier and optimize the fiber coupling of the seed light into the amplifier. It should read at least 1 mW, below which the amplifier will not work. Make sure you remove the power meter once this step is done.
7. The GUI also displays the power of the seed light detected, which should have a similar value (at least 1 mW). Also, check the temperature reading displayed in the GUI and make sure the amplifier is not heating up.
8. Click the "ENABLE" button. You can now turn up the power control setting in the GUI. You should start from a low power setting (about 10%) and make sure nothing is burning in the beam path before going to a higher power setting.

To turn off the amplifier, simply follow the steps above in reverse.

Figure 4.13 and 4.14 show a schematic and a photo of the optics layout after the Nufern amplifier. The output of the Nufern amplifier is collimated and shaped using a telescope, and as a safety measure, we placed a lens tube around the focus of the light in between the telescope. The light is then sent through a high-power isolator (Thorlabs IO-5-1069-HP), followed by some mirrors and lenses. Figure 4.15 shows the power measured at different locations after the amplifier as the power control setting of the amplifier is turned up. The laser output of the amplifier can go up to about 55 W and the efficiency of the isolator is more than 80%. The steep drop in the efficiency above 80% power control setting is likely due to the bad spatial mode of the output light at the high power. Note that the quoted maximum output of the amplifier is 50 W. We typically used a 70% power control setting

for the work presented in this thesis.

After the isolator, some leaked light through one of the IR mirrors is coupled into a Fabry-Perot interferometer (Thorlabs SA200-8B) for monitoring the frequency mode of the laser. The light is then divided using TFPNs (CVI TFPN-1064-PW-1025-UV) into three beams, one for each axis of the three-dimensional optical lattice. Along each lattice arm, the light is sent through an AOM, followed by a TFPN to clean up the polarization, before it is coupled into a polarization-maintaining fiber (Thorlabs PM980-XP) that directs the light to the vacuum chamber.

The frequency of each of the AOMs is separated by 40 MHz to prevent interference between the three lattices. The AOMs for lattice 2 and lattice 3 are driven and controlled by our usual rf driver and circuit. Lattice 2 and 3 are also intensity stabilized to below 2% peak-to-peak noise level, with the error signal fed to the corresponding AOMs. The rf control circuit for the lattice-1 AOM is slightly different. Its rf source is from a typical MiniCircuit voltage-controlled oscillator but the amplitude and switch are controlled by an IQ modulator (ADL5390-EVALZ), which allows a fast switching time and a quick power response that we need for the kick pulses. While setting up the lattice laser, we noticed that the thermal lensing effect caused by the high-power laser can affect the alignment of the optics quite significantly. Particularly, to prevent the fiber from being damaged, we optimized the position of the aspheric lens for fiber coupling at an intermediate power so that the actual fiber coupling efficiency at high power is not too low.

After the lattice light source is set up and prepared, we set up the three-dimensional optical lattices around the vacuum chamber. A typical optical lattice setup usually consists of a pair of lenses that focus the light into the chamber and collimate it after the chamber and retro-reflecting mirror. The design and construction of the optical lattice is a challenging problem for us due to the crowded space around the vacuum chamber. We also had to consider how each lattice arm is combined with the existing beams, particularly the MOT and ODT beams. With the laser power available, we aimed for a beam waist of 100 μm for each lattice beam. Once we had a rough layout of the optical paths, we estimated the path

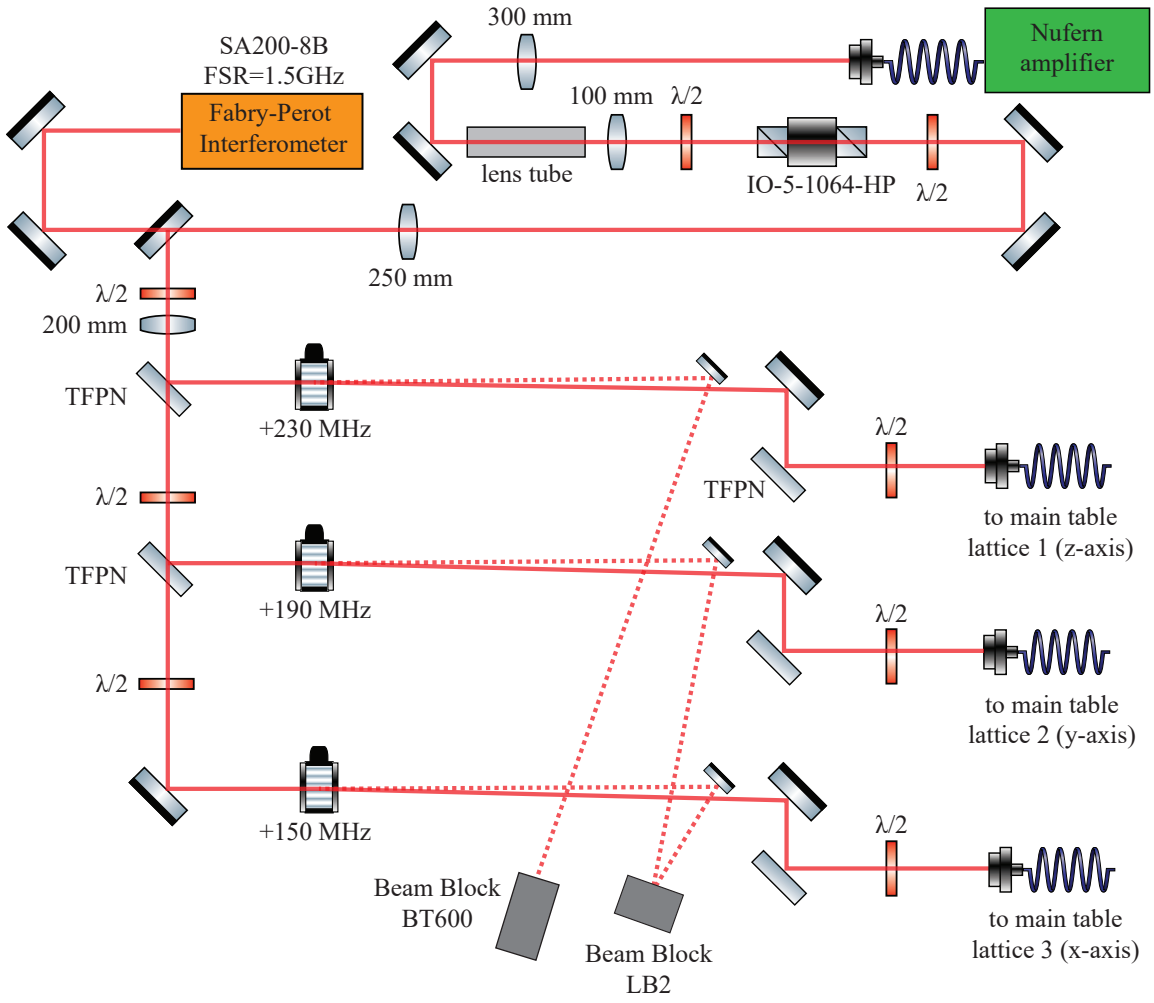

Figure 4.13: Optics layout of each lattice beam on the lattice table. The output of the Nufern amplifier is collimated and sent through an optical isolator. The beam is then divided into three paths, one for each lattice, using TFPNs and waveplates. Each lattice beams is sent through an AOM and then fibered over to the main experiment table. The leaked light through one of the IR mirrors is sent to a Fabry-Perot interferometer to monitor the frequency mode of the light.

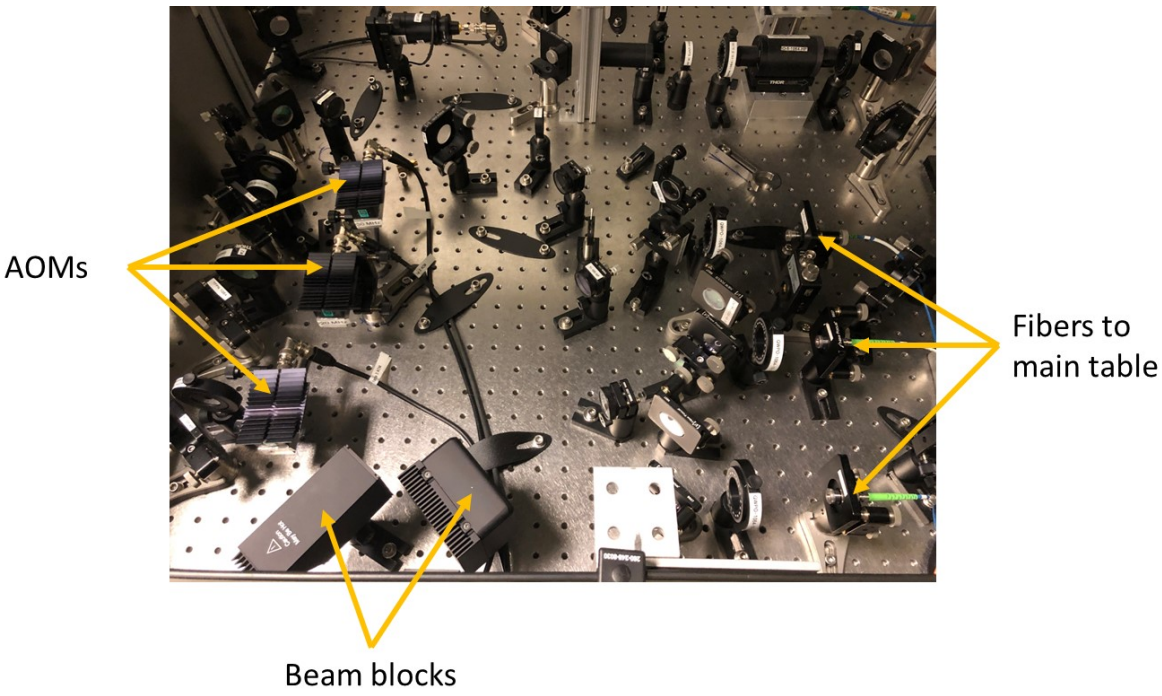

Figure 4.14: A photo of the lattice optics setup after the amplifier. The light is divided using TFPNs into three beams, one for each lattice arm.

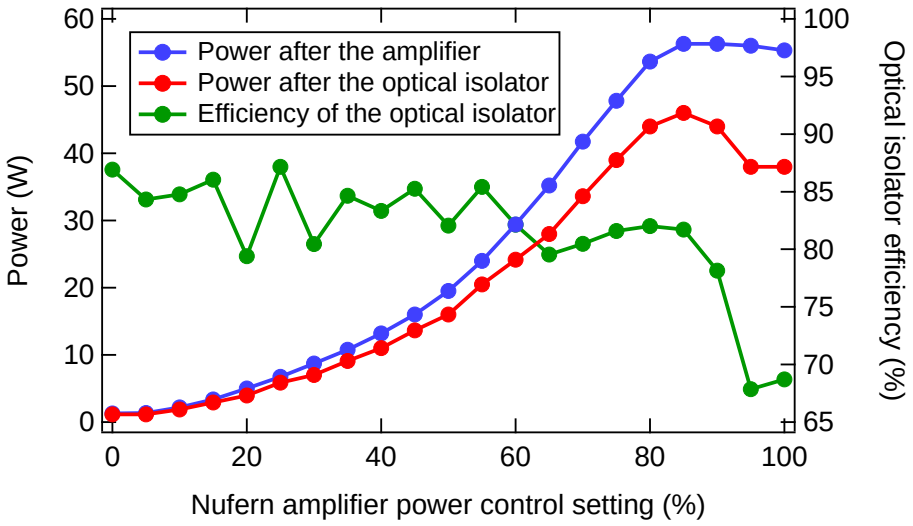

Figure 4.15: Power measurement of the Nufern amplifier output and the efficiency of the optical isolator. The laser power is measured at locations right after the amplifier (before the isolator) and after the isolator. The efficiency is calculated from the ratio of these two powers. These measurements are recorded on March 9, 2020.

length and decided on the lenses needed to achieve the desired beam waist.

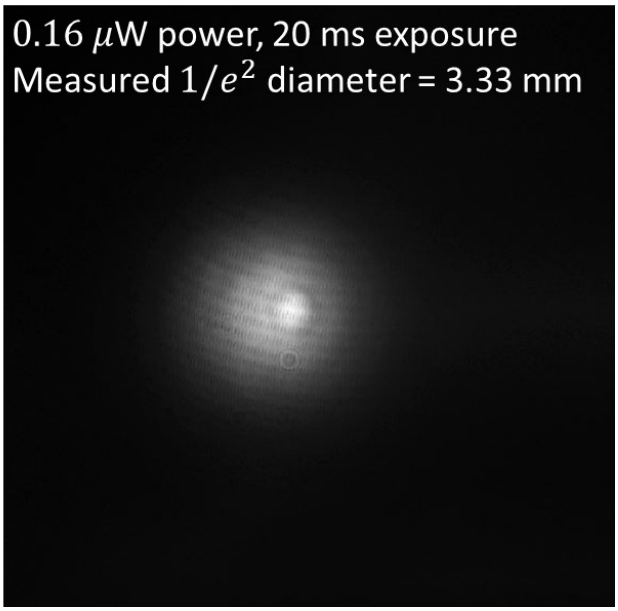

Figure 4.16: Image of the lattice-3 beam at the fiber output. The collimating aspheric lens F260APC-1064 has a quoted beam diameter of 3.37 mm and we measured 3.33 mm.

We chose the collimating aspheric lens at the fiber output carefully to get the right initial beam size. We imaged the beam at the fiber output to verify the beam size and also to check the spatial mode of the beam. Figure 4.16 shows the image of the lattice-3 beam at its fiber output, and the measured $1/e^2$ diameter is 3.33 mm, close to the quoted value of 3.37 mm. The collimator aspheric lenses we use for lattice 1, 2, and 3 are TC12APC-1064 (quoted beam diameter of 2.70 mm), F220APC-1064 (2.4 mm), and F260APC-1064 (3.37 mm), respectively.

After the light out of the fiber is collimated, it is directed along the designed path through several optical components to form an optical lattice. Figure 4.17 shows the schematic of the optics setup of lattice 1 and 2 placed on the breadboards around the vacuum chamber. The output of lattice 1 (z-axis) is sent through a half waveplate and a TFPN to clean up its polarization. The light reflected off the half waveplate is directed to a fast photodiode

(Thorlabs PDA20CS2) for monitoring the kick pulses. The beam is then focused by a lens with a 300 mm focal length into the chamber after it is combined with the MOT beam using a short-wave-pass dichroic mirror. The tiny portion of lattice light that leaks through the dichroic mirror can be used as another monitoring beam but we found that its power is too low for practical purposes. After the chamber, the MOT and lattice beams are separated by another dichroic mirror, and the lattice beam goes through another lens and is then retro-reflected by a mirror.

The lattice-2 (y-axis) beam also goes through a half waveplate and a TFPN for polarization cleaning. A tiny portion of the output is reflected by a pellicle into a photodiode (Thorlabs PDA30B2) for intensity feedback. A pellicle, instead of a waveplate, is used because its reflection is insensitive to the polarization fluctuation that can cause intensity fluctuation. The TFPN also serves the purpose of overlapping the lattice-2 beam with the ODT beam. The two beams are then sent through a focusing lens and combined with the MOT beam using a dichroic mirror. The optics setup after the vacuum chamber is similar to that of the lattice-1 except the additional TFPN used to separate the ODT and the lattice beams. Figure 4.18 shows the actual optics layout of lattice 1 and lattice 2 around the vacuum chamber.

Figure 4.19 shows the schematic of the optics setup of lattice-3 (x-axis), which has a vertical configuration. Similarly, the lattice beam goes through the polarization cleaning optics and a focusing lens. The lattice beam is then combined with the MOT and imaging beams using a dichroic mirror and reflected upwards into the vacuum chamber. It is then sent through a lens, a dichroic mirror, and retro-reflected by a mirror. The dichroic mirror separates the lattice and the imaging beams, and a flipper mirror is used to direct the MOT light to its path during the atom loading. The leaked light through the dichroic mirror is sent to a feedback photodiode (Thorlabs PDA30B2).

Aligning the lattice beam can be challenging due to the small beam waist ($\sim 100\,\mu$m) and atom cloud ($\sim 20\,\mu$m). To find the position of the atom cloud, we typically overlap a temporary imaging beam along the lattice beam path and take an image of the atom cloud.

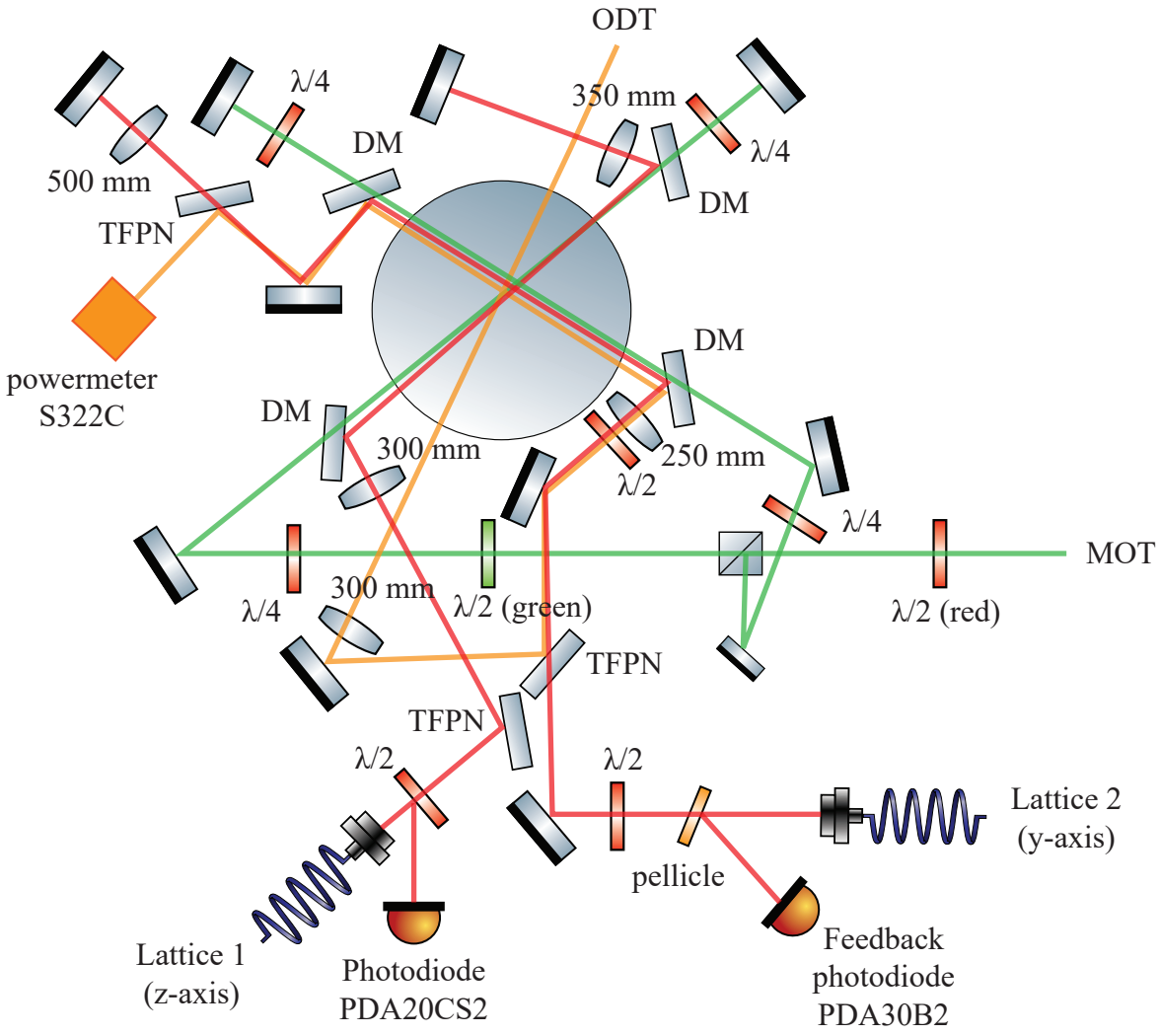

Figure 4.17: A simplified schematic of the optics near the vacuum chamber (Top view) showing how the lattice beams are integrated into our setup. Each of the lattice 1 and lattice 2 beams is sent through a TFPN to clean up its polarization before being combined with the MOT beam along that direction through a dichroic mirror (DM). Part of the light at the fiber output is sent into a photodiode for monitoring or intensity stabilization. Each lattice beam is focused into the chamber using a focusing lens and then retroflected. The lattice 2 beam is also overlapped with the ODT beam. The two lattice beams intersect at a right angle.

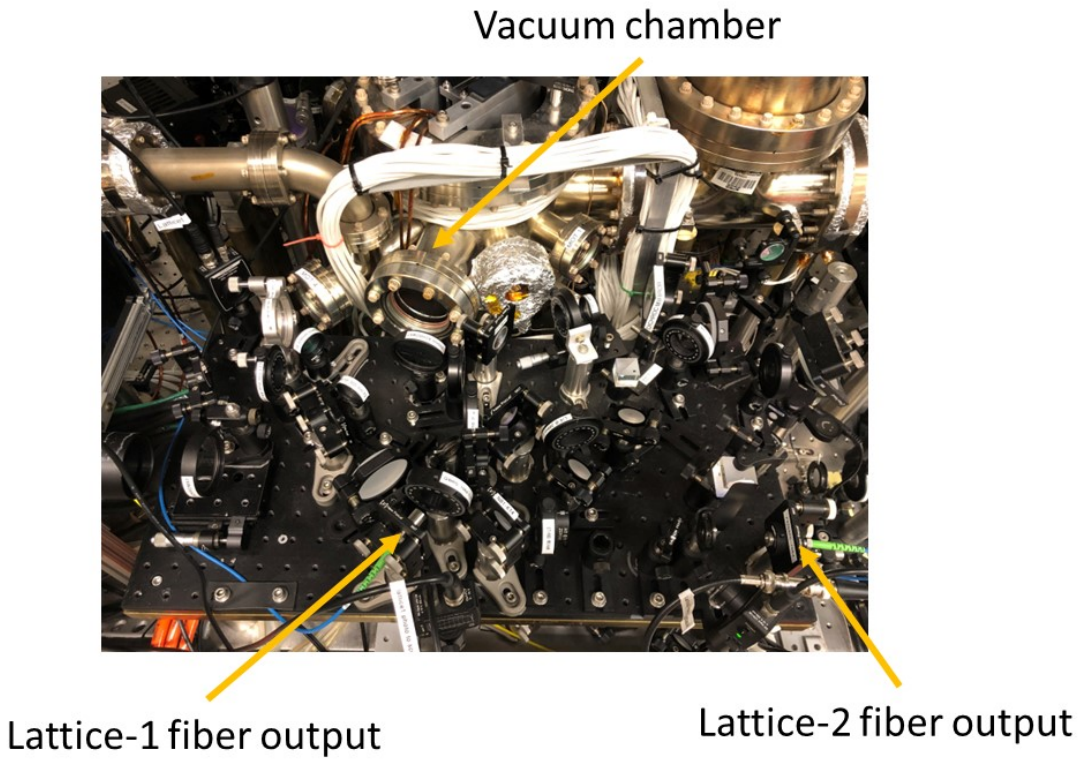

Figure 4.18: A photo of the optics layout of lattice 1 and lattice 2.

During this process, the lattice lens after the vacuum chamber is used as a collecting lens and the retro-reflecting mirror is replaced by a focusing lens and a Mako camera. Once an image is taken, the lattice beam is then aligned to the atom position on the camera. Since lattice-2 also shares the same light path with the ODT beam, the alignment can also be done by overlapping them together on the camera without having to image the atom cloud. Figure 4.20 shows an image of the ODT beam and the lattice-2 beam on the Mako camera. The ODT beam should remain untouched and the lattice-2 beam can be easily walked to overlap with the ODT beam.

The fine alignment of the lattice forward beam has to be done by observing the response of the atom number using the usual imaging setup while walking the pointing of the lattice

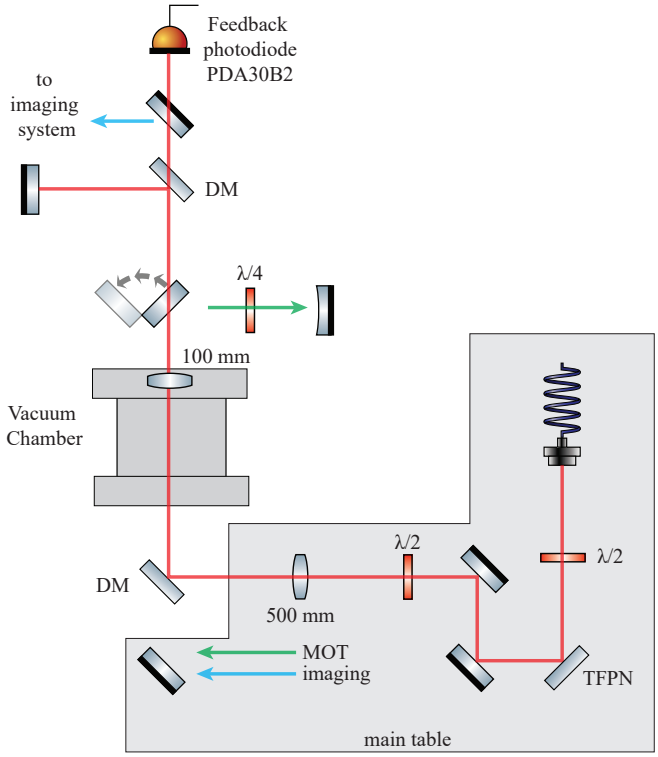

Figure 4.19: A simplified schematic of the lattice 3 (x-axis) setup. The output of the fiber is sent through a TFPN to clean up the polarization. After being sent through a focusing lens, the beam is then reflected upwards from the main table into the vacuum chamber through a dichroic mirror (DM) which also combines the beam with the vertical MOT beam. The lattice beam is then retro-reflected using a mirror after the vacuum chamber. A tiny portion of the light leaked through the mirrors after the chamber and is sent to a photodiode for intensity stabilization.

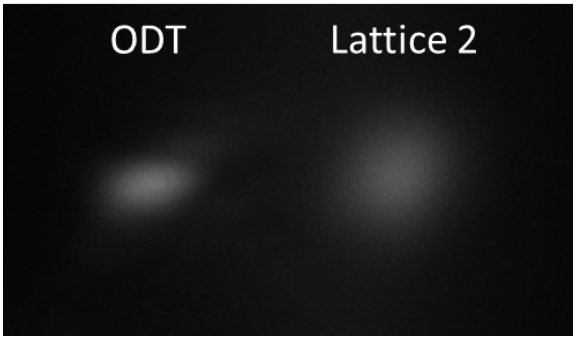

Figure 4.20: An image of the ODT beam and the lattice-2 beam at the same focused position. The ODT beam looks elliptical because its center position is modulated ("painting"). This image was taken using the Mako camera on March 28, 2020.

beam. To obtain a large signal of the effect from the lattice beam, we turn on the lattice light to high power (about 3 W) during evaporation and observe the response of the BEC. Figure 4.21 shows how the lattice-2 forward beam increases the atom number and the atom temperature at the end of the evaporation. Without the lattice-2 light, we obtain the usual pure BEC. When we turn on the lattice-2 light during evaporation, we trap twice as many atoms at the end of the evaporation because of the additional optical potential from the lattice beam, and the atoms are also hotter. These effects are also used to optimize the position of the focusing lens.

Once the focus position and the pointing of the forward lattice beam are optimized, the retro-reflecting mirror is installed to complete the lattice. The retro-reflected light is coupled back into the lattice fiber itself, and the coupling is optimized by walking the retro-reflecting mirror, the dichroic mirror, and the position of the lens after the chamber. This ensures that the retro-reflected light is refocused onto the atoms. With the optical lattice completely set up, we can expect to observe Kapitza-Dirac diffraction if we apply a short pulse of lattice light to the atoms. Figure 4.22 shows some time-of-flight absorption images of the atoms diffracted from the lattice grating. We can see that the BEC is diffracted into many orders of momentum with different populations. This diffraction can also happen in two dimensions

if we pulse on two optical lattices simultaneously.

When the lattice setup was completed, we encountered an interesting problem with the lattice power supported by the optical fibers. We noticed that when the lattice light is retro-reflected and recoupled into the fiber, the maximum power of the fiber output drops from about 4 W to 1.5 W. We attribute this to the stimulated Brillouin scattering effect of the optical fiber. The two counter-propagating light waves generate a traveling refractive index grating within the fiber and effectively increase the reflection of the light waves and reduce the power transmitted [59]. All of our lattice fibers have APC-APC connectors to reduce the reflection caused by the inner surface of the fiber head, but this does not solve the problem of lower fiber output because there are still two counter-propagating waves within the fiber. However, we are not limited by the problem for the QKR experiment because we do not need more than 1.5 W of lattice light in each dimension. In the future, this problem can be fixed by adding an optical isolator at the output of the fiber to prevent the retro-reflected light from going back into the fiber. Another approach is to slightly misalign the retro-reflected light meanwhile ensuring that the light is still hitting the atoms and that the misaligned beam does not damage the fiber head.

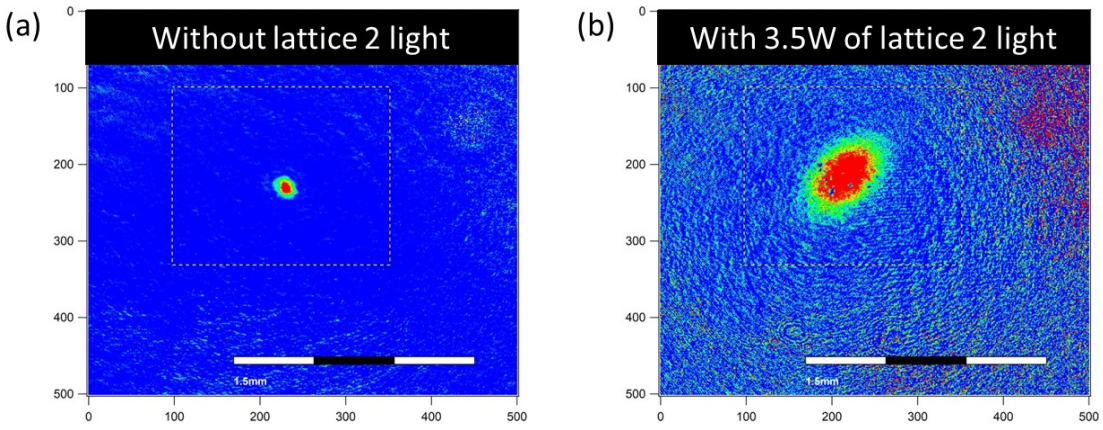

Figure 4.21: Absorption images of the atoms showing the effect of the lattice-2 forward beam. The images above are taken on March 28, 2020, using the Andor camera in the vertical imaging configuration. (a) Without the lattice-2 light, the image shows the typical BEC at the end of the evaporation. (b) When 3.5 W of lattice-2 light is kept on during the evaporation process, twice as many atoms are trapped because of the additional optical potential. We used this response to optimize the fine alignment of the forward lattice beam to the atom cloud.

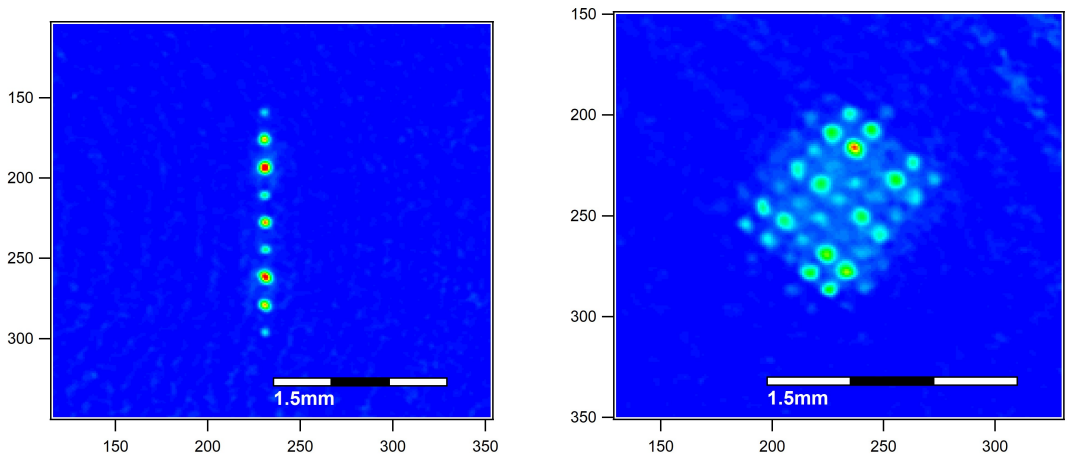

Figure 4.22: Time-of-flight absorption images of the diffracted atoms. The BEC can be diffracted in one dimension (left) and two dimensions (right) after a short pulse of lattice light is applied.

4.4 Lattice Depth Calibration

Once the optical lattices are set up and aligned to the atoms, we have to calibrate their depths so that we know the relationship between the laser power and the lattice depth. We calibrate our lattice depths using Kapitza-Dirac diffraction by applying a single pulse of the lattice light to the BEC and measuring the population of the atoms in each momentum order. As discussed in the previous chapter, the fractional population of the atoms in n^{th} order is given by Eq. 3.46,

$$P_n = [J_n(\phi_{\text{kick}})]^2 \quad \text{with} \quad n = 0, \pm 1, \pm 2, \ldots$$

where J_n is the n^{th} order Bessel function and $\phi_{\text{kick}} = \frac{V_{\text{lat}} t_p}{2\hbar}$ is the pulse area with pulse width t_p, for a square pulse.

Figure 4.23 shows the depth calibration data of the three-dimensional lattice. We measure the fractional population of the atoms in each momentum order as we vary the lattice laser power. We then fit some Bessel functions $[J_n(\beta P)]^2$ to the data, where P is the laser power and β is the variable to be fitted. From the fit, we can extract the beam waist of the lattice using equation 3.47 and calculate the power-to-depth conversion. Table 4.1 summarizes the measured beam waists and the power-to-depth conversions of the three optical lattices. For everyday operations, we do a one-point calibration check; if the depth calibration drifted too far, we typically walk the fiber mount and the retro-reflecting mirror to get it back.

Lattice beams	Beam waist (μm)	Power (mW)/Erec
Lattice 1 (z-axis)	98.93	6.855
Lattice 2 (y-axis)	101.17	7.169
Lattice 3 (x-axis)	120.62	10.190

Table 4.1: Beam waists and power-to-depth conversions extracted from the lattice depth calibration.

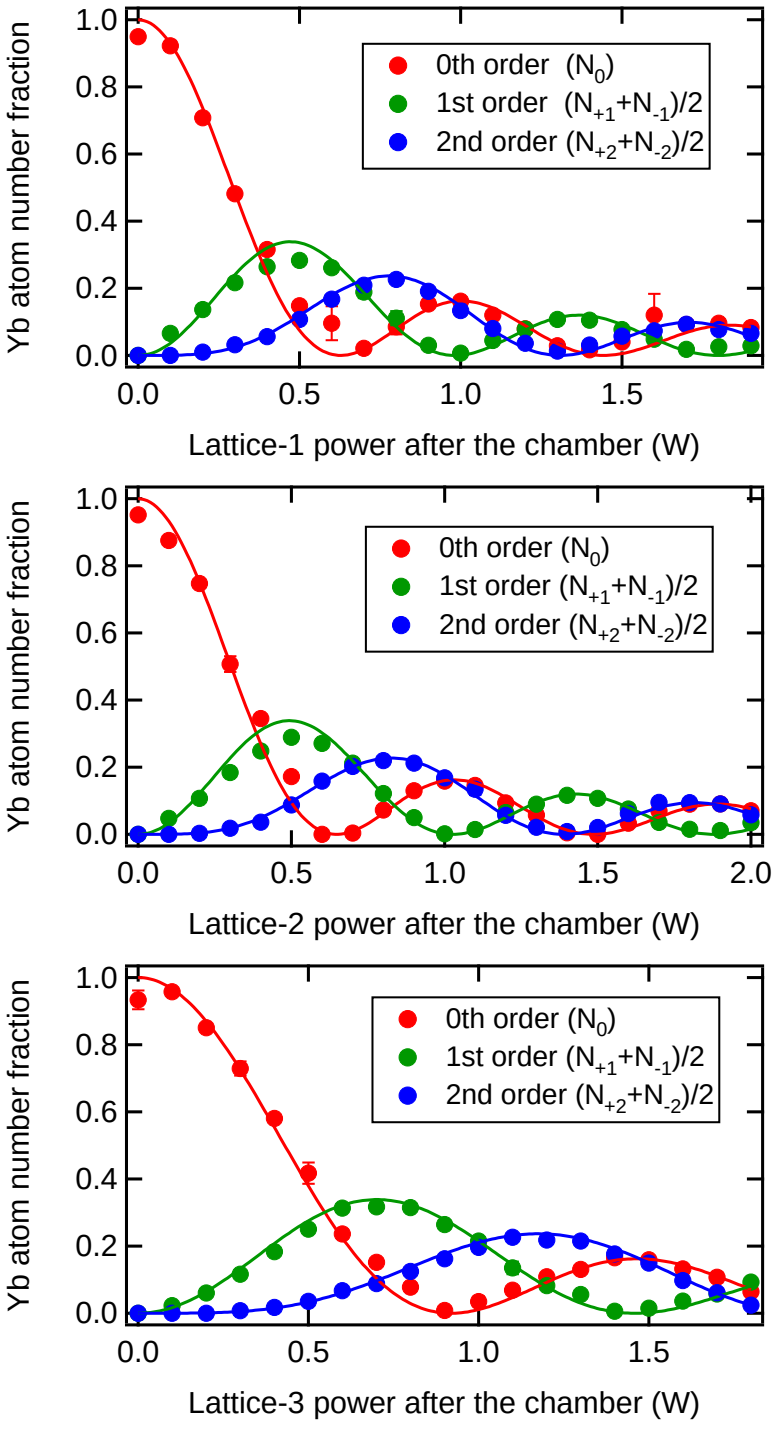

Figure 4.23: Lattice depth calibration of the three lattices. A short pulse of 8.5 μs is applied to the BEC and the atom number fraction in each momentum order is measured after a 30 ms ToF. The solid lines are the Bessel function fits.

4.5 Superfluid-to-Mott Insulator Transition

After the three-dimensional lattice is constructed and calibrated, we checked that our optical lattice is operational by observing the superfluid-to-Mott insulator transition predicted by the Bose-Hubbard model. The Bose-Hubbard model [60] describes the physics of spinless bosonic atoms with repulsive interaction in a lattice. The Hamiltonian of the Bose-Hubbard model is given by [46, 61–63]

$$H = -J \sum_{\langle i,j \rangle} \hat{a}_i^\dagger \hat{a}_j + \mu \sum_i \hat{n}_i + \frac{U}{2} \sum_i \hat{n}_i(\hat{n}_i - 1) \tag{4.10}$$

where $\hat{n}_i = \hat{a}_i^\dagger \hat{a}_i$ is the number of particles on site i, and $\langle i, j \rangle$ denotes the summation over all neighboring sites i and j. The first term describes the hopping of the particles between neighboring sites with the tunneling matrix element

$$J = -\int d^3x \; w(\mathbf{x} - \mathbf{x}_i) \left(\frac{\hbar^2}{2m} \nabla^2 + V_{\text{lat}}(\mathbf{x}) \right) w(\mathbf{x} - \mathbf{x}_j) \tag{4.11}$$

where $w(\mathbf{x} - \mathbf{x}_i)$ is the Wannier function. The second term describes the chemical potential μ of the system. The third term describes the repulsive interaction between the atoms on the same lattice site with

$$U = \frac{4\pi\hbar^2 a_s}{m} \int |w(x)|^4 d^3x. \tag{4.12}$$

There are two distinct ground states to the Bose-Hubbard Hamiltonian depending on the relative strength between the onsite interaction U and the tunnel-coupling J, which can be tuned with the lattice depth. If the tunneling term is dominant ($J \gg U$), the ground-state wavefunction for N bosons in a lattice is given by

$$|\Psi\rangle \sim \left(\sum_{i=1} \hat{a}_i^\dagger \right)^N |0\rangle \; . \tag{4.13}$$

Each atom is delocalized over the entire lattice because it can easily tunnel to neighboring sites. A macroscopic phase is well defined on each site and the system is superfluid. If the onsite interaction is dominant ($U \gg J$), the ground-state wavefunction is given by

$$|\Psi\rangle \sim \prod_{i=1} (\hat{a}_i^\dagger)^n |0\rangle \; . \tag{4.14}$$

Each atom is localized to a site since extra energy is needed to overcome the interaction energy if the atom tunnels to a neighboring site. In this case, the system has no macroscopic phase coherence and it is a Mott insulator.

Figure 4.24 shows our observation of the superfluid-to-Mott transition using the three-dimensional optical lattice. We load the BEC adiabatically into the three-dimensional lattice with an exponential ramp to a particular depth and then diabatically turn off all the trapping potentials. At low lattice depth, the system is in the superfluid phase and the macroscopic phase coherence leads to a distinct interference pattern after the atoms are released from the lattice. As the lattice depth is increased, the system becomes a Mott insulator due to the suppressed tunneling and thus no interference maxima are observed.

We also recovered the superfluid from a Mott insulator by holding the insulator for 10 ms and then linearly ramping down the lattice depth. Although the coherence and the interference are not fully recovered, we can still see some weak interference maxima around the center cloud.

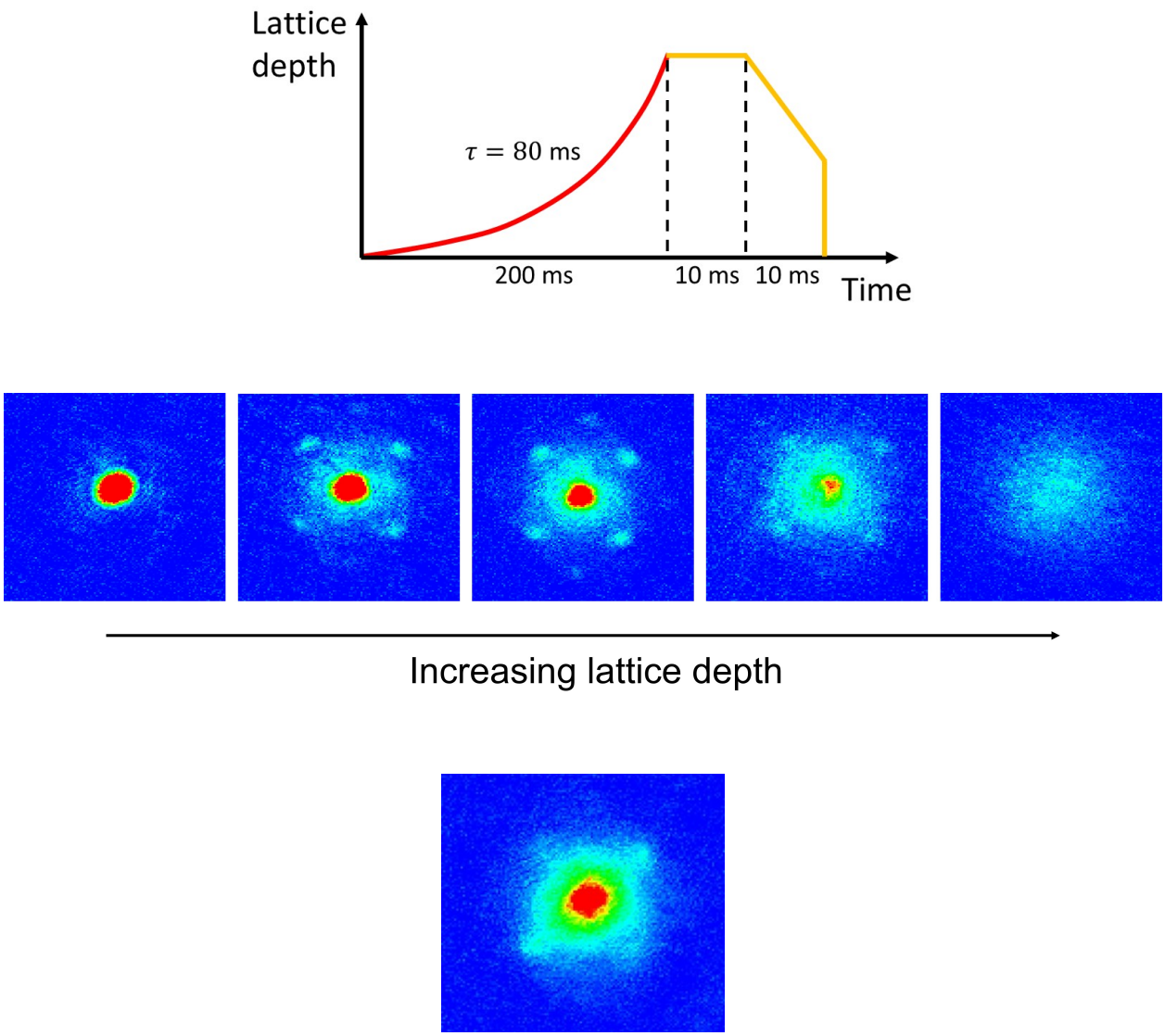

Figure 4.24: Superfluid-to-Mott insulator transition. (Top) The experimental sequence of the lattice depth. The red solid line is the ramp used to obtain the superfluid-to-Mott insulator transition. The yellow solid line is the ramp used to recover the superfluid from a Mott insulator. (Middle) Each square is a ToF absorption image of the atoms from a particular lattice depth. The distinct interference pattern disappears as the lattice depth is increased, indicating the transition from a superfluid to a Mott insulator. (Bottom) The superfluid is partially recovered after the lattice depth is ramped down.

Chapter 5

MANY-BODY DYNAMICAL DELOCALIZATION IN A KICKED ONE-DIMENSIONAL ULTRACOLD GAS

Despite the extensive study on the quantum kicked rotor and dynamical localization, the effect of interaction is still a long-standing question. This chapter will show that interactions lead to sub-diffusive delocalization in a one-dimensional kicked ultracold gas. We will first explain how we prepare and characterize our 1D systems, including measuring the background heating rate and the transverse excitation. We will then examine the quantum resonance and anti-resonance of a non-interacting QKR. Finally, we will present the observation of the many-body delocalization of the one-dimensional kicked rotor and show how the delocalization dynamics change with different experimental parameters.

This chapter covers the results reported in the publication See Toh *et al.*, Nature Physics 18, 1297 (2022) [64]. The theoretical mean-field modeling of interaction effects was performed by our theory collaborators − Ying Su, Xi-Wang Luo, and Chuanwei Zhang at The University of Texas at Dallas.

5.1 Preparation and Characterization of the System

To quantify the interaction of our 1D systems, we need to calibrate and characterize how the BEC is loaded into the 1D tubes and how they interact in the tubes. In this section, we will present the details of the experimental setup for the one-dimensional QKR. First of all, we need to measure the size of the prepared BEC to know its cross-section area and thus how many sites (and thus how many 1D tubes) of the two-dimensional lattice are filled. Figure 5.1 shows the trap frequency measurement of the ODT in which we obtain a BEC before loading the BEC into the two-dimensional lattice. We diabatically change the center

position of the ODT beam (i.e. using the "painting" setting) to displace the atom cloud in the horizontal plane (yz-plane) and then observe how it oscillates in the original trap. We measure the change of the atom cloud's position with varying hold times and fit a sinusoidal function to the data to extract the trap frequency along each axis. The vertical (x-axis) trap frequency is measured with a similar method except the atom cloud is displaced by simply releasing and recapturing the atoms. For all the kicked rotor described in this thesis, we prepare a BEC containing 1.5×10^5 atoms of ^{174}Yb in a crossed ODT and measured the trap frequencies to be $\{\omega_{0x}, \omega_{0y}, \omega_{0z}\} = 2\pi \times \{145, 16, 53\}$ Hz. The corresponding chemical potential is $h \times 1.1$ kHz and Thomas-Fermi radii $\{2.4, 22, 6.6\}$ μm.

The BEC is then transferred into a two-dimensional optical lattice formed by two pairs of counter-propagating laser beams, where atoms reside in a set of 1D tubes with negligible intertube tunneling, as shown in Figure 5.2(a). To suppress optical interference between different arms of the lattice, we maintain orthogonal linear polarization for each pair of lattices and separate their optical frequencies by 40 MHz using acousto-optic modulators. The depths of the lattices are calibrated using single-pulse Kapitza-Dirac diffraction, and we measure the lattice-beam waist to be $\{w_x, w_y, w_z\} = \{121, 101, 99\}$ μm, which are much larger than the BEC size.

We load the BEC from the ODT to the two-dimensional lattice by ramping up the lattice exponentially in 100 ms with an exponential time constant of 20 ms. We check the adiabaticity of this ramp by immediately loading the BEC back to the ODT using the same ramp in reverse and comparing the final BEC fraction with the initial value. Using this method, we measure about 70% BEC fraction after the forward and reverse ramps, suggesting that the BEC fraction in the two-dimensional lattice is about 85% [64]. This is a lower bound because tunneling is strongly suppressed for lattice above $s_\perp \simeq 20$ and therefore limits the coherence between tubes.

Our lattice has spatial period of 1073 nm/2 $= \pi/k_L$ and corresponding recoil frequency $\omega_{\text{rec}} = \hbar k_L^2/2m = 2\pi \times 1$kHz. Each of the two transverse lattices has depth $s_\perp E_{\text{rec}}$. The typical lattice depth we use for the 1D QKR experiment is $s_\perp = 106$, which has a transverse

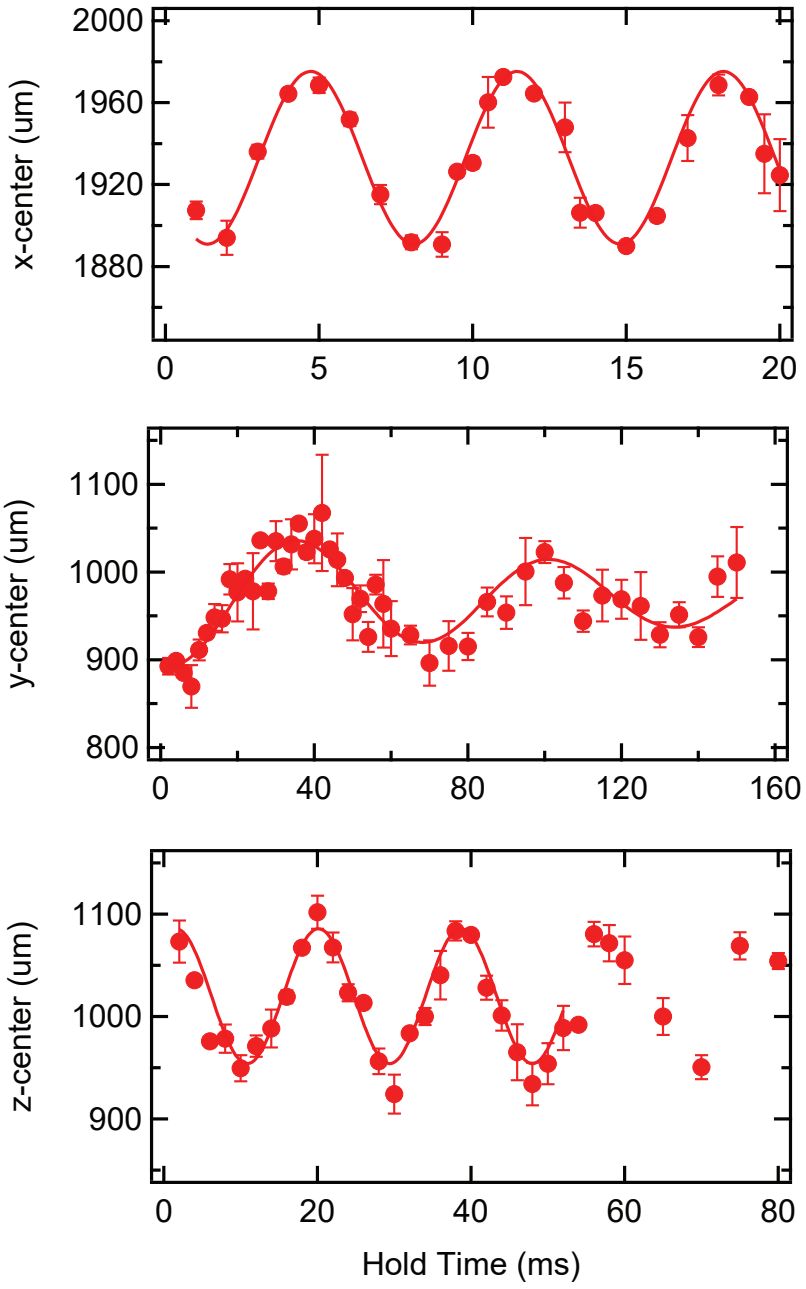

Figure 5.1: Trap frequencies of the optical dipole trap. We measure the trap frequencies of the ODT in which we obtain a BEC before loading it into the two-dimensional lattice. The solid lines are sinusoidal-function fits. The measured trap frequencies are $\{\omega_{0x}, \omega_{0y}, \omega_{0z}\} = 2\pi \times \{145, 16, 53\}$ Hz.

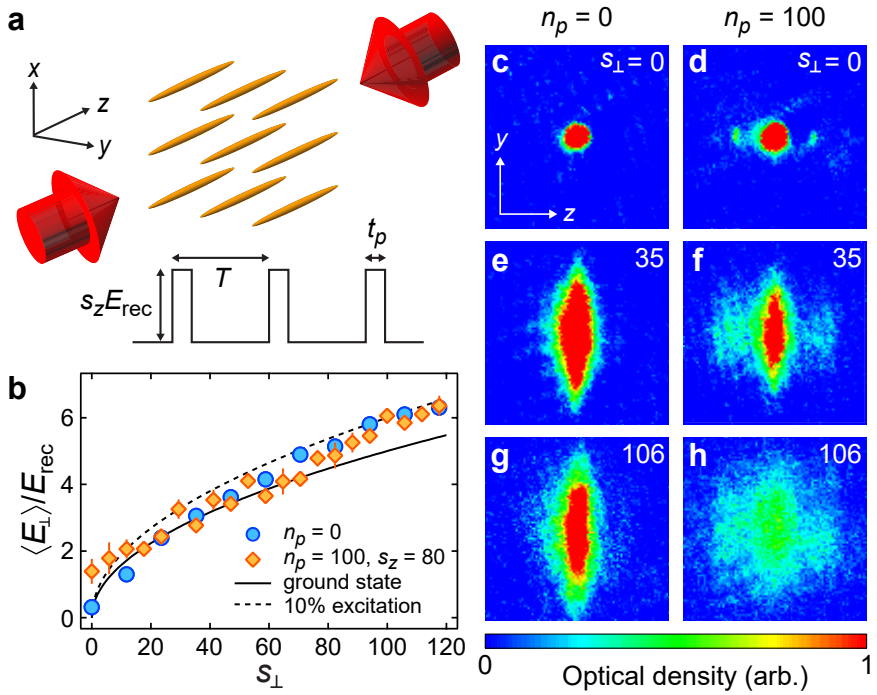

Figure 5.2: Experimentally realizing the interacting 1D QKR system. (a) The BECs are loaded into the 1D tubes before the periodic kicking pulses are applied along the axial (z) direction. (b) Mean transverse energy $\langle E_\perp \rangle$ as a function of $s_\perp$ for no kick and 100 kicks with $s_z = 80$ and $(t_p, T) = (2, 105)\,\mu$s. The solid line shows the calculated transverse ground-state energy and the dashed line that for 10% occupation of the first transverse excited state. Error bars show 1 s.e.m (not visible when smaller than the marker size). (c−h) Time-of-flight atom absorption images after 0 (left column) and 100 (right column) kicks for different lattice depth $s_\perp$. Each image spans the momentum range 10 $\hbar k_L \times 10\ \hbar k_L$.

trap frequency of $\omega_\perp = 2\pi \times 20.5$ Hz for the central tube and an axial trap frequency of $\omega_z = 2\pi \times 64$Hz. The transverse oscillator length is $a_\perp = \sqrt{\hbar/m\omega_\perp} \simeq 53$nm.

From the measured Thomas-Fermi radii of the BEC, we know the cross-section area overlapped with the lattice and estimate that the atoms are loaded into about 570 horizontal 1D tubes. From the initial axial size of the BEC of 27 μm for $s_\perp = 106$, we estimate a peak particle number of $N_{\text{atom}} = 650$ and an initial 1D peak density of $\bar{n}_{1\text{D}} = 24\mu\text{m}^{-1}$ [64].

After the BEC is loaded into the two-dimensional lattice, we exponentially ramp down the ODT in 50 ms with a time constant of 10 ms. We measure the background heating rate of the atoms by measuring the growth of mean axial energy after some variable hold time in the two-dimensional lattice of $s_\perp = 106$, as shown in Figure 5.3. The background heating rate is $6E_{\text{rec}}/\text{s}$, which is negligible on the timescale ($\sim$ 100ms) of our QKR experiments. The lifetime of the atoms in the two-dimensional lattice is also measured in a similar way by keeping track of the atom number. Figure 5.4 shows that the lifetime of the atoms in the lattice is about 4 seconds. Also, the photon-scattering rate from the transverse lattice is estimated to be < 0.1 s^{-1} for $s_\perp = 106$, suggesting that any observed residual heating is from technical noise.

Once the 1D systems are prepared, we apply a series of standing-wave pulses along the axial direction, with kick period T and pulse length t_p, as shown in Fig. 5.2a. The kick pulses are generated by triggering a function generator (Stanford Research Systems DS345) in burst mode. The function generator will output a voltage pulse when triggered, and the voltage is sent to the radio-frequency switch on the IQ modulator that drives the AOM for the kicking-lattice laser beam. The length of each pulse can be controlled through the frequency setting of the function generator. The duty cycle, and hence the kick period T of the pulse, is set by the triggering function sent to the function generator. The triggering function is programmed in Cicero using the equation

$$2.5 \times \{sign(\sin(2\pi f t + \phi)) + 1\} \tag{5.1}$$

where f is the kick frequency $1/T$ and ϕ is an overall phase. The prefactor of 2.5 and the

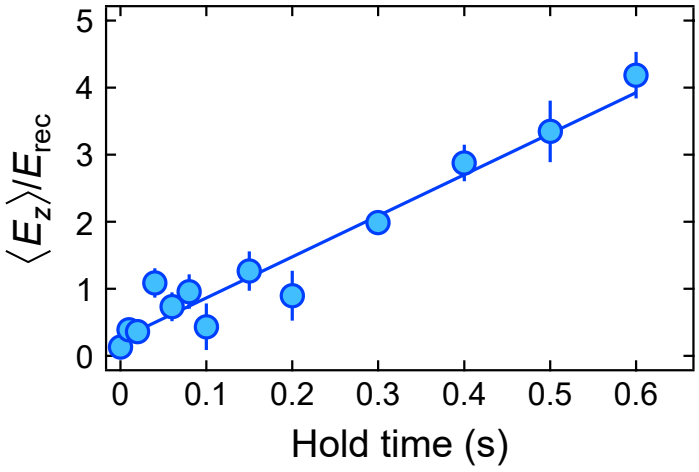

Figure 5.3: Background heating rate in the two-dimensional lattice. We measure the energy of the 1D tubes of depth $s_\perp = 106$ without the kick pulses after different hold times. The linear fit (solid line) shows that the background heating rate is $6E_{\rm rec}/s$.

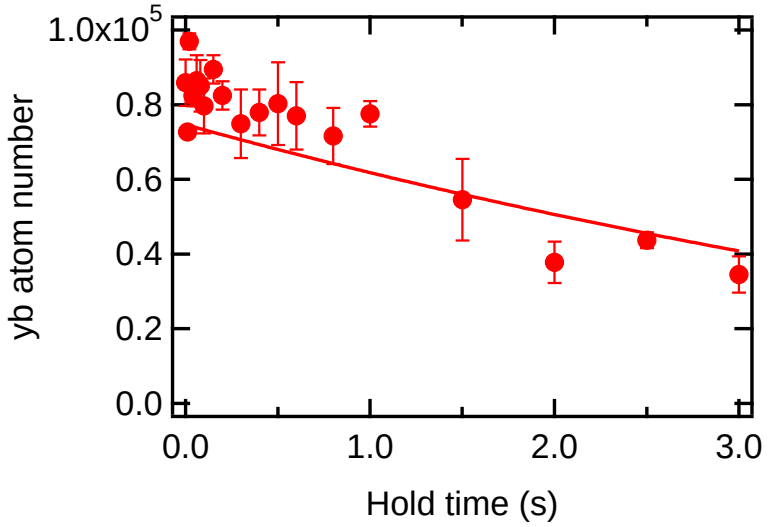

Figure 5.4: Lifetime of the atoms in the two-dimensional lattice. The plot shows the total atom number in a two-dimensional lattice of depth $s_\perp = 106$. The solid line is an exponential fit. The lifetime of the atoms is about 4 seconds.

extra term of +1 are there so that the total voltage is non-negative and ranges from $0-5$V.

We probe the system by diabatically turning off all the optical potentials after some pulse number n_p and taking a time-of-flight absorption image of the atoms. From the axial and transverse momentum distributions of the atoms, we can calculate the axial and transverse energies of the system by determining the number of atoms in each order of diffraction using the equation

$$\langle E_z \rangle = \frac{\langle p^2 \rangle}{2m} = \frac{1}{2m} \frac{\sum_n N_n p_n^2}{\sum_n N_n} = \frac{1}{2m} \frac{\sum_n N_n (2n\hbar k_L)^2}{\sum_n N_n} \tag{5.2}$$

$$= \frac{\hbar^2 k_L^2}{2m} \frac{\sum_n N_n 4n^2}{\sum_n N_n} = E_{\text{rec}} \frac{4\sum_n N_n n^2}{\sum_n N_n}. \tag{5.3}$$

where N_n is the number of atoms in the n^{th} momentum state. For a continuous momentum distribution, the sum is replaced by an integral over all the momentum states.

The strong confinement of the 1D tubes $\omega_\perp \gg \omega_{\text{rec}}$ suppresses two-body scattering from the axial to the transverse directions, as shown in Fig. 5.2b. With 100 kicks of $s_z = 80$, we observe less than 10% excitation in the transverse direction. Figure 5.2(c−h) show the absorption images of the atoms after 0 and 100 kicks with different interactions controlled through the transverse confinement $s_\perp$. The transverse (y) momentum does not change much with increasing pulses, consistent with the low transverse excitation. However, the axial (z) momentum increases drastically, which is a sign of many-body dynamical delocalization.

5.2 Non-interacting QKR: Quantum Resonance and Anti-resonance

Before discussing the effect of interactions on dynamical localization, we will first look at some special cases of the non-interacting QKR. The disorder in the Anderson model is emulated in the QKR in the pseudorandom phases of different momentum sites. This pseudo-randomness only holds if the phases are irrational multiple of 2π, or else they will result in quantum resonances or anti-resonances.

The unitary operator of the QKR for one period consists of a kick term and a free evolution term

$$U = e^{-iK\cos\theta/\bar{k}} e^{-ip^2/2\bar{k}}\,. \tag{5.4}$$

Let us examine the free evolution term that controls the phases of the different momentum states $|m\rangle$.

$$e^{-ip^2/2\hbar}|m\rangle = e^{-i(m\hbar)^2/2\hbar}|m\rangle = e^{-im^2\hbar/2}|m\rangle \tag{5.5}$$

$$= e^{-im^2(2\pi l)/2}|m\rangle = e^{-im^2\pi l}|m\rangle \tag{5.6}$$

$$= (-1)^{m^2 l}|m\rangle \tag{5.7}$$

where we have written $\hbar = 2\pi l$ with integer l. We can see that when l is even, the free evolution becomes unity. This means that the effect of multiple pulses is the same as that of a single larger pulse with the same combined pulse area. This is referred to as the quantum resonance of the QKR. When l is odd, the phases acquired are different for odd and even m. The odd m states acquire a multiplicative factor of -1, resulting in an oscillatory behavior of the energy of the system. This is referred to as the quantum anti-resonance of the QKR where the effect of a pulse is canceled by the next pulse.

Since the kick period T is the parameter we control experimentally, it is conventional to define a timescale of the system T_{Talbot} such that the kick period coincides with the first quantum resonance. This can be derived using the resonance condition $\hbar = 2\pi l$ and equation 2.17

$$T = \frac{\pi l}{4\omega_{\text{rec}}} = \frac{l}{2}T_{\text{Talbot}} \tag{5.8}$$

where the Talbot time corresponds to the first quantum resonance at $l = 2$

$$T_{\text{Talbot}} = \frac{\pi}{2\omega_{\text{rec}}}\,. \tag{5.9}$$

It is thus straightforward to show that kick periods of integer multiples of Talbot time correspond to quantum resonances, while kick periods of half-integer multiples of Talbot time correspond to quantum anti-resonances. The pseudorandom condition of the phases to simulate the Anderson disorder is satisfied when the kick period is incommensurate with the Talbot time.

The recoil frequency of the atoms in our lattice laser beams is $\omega_{\text{rec}} = 2\pi \times 1\,\text{kHz}$ and thus the Talbot time of our system is about 250μs. Figure 5.5 shows the observation of the

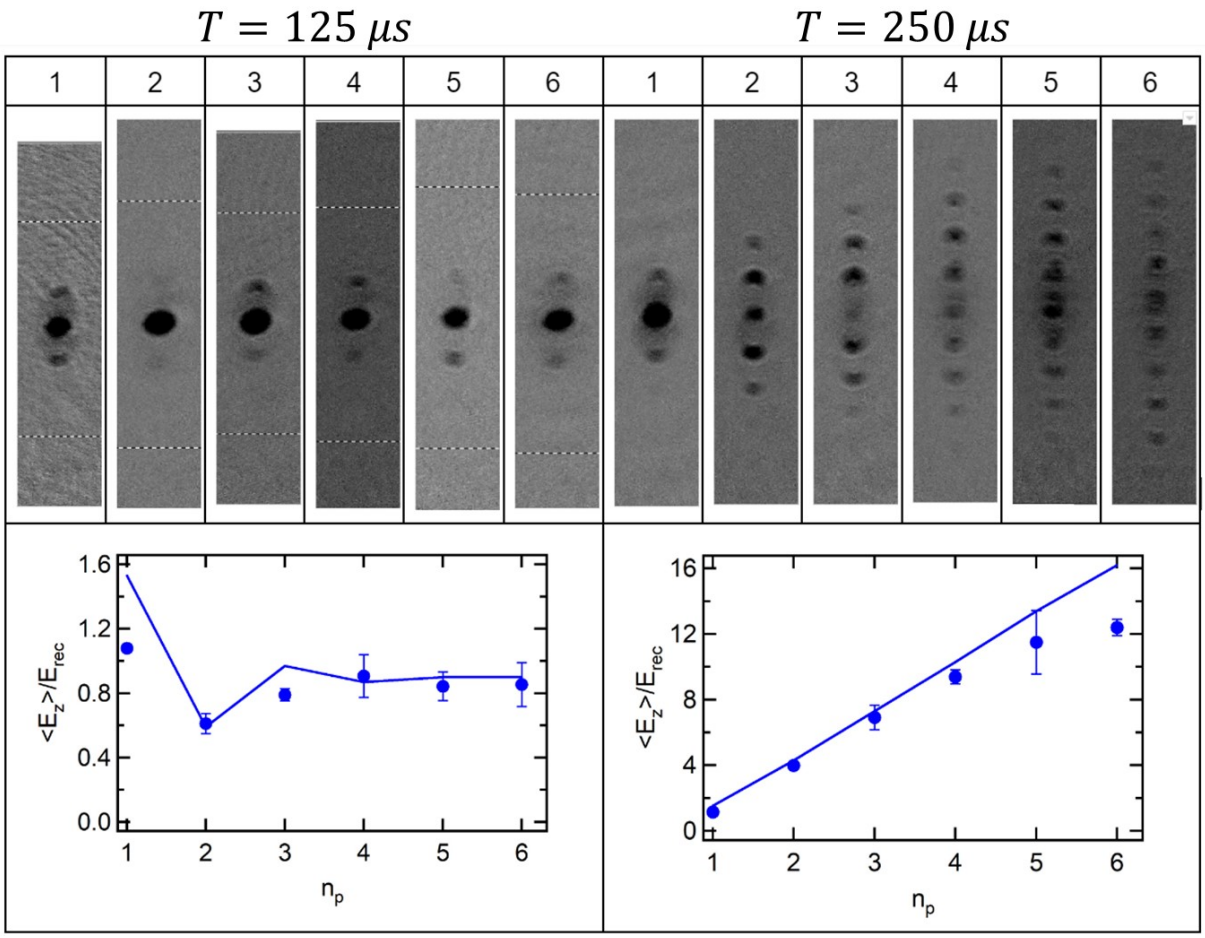

Figure 5.5: Quantum anti-resonance and quantum resonance. The data show the absorption images and the mean energy of atoms with increasing pulse number n_p for the quantum anti-resonance (left) and the quantum resonance (right). The pulse length is $t_p = 5\mu$s, and the pulse area is $\phi_{\text{kick}} = 0.86$. The solid lines are the theory curves solved with an initial momentum width of 10 nK. These calculations were performed by Katie McCormick.

quantum anti-resonance and resonance with a kick period of 125 μs and 250 μs, respectively. The data are taken by applying some kicks to the BEC in the ODT, and the time-of-flight absorption images show the momentum distributions of the atoms after some pulse number n_p. We can see from the images that for the quantum anti-resonance case, the system alternates between two different Floquet states and then reaches a steady state. This is also shown in the mean energy of the system − it oscillates initially and then saturates at some value. The short oscillatory behavior observed, instead of a long oscillation in the ideal case, is due to the decoherence of the system from the initial momentum width and the weak interaction of the BEC. On the other hand, for the quantum resonance case, the atoms are diffracted up to large momentum states because of the increasing effective pulse area seen by the atoms as the pulse number is increased.

Apart from the quantum resonances and anti-resonances, there are also fractional resonances when the kick period is a rational multiple of the Talbot time. These fractional resonances are the results of the superposition of q copies of the initial wave packet, separated by $2\pi/q$ [65]. Figure 5.6 shows the mean energy of the atoms after 4 kicks as a function of the kick period T. The large peak at 250 μs is the quantum resonance while the minimum around 125 μs is the quantum anti-resonance. The other local maxima around 62.5 μs, 100 μs, 156.25 μs, and 187.5 μs are the fractional resonances corresponding to $(1/4)T_{\text{Talbot}}, (2/5)T_{\text{Talbot}}, (5/8)T_{\text{Talbot}}$, and $(3/4)T_{\text{Talbot}}$, respectively.

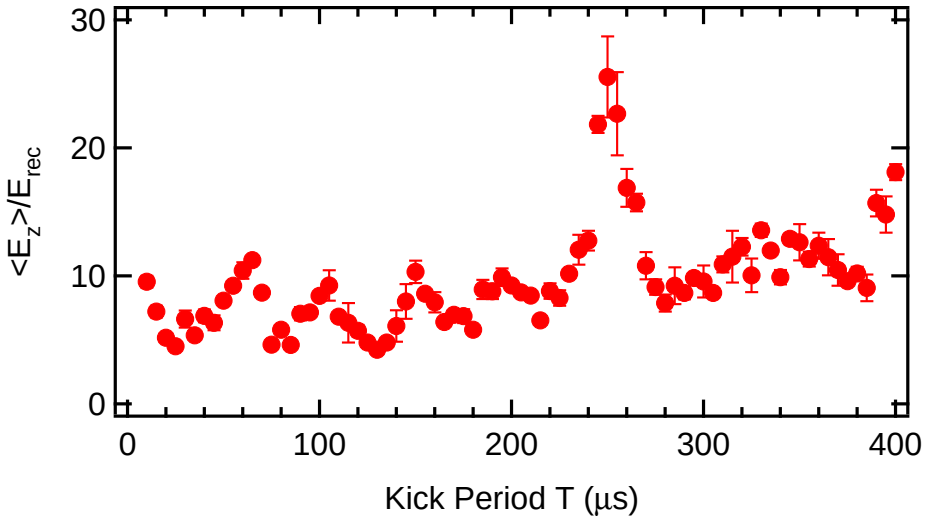

Figure 5.6: Fractional resonances. The plot shows the mean energy of the system after 4 pulses as a function of the kick period T. The maxima and minima show the quantum resonance, anti-resonance, and fractional resonances of the system. The pulses were applied with the BEC in the ODT, and the experimental settings used are $t_p = 4\,\mu$s, $s_z = 120$, $\phi_{\text{kick}} = 1.508$, and tof = 15 ms.

5.3 Interacting QKR: Many-body Dynamical Delocalization

We will now present our observation of the dynamical delocalization in a kicked one-dimensional ultracold gas in the presence of interaction [64]. As shown before, a classical kicked rotor displays chaotic and diffusive dynamics above a critical kick strength [66, 67], while a quantum kicked rotor with the same kick strength can display dynamical localization due to quantum interference [68]. The mapping of the Floquet dynamics of the QKR to the Anderson model [31] shows that the pseudorandom phases of the QKR simulate the disorder and lead to dynamical localization.

While the dynamical localization of the QKR has been experimentally studied extensively [19–25, 69], the effect of interaction on dynamical localization has remained unexplored till now. The effects of interactions have been studied both experimentally and theoretically in position space [70–72] but not in the momentum space. There are conflicting theoretical predictions: mean-field calculations for interacting BEC predicts delocalization with sub-diffusive dynamics [40, 73], while the low-energy approximation based on Luttinger liquid theory of a kicked one-dimensional (1D) Lieb-Liniger gas predicts the persistence of dynamical localization [35]. It is challenging to understand the interaction effect on dynamical delocalization because the infinite long-range interaction in the momentum space is fundamentally different from the short-range interaction in position-space Anderson lattices [35, 36, 40, 70–78].

Here we perform the first experimental study of the effects of interactions on dynamical localization. We observe that interactions destroy the dynamical localization and induce sub-diffusive dynamics. We control the contact interactions of our periodically kicked 1D bosonic system with the transverse confinement of the two-dimensional lattice and study the dynamical delocalization across various experimental parameters. The sub-diffusive delocalization dynamics do not seem to depend on the various experimental parameters, but the onset time of delocalization is earlier with larger interaction strengths or kick strengths. We will also present the results of the theoretical models using the mean field and Hartree-

Fock-Bogoliubov approaches performed by our collaborators − Ying Su, Xi-Wang Luo and Chuanwei Zhang at The University of Texas at Dallas.

Using the mean-field theory, the many-body dynamics of our system and the QKR wavefunction Φ are governed by the non-linear Gross-Pitaevskii (GP) equation:

$$i\hbar\partial_\tau\Phi(\theta,\tau) = \left(-\frac{\hbar^2}{2}\partial_\theta^2 - K\cos\theta\sum_{n_p}\delta(\tau-n_p) + \frac{1}{2}\omega_\theta^2\theta^2 + g|\Phi(\theta,\tau)|^2 \right)\Phi(\theta,\tau) \qquad (5.10)$$

with the dimensionless parameters $\theta = 2k_L z$, $\tau = t/T$, where $\hbar = 8\omega_{\rm rec}T$ is the dimensionless effective Planck constant. The first term on the right describes the kinetic energy and free evolution of the atoms. The second term describes the standing-wave pulses with kick strength $K = 4s_z\omega_{\rm rec}^2 t_p T$, and the third term the harmonic confinement along the tubes with dimensionless axial frequency $\omega_\theta = \omega_z T$. The last term describes the nonlinear contact interaction between the atoms with interaction constant $g = 2\bar{g}k_L\hbar T/\hbar = \hbar^2\frac{k_L a_s}{(k_L a_\perp)^2}$.

We control the interaction strength $gn_{\rm 1D}$ through the transverse confinement of the 1D tubes where $n_{\rm 1D} = |\Phi(0,0)|^2 = \bar{n}_{\rm 1D}/2k_L$ is the dimensionless initial peak density. Because of the non-uniform load into the 1D tubes, we take into account the variation of atom number in different tubes when calculating the interaction strength, and the wave function of the system is normalized as $\int d\theta|\Phi(\theta,\tau)|^2 = N_{\rm atom}$. Because we cannot tune the scattering length of the Yb atoms using a Feshbach resonance, our weakest interacting system is a BEC in the ODT without the two-dimensional lattice. In this case, we adjust the $a_\perp$ in the interaction constant to match the measured chemical potential of the BEC in the ODT, which gives us an effective 1D interaction strength $gn_{\rm 1D}^{\rm eff}$ of the 3D BEC.

Figure 5.7 shows the effects of interactions on the dynamical localization. The weak interaction case ($gn_{\rm 1D}^{\rm eff} = 3.9$) is realized by kicking the BEC in the ODT. We can see from the absorption images (Fig. 5.7 a) and the momentum distribution (Fig. 5.7 c,e) that when the interaction is weak, the momentum distribution freezes after some initial dynamics, indicating dynamical localization. This is also evident from the saturation of mean axial energy $\langle E_z\rangle$ (Fig. 5.7 g) after some pulse number n_p. The exponential functions in the momentum distribution plots show the localized function $e^{-|p|/\xi}$ with the theoretical

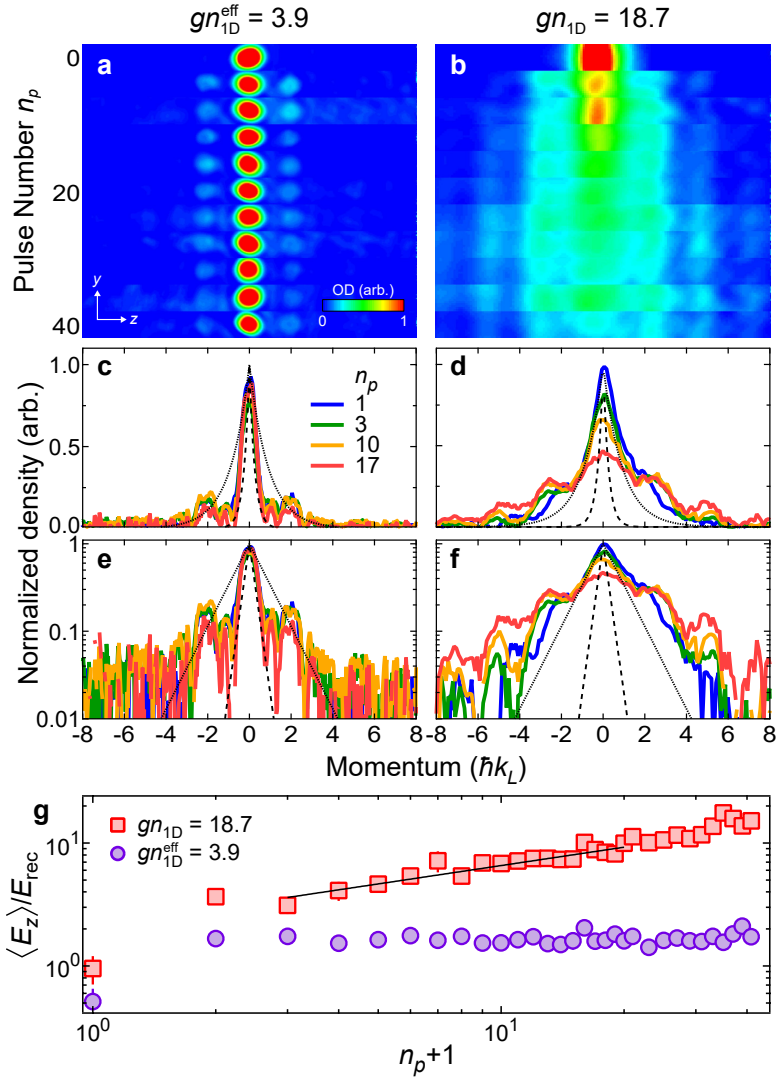

Figure 5.7: Interaction-driven dynamical delocalization. (a−b) Sequences of time-of-flight absorption images for localized (left column) and delocalized (right column) cases with low and high interaction strength gn_{1D} respectively. The kicking parameters used are $k = 5.26, K = 5.3$, and $(t_p, T) = (2, 105)\,\mu$s. (c−f) Axial momentum distributions after some kick numbers n_p on a linear scale (c, d) and logarithmic scale (e, f). The dashed and dotted lines are exponential functions with theoretical and measured localization lengths, respectively. (g) Evolution of the axial kinetic energy. The solid line is a power-law fit, with an exponent value of 0.36.

localization length $\xi = K^2/4\bar{k}^2 = 0.25$ in unit of $\hbar k_L$ (dashed line) and the measured localization length $\xi = 0.92$ corresponding to the measured saturation energy $\langle E_z \rangle = 1.7 E_{\rm rec}$ (dotted line). The difference between the measured and theoretical momentum distribution arises from the non-zero interaction of the BEC and the narrow initial momentum width compared with $2\hbar k_L$. For the strong interaction case ($gn_{\rm 1D}^{\rm eff} = 3.9$), the atoms populate higher momentum states with increasing pulse numbers (Fig. 5.7 b,d,f), indicating dynamical delocalization. The power-law fit to the energy growth (Fig. 5.7 g) also shows that the delocalization dynamics is sub-diffusive with an exponent of 0.36. The striking contrast between the two cases confirms that interactions do indeed destroy dynamical localization and lead to sub-diffusive dynamics.

We study the dynamical delocalization with various parameters to understand their effect on the sub-diffusive exponent and the onset time of delocalization. Figure 5.8a shows the delocalization behavior for different kick strengths (tuned through s_z) and interaction strengths (tuned through $s_\perp$). The dynamics respond strongly to kick strength K with the delocalization beginning earlier with stronger K. Although our 1D tubes have an axial harmonic confinement, it is not a prerequisite to observe the delocalization dynamics because the onset of delocalization can happen within the first ten pulses for the largest K we used, much earlier compared to the axial oscillation period (marked by the yellow vertical bar). The monotonic growth of the mean axial energy with K is also evident in Figure 5.8b which corresponds to a vertical cut of the data in Fig. 5.8a (fixed $n_p = 15$ and $gn_{\rm 1D} = 18.7$).

Figure 5.8c shows the delocalization behavior with different interaction strengths controlled through the lattice confinement $s_\perp$. Stronger confinement increases the density of the atoms in the tube and thus the interaction strength. We can see from the plot that the system is localized with weak interaction strength and delocalized with large interaction strength. As the interaction strength is increased, the delocalization is stronger and the onset of the delocalization is also earlier. The monotonic growth of the mean axial energy with $gn_{\rm 1D}$ is also evident in Figure 5.8d which corresponds to a vertical cut of the data in Fig. 5.8c (fixed $n_p = 100$ and $K = 2.6$).

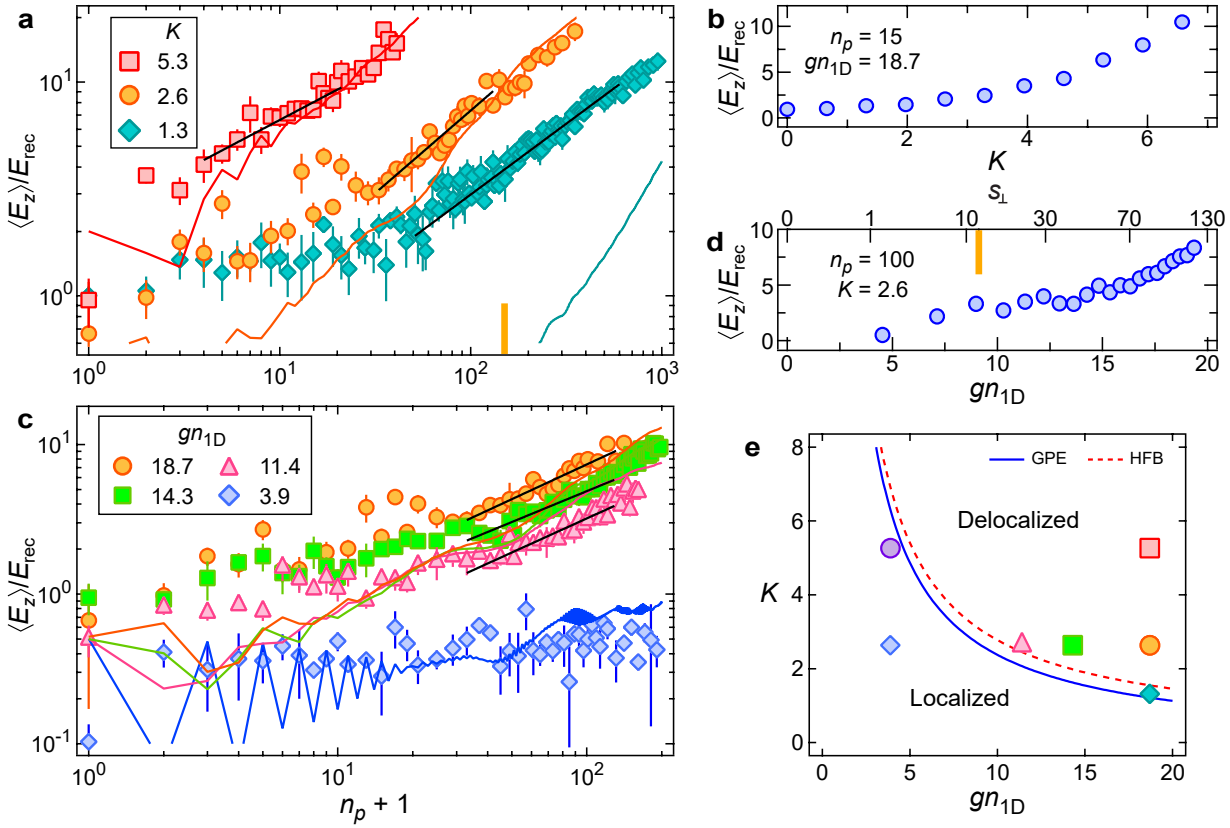

Figure 5.8: Delocalization dynamics with different interaction and kick strengths. The kick parameters used are $(t_p, T) = (2, 105)\,\mu$s and $\hbar = 5.26$. (a) Evolution of $\langle E_z \rangle$ with pulse number n_p for different kick strengths and fixed $gn_{1D} = 18.7$. The yellow vertical bar marks the axial oscillation period. The black solid lines are power-law fits. The colored solid lines are the corresponding numerical simulations using the GP equation. (b) $\langle E_z \rangle$ after 15 kicks as a function of K. (c) Evolution of $\langle E_z \rangle$ for four different interaction strengths with $K = 2.6$. The $gn_{1D}^{\text{eff}} = 3.9$ data are obtained in the 3D system. (d) $\langle E_z \rangle$ after 100 kicks as a function of gn_{1D}. The yellow bar marks the intertube tunneling time of 21 ms ($n_p = 200$). (e) $K - gn_{1D}$ phase diagram of the system for $\hbar = 5.26$. The lines are the localization-delocalization transition boundaries solved using the GP (solid) and HFB (dashed) equations. The filled markers correspond to the data from (a), (c), and Fig. 5.7(g).

We fit a power-law function $E_0 n_p^\alpha$ to the mean energy $\langle E_z \rangle$ to understand the sub-diffusive character of the dynamics. The range of the fit is restricted by the atom loss and the axial oscillation period. As shown in Fig. 5.9, the atom loss is significant when the mean kinetic energy is above $10E_{\rm rec}$ due to the finite trap depth. The exact fit range chosen with these restrictions is listed in Table 5.1, and the analysis of the sub-diffusive dynamics is shown in Figure 5.10. Our fit results for α lie in the range of $0.36 - 0.80$, indicating sub-diffusive dynamics. This measurement is consistent with the prediction in Ref. [40], but larger than the predicted value of $0.3 - 0.4$ in Ref. [76]. We also do not observe any clear functional dependence of the exponent on the kick strength or the interaction strength. There is, however, a trend in the onset time of delocalization n_p^*, which we define as when the energy of the system reaches $2.5E_{\rm rec}$, i.e. $E_0(n_p^*)^\alpha = 2.5E_{\rm rec}$. As shown in Fig. 5.10, the onset time of delocalization is earlier with a stronger kick or interaction strength.

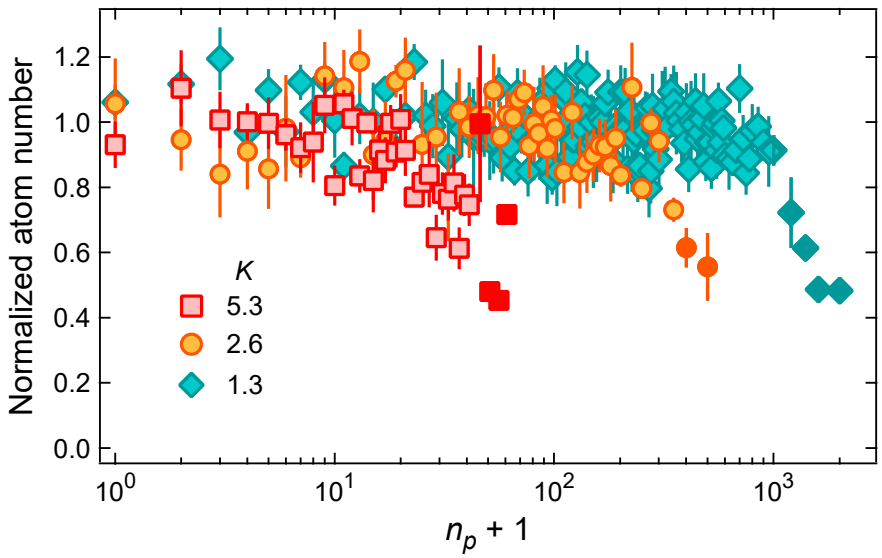

Figure 5.9: Evolution of atom number. The plot shows the normalized atom number as a function of pulse number n_p for the data corresponding to Fig. 5.8(a). For each K, the darker markers correspond to the data points not included in Fig. 5.8(a). Error bars show 1 standard error of the mean (s.e.m.).

Table 5.1: **Ranges of pulse numbers used for fitting the data, corresponding energy ranges, and the number of fits.**

Dataset	Figure	Beginning n_p	Ending n_p	Beginning $\langle E_z \rangle$	Ending $\langle E_z \rangle$	Number of fits
(i)	3(a) $K = 1.3$	50-70	500-600	$1.6 - 3.4E_{\mathrm{rec}}$	$8.0 - 9.8E_{\mathrm{rec}}$	99
(ii)	3(a) $K = 2.6$	30-50	110-130	$3.1 - 4.4E_{\mathrm{rec}}$	$7.7 - 10.1E_{\mathrm{rec}}$	18
(iii)	3(a) $K = 5.3$	3-8	15-20	$4.1 - 7.2E_{\mathrm{rec}}$	$8.2 - 11.3E_{\mathrm{rec}}$	36
(iv)	3(b) $gn_{\mathrm{1D}} = 11.4$	30-50	110-130	$1.6 - 2.4E_{\mathrm{rec}}$	$3.2 - 4.4E_{\mathrm{rec}}$	30
(v)	3(b) $gn_{\mathrm{1D}} = 14.3$	30-50	110-130	$2.3 - 3.1E_{\mathrm{rec}}$	$5.3 - 6.5E_{\mathrm{rec}}$	36
(vi)	3(b) $gn_{\mathrm{1D}} = 18.7$	30-50	110-130	$3.1 - 4.4E_{\mathrm{rec}}$	$7.7 - 10.1E_{\mathrm{rec}}$	18

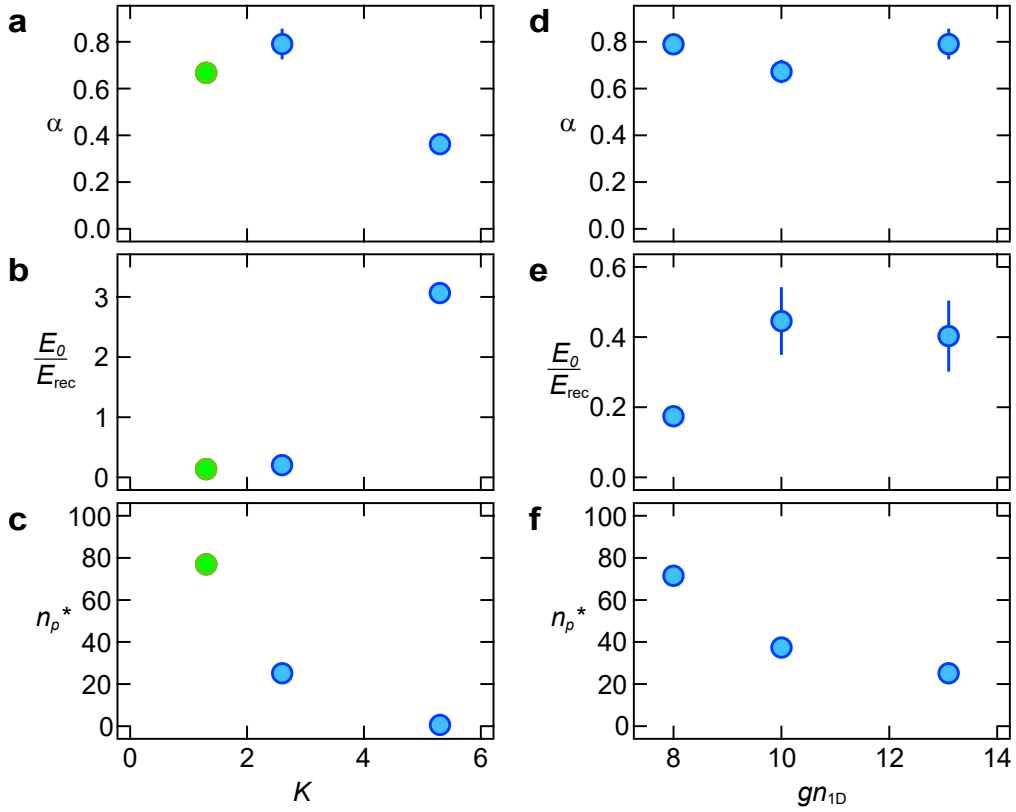

Figure 5.10: Analysis of the delocalization dynamics. Exponent α, prefactor E_0, and the onset time of delocalization n_p^* for the corresponding data in Fig. 5.8. The different color (green) of the $K = 1.3$ data point indicates that the fitting range of the data goes beyond the axial oscillation period. Error bars show 1 s.d. (not visible when smaller than the marker size).

The colored lines in Fig. 5.8a,c are numerical mean-field calculations of the dynamics. We find that for a given interaction strength gn_{1D}, the system enters the delocalized phase earlier when K is larger than a critical value K_c. This can also be seen from the phase diagram in Fig. 5.9e where we plot the boundary curves that separate the localized and delocalized phases using the mean-field Gross-Pitaevskii equation (GPE) and Hartree-Fock-Bogoliubov (HFB) approaches. For a larger gn_{1D}, the K_c is smaller, implying that dynamical delocalization is easier with stronger interactions. The numerical simulation captures the

dynamics better when the system is in the deep localization or delocalization phase but deviates from the experimental data around the boundary of localization-delocalization phases. This failure of the mean-field theory around the phase transition boundary is potentially due to the depletion of the BEC fraction. Furthermore, for our system, the real-space contact interaction maps to an infinite long-range interaction in the momentum space leading to a strong competition between the disorder potential and the interaction-induced infinite long-range hopping.

5.4 Delocalization Dynamics with Different Kick Periods and Atom Numbers

We also tuned other experimental parameters and found that the interaction-driven dynamical delocalization is a general feature of our system. Figure 5.11 shows the similar delocalization behavior for different kick periods T ranging from 20 to 125 μs while keeping the kick strength constant. Particularly, we note that interaction-induced dynamical delocalization is also observed at the quantum anti-resonance condition ($T = 125\,\mu$s), where the dynamics are oscillatory in the non-interacting case.

Apart from the transverse lattice depth, we can also control the interaction using the atom number N_{atom}. We repeat the experiment in a vertical-tube configuration and let some atoms fall out of the tubes before applying the kicks. The ODT is not extinguished during the kicks to keep the remaining atoms in the tubes. Figure 5.12 shows the delocalization dynamics of the system with different atom numbers in the fixed transverse lattice depth. Consistent with our other observations, the delocalization is stronger with larger kick strength or interaction strength.

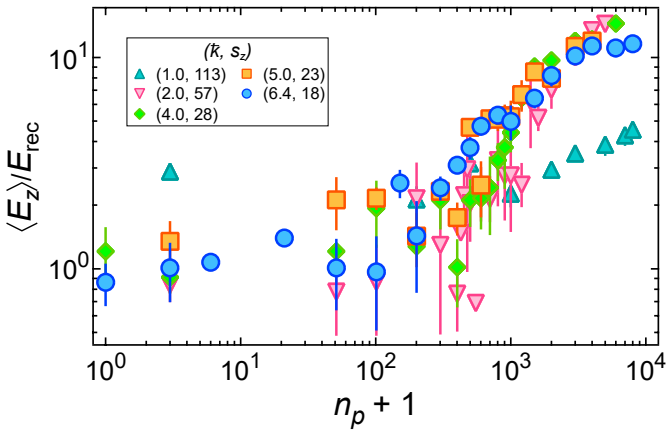

Figure 5.11: Interaction-driven delocalization using various kick periods. The data show the mean energy as a function of pulse number for different kick periods and kick lattice depth s_z, while keeping the kick strength $K = 0.7$ constant. The kick periods used are $T = \{20, 40, 80, 100, 125\}\,\mu$s, corresponding to $\bar{k} = \{1.0, 2.0, 4.0, 5.0, 6.4\}$. Error bars show 1 s.e.m. (not visible when smaller than the marker size).

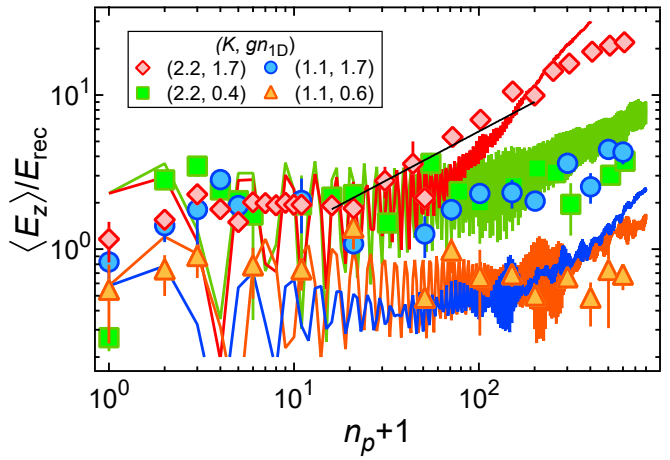

Figure 5.12: Tuning delocalization dynamics with atom numbers. The plot shows the mean energy as a function of pulse number using different number densities in vertical tubes of $s_\perp = 105$ and $g = 1.3$. The kick parameters are $(t_p, T) = (3.5, 40)\,\mu$s and $\bar{k} = 2.0$. The colored solid lines are numerical simulations using the mean-field approach, and the black solid line is a power-law fit that returns an exponent value of 0.63.

5.5 Summary and Outlook

We have observed dynamical delocalization in a kicked one-dimensional ultracold gas in the presence of interactions. Shedding experimental light on prior conflicting theoretical work, we have observed that interactions do indeed destroy dynamical localization and systematically studied it within our parameter space. We have found that the delocalization dynamics are sub-diffusive with the onset of delocalization happening earlier with a larger kick strength or interaction strength. However, we have not observed a clear dependence of the sub-diffusive exponent on the kick strength or interaction strength. Our numerical simulations using the mean-field approach capture the dynamics well except around the transition boundary of the localization-delocalization phase. In the future, we can further investigate and characterize the dynamics around the phase transition where we observe that the mean-field theory fails. It will also be interesting to study a kicked Tonks-Girardeau gas, where the strongly-interacting 1D bosonic gas is fermionized and predicted to be dynamically localized [35].

Chapter 6

INTERACTION-DRIVEN DYNAMICAL DELOCALIZATION OF THE MOMENTUM-SPACE ANDERSON INSULATOR

The flexibility of the quantum kicked rotor allows the engineering of higher dimensional Anderson models. This chapter will first explain how we modify the quantum kicked rotor to a quasiperiodic kicked rotor (QPKR) to simulate a higher dimensional Anderson model. We will then present our observation of the interaction-driven delocalization of the momentum-space Anderson insulator. We will describe how the sub-diffusive delocalization dynamics depend on the different experimental parameters and show the Anderson transition in the presence of interactions. Finally, we will show that the interaction effects are similar in 1D to 4D Anderson models for our experimental parameters.

This chapter reports on the results currently in preparation for publication: J. H. See Toh *et al.* "Interaction-driven delocalization of the Anderson insulator". The theoretical mean-field modeling is performed by our theory collaborators – Mengxin Du, Ying Su, and Chuanwei Zhang at The University of Texas at Dallas.

6.1 Simulating Higher Dimensional Anderson Model

The Anderson model shows that a particle in a 1D or 2D disordered medium will always be localized due to quantum interference, but can be localized or delocalized in a 3D disordered medium. The Anderson metal-insulator transition has been observed using QPKR that simulates a non-interacting 3D (or higher D) Anderson model [27, 29, 41]. Extensive experiments with ultracold atoms in spatially quasiperiodic lattices in one dimension have also observed localization and delocalization in the presence of interaction [70, 72, 74, 79, 80]. However, the effect of interactions on the higher-dimensional momentum-space Anderson

insulator has not been studied so far. We will describe in this section how we engineer the higher-dimensional Anderson model.

The greatest advantage of simulating the Anderson model in the synthetic momentum space is the flexibility to scale up the dimension. This can be easily achieved by simply modulating the amplitude of the kick pulses with incommensurate frequencies. Generalizing the mapping between the QKR Hamiltonian and the Anderson model, a d-dimensional Anderson model can be engineered by using $d-1$ incommensurate modulation frequencies [29, 81–84]. In this chapter, we will focus on the three-dimensional Anderson model where the modulated kick strength of the quasiperiodic kicked rotor (QPKR) is

$$K(t) = K(1 + \epsilon \cos \omega_2 t \cos \omega_3 t) \tag{6.1}$$

where ω_2 and ω_3 (in unit of $1/T$) are the modulation frequencies and ϵ is the modulation strength. To avoid quantum resonances, $(\hbar, \omega_2, \omega_3, \pi)$ must be incommensurate with each other. Figure 6.1 shows a plot of the modulated kick strength with $\omega_2 = 2\pi \times \sqrt{2}, \omega_2 = 2\pi \times \sqrt{3}$ and $\epsilon = 1$. Similar to the 1D case, the pulses are generated by triggering a function generator in burst mode. An aliased function of the modulated kick strength is used for the trigger function to reduce the amplitude fluctuation during each pulse. The fast amplitude response of the IQ modulator that drives the lattice AOM also plays a crucial role here to achieve kick strengths to the desired accuracy.

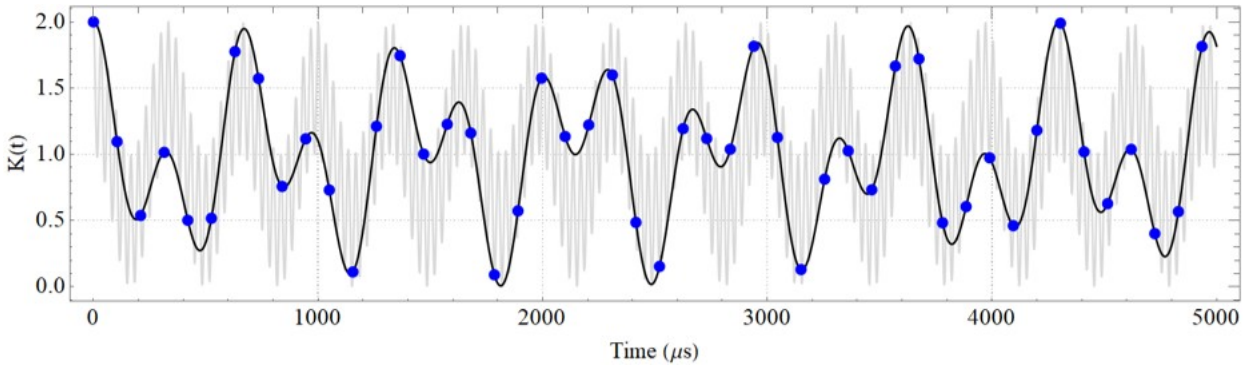

Figure 6.1: Kick-strength modulation to engineer a 3D Anderson model. The grey solid line shows the function of the modulated kick strength with $\omega_2 = 2\pi \times \sqrt{2}, \omega_3 = 2\pi \times \sqrt{3}$ and $\epsilon = 1$. The blue points show the kick strength of the pulses at every kick period $T = 105\,\mu$s. The black solid line shows the aliased function we use to trigger the function generator.

6.2 Dynamical Delocalization of the 3D Anderson Model

In this section, we will present our observation of dynamical delocalization of the 3D Anderson insulator in the synthetic momentum space. The experimental setup is the same as the 1D QKR experiment presented in the previous chapter; the only difference is the amplitude-modulated kick pulses as discussed in the last section. The BEC is loaded into the two-dimensional lattice and the interaction strength is controlled through the transverse confinement of the lattice.

The system can be modeled using the mean-field GP equation

$$i\hbar\partial_\tau\Phi(\theta,\tau) = \left(-\frac{\hbar^2}{2}\partial_\theta^2+\frac{1}{2}\omega_\theta^2\theta^2+g|\Phi(\theta,\tau)|^2-K(1+\epsilon\cos\omega_2\tau\cos\omega_3\tau)\cos\theta\sum_{n_p}\delta(\tau-n_p)\right)\Phi(\theta,\tau) \tag{6.2}$$

where the kick strength is now modulated with two additional incommensurate frequencies ω_2 and ω_3. For all of the 3D Anderson model experiments, we use $\omega_2 = 2\pi \times \sqrt{2}$, $\omega_3 = 2\pi \times \sqrt{3}$, $t_p = 4\,\mu$s, and $T = 105\,\mu$s, as shown in Fig. 6.2a.

The absorption images in Figure 6.2(b-c) show our observation of interaction-driven

delocalization of the momentum-space Anderson insulator. With weak interaction strength $gn_{1D} = 3.9$, the momentum distribution of the atoms freezes after some kicks, and the energy of the system (Fig. 6.2d) saturates at $1.5E_{rec}$. However, with strong interaction strength, the momentum distribution of the atoms becomes wider with increasing pulse number and the energy of the system grows sub-diffusively.

Next, we further investigate the sub-diffusive dynamics of the interaction-driven delocalization with different experimental parameters. Figure 6.3a shows the evolution of the axial kinetic energy for three different interaction strengths with fixed kick strength $K = 2.5$ and modulation strength $\epsilon = 0.4$. The $gn_{1D} = 3.9$ case corresponds to the BEC in the optical dipole trap ($s_\perp = 0$), while the $gn_{1D} = 12.2$ and 17.6 cases correspond to the BEC in the two-dimensional lattice of depth $s_\perp = 30$ and 90, respectively. As the interaction strength is increased, the system goes from localized to delocalized, indicating interaction-driven dynamical delocalization. Figure 6.3b shows that in the presence of interactions, stronger modulation strength ϵ leads to an earlier onset time of delocalization and higher axial kinetic energy at later times. Similar behavior is also observed when we tune the kick strength K, as shown in Figure 6.3c. The onset time of delocalization changes drastically by one order of magnitude when the kick strength is changed from $K = 1$ to $K = 4$. We fit a power law $E_0 n_p^\alpha$ to the delocalization data to extract the exponent α. The measured exponents are in the range of $0.6 - 1.0$, with no obvious functional dependence on any of the experimental parameters.

We define the onset time of delocalization n_p^* to be when the system energy reaches $2.5E_{rec}$, i.e. $E_0(n_p^*)^\alpha = 2.5E_{rec}$. To study how the onset time of delocalization depends on the interaction strength and kick strength, we measure the evolution of the axial energy at two fixed pulse numbers n_p=30 and 100 while varying gn_{1D} or K, as shown in Figure 6.4(a-b). From the measured energy, we can then extract the prefactor E_0 and exponent α, and solve for n_p^*, as shown in Figure 6.4(c). Consistent with what we observed in Figure 6.3, the onset time of delocalization is earlier with stronger interaction strength or kick strength. We fit inverse power law $1/gn_{1D}^p$ to the data in Fig. 6.4(c). We measure $p \simeq 2$, in contrast

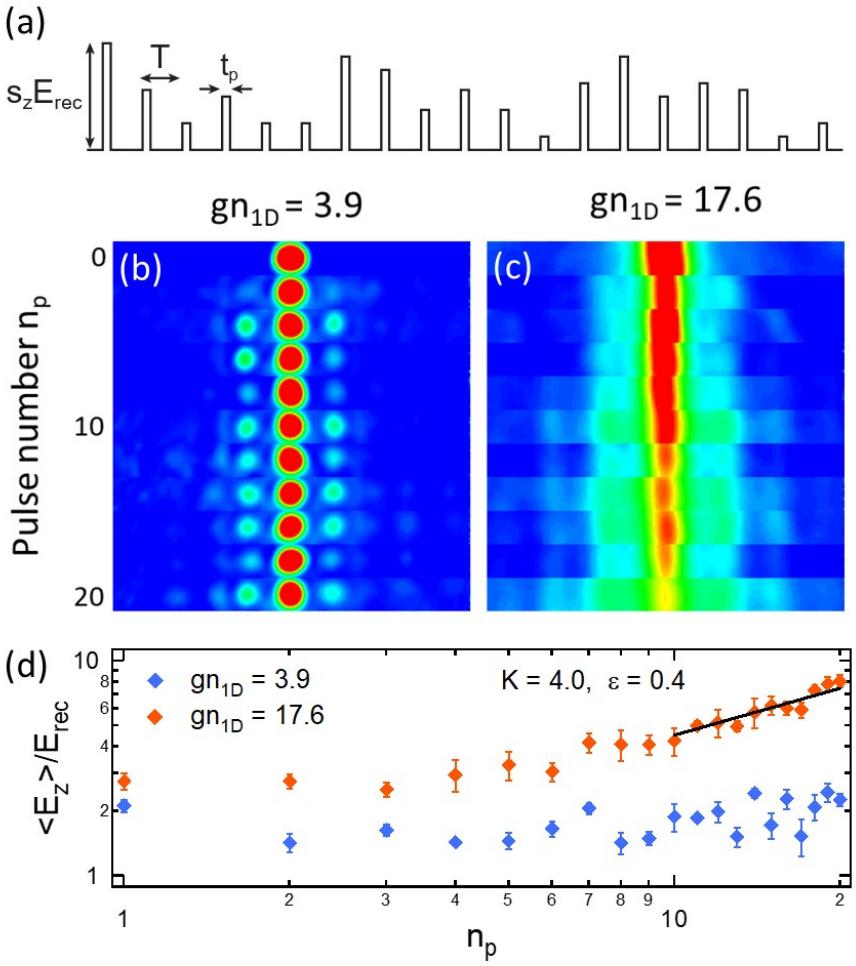

Figure 6.2: Observation of interaction-driven delocalization of the 3D momentum-space Anderson insulator. (a) Experimental sequence of the modulated kick pulses with $t_p = 4\,\mu$s, $T = 105\,\mu$s, $\omega_2 = 2\pi \times \sqrt{2}, \omega_3 = 2\pi \times \sqrt{3}, \bar{k} = 5.26, K = 4, \epsilon = 0.4$ (not to scale). (b-c) Sequences of absorption images for (b) localized and (c) delocalized cases with different interaction strengths. (d) Evolution of the axial kinetic energy corresponding to the data in (b) and (c). The solid line is a power-law fit with an exponent of 0.72.

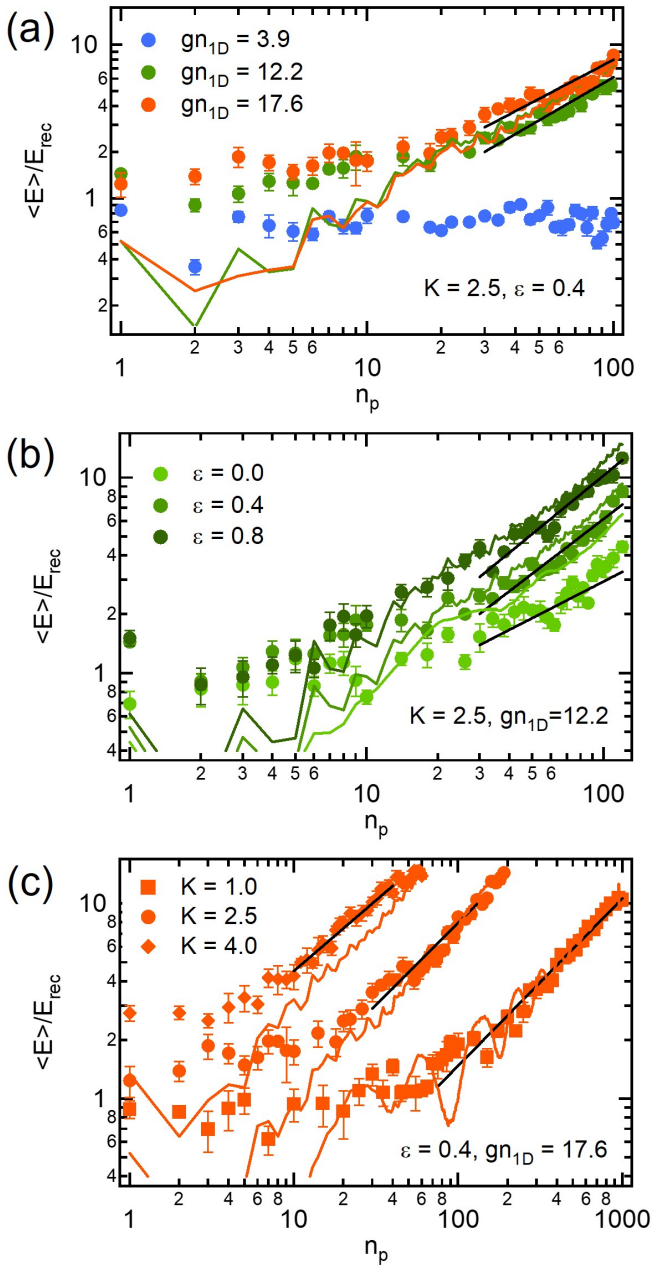

Figure 6.3: Delocalization dynamics with different experimental parameters. The plot shows the evolution of the axial kinetic energy $\langle E_z \rangle$ with pulse number n_p with different (a) interaction strengths gn_{1D}, (b) modulation strengths ϵ, and (c) kick strengths K. The colored solid lines are the corresponding numerical simulation using the GP equation. The black solid lines are power-law fits to the data.

to the prediction of $p = 1$ in Ref. [41]. This is because our interactions are in the position space instead of the momentum space considered in Ref. [41].

The divergence of n_p^* in Fig. 6.4(d) indicates the metal-insulator transition as the kick strength is varied. Using a critical exponent $\nu = 1.59$ numerically established in Ref. [29] for a non-interacting system, we find that the onset time satisfies $n_p^* \simeq 1/|(K - K_c)|^\nu$ with $K_c = 1.6$ with the critical kick strength K_c demarcating the metal-insulator transition. Leaving the critical exponent as a free parameter, our fit returns $\nu = 1.9$ and $K_c = 1.4$. The difference hints at how interactions alter second-order phase transition and could be interesting for future work.

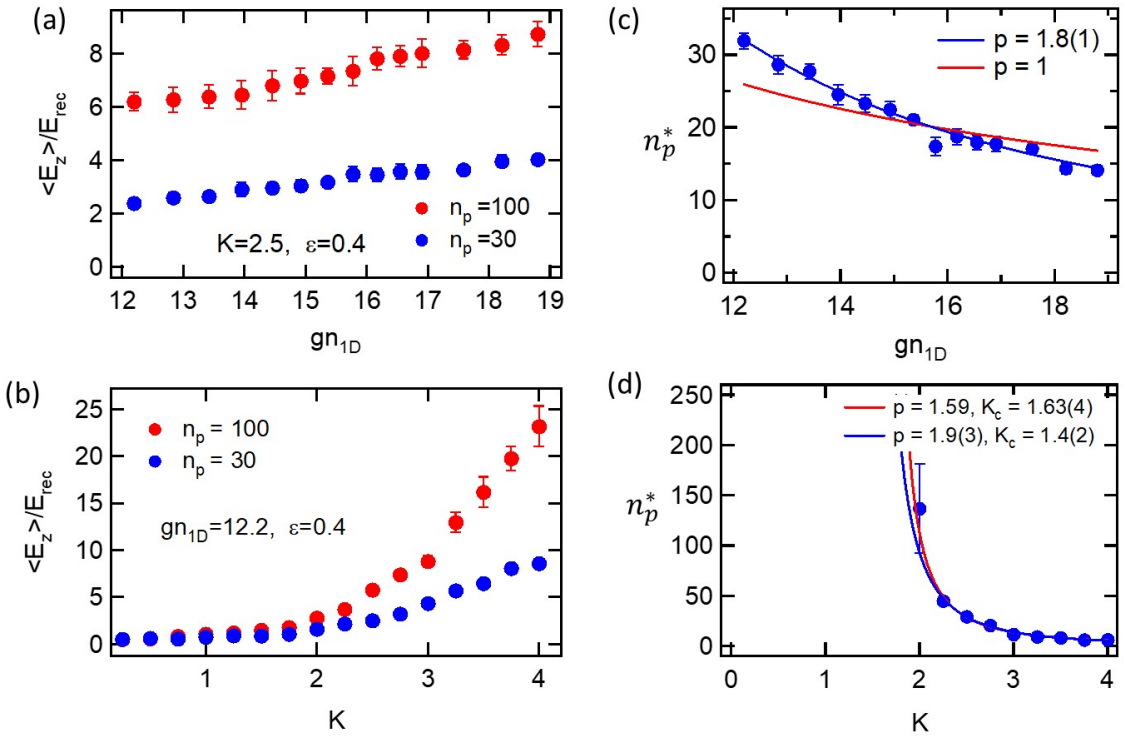

Figure 6.4: Onset of delocalization. (a-b) Evolution of the axial kinetic energy with varying (a) interaction strengths gn_{1D}, and (b) kick strengths K at two different fixed pulse numbers $n_p = 30$ and 100. (c-d) The onset time of delocalization n_p^* calculated from the corresponding data in (a) and (b) respectively. The solid lines are inverse power-law fits with an exponent p.

6.3 d-dimensional Interaction-driven Delocalization

We also compare the interaction-driven delocalization of the d-dimensional Anderson model in the synthetic momentum space from $d = 1$ to $d = 4$. In Figure 6.5, we plot the modulated kick strength using different incommensurate frequencies for different dimensions. The frequencies are chosen such that they give low saturation energy in a localized system, but the choice would not affect the generality of the dynamics [85] as long as they are incommensurate with each other.

Figure 6.6 shows the interaction-driven delocalization of the engineered Anderson insulators in different dimensions $d = 1 - 4$. The interaction $gn_{1\mathrm{D}} = 17.6$ used is strong enough to dominate the system dynamics irrespective of the dimensionality. The measured subdiffusive exponents are in the range of $0.58 - 0.83$ and do not have a clear dependence on the dimension d. It will be interesting in the future to investigate the behavior versus d at reduced values of interaction strength when variations with d have emerged.

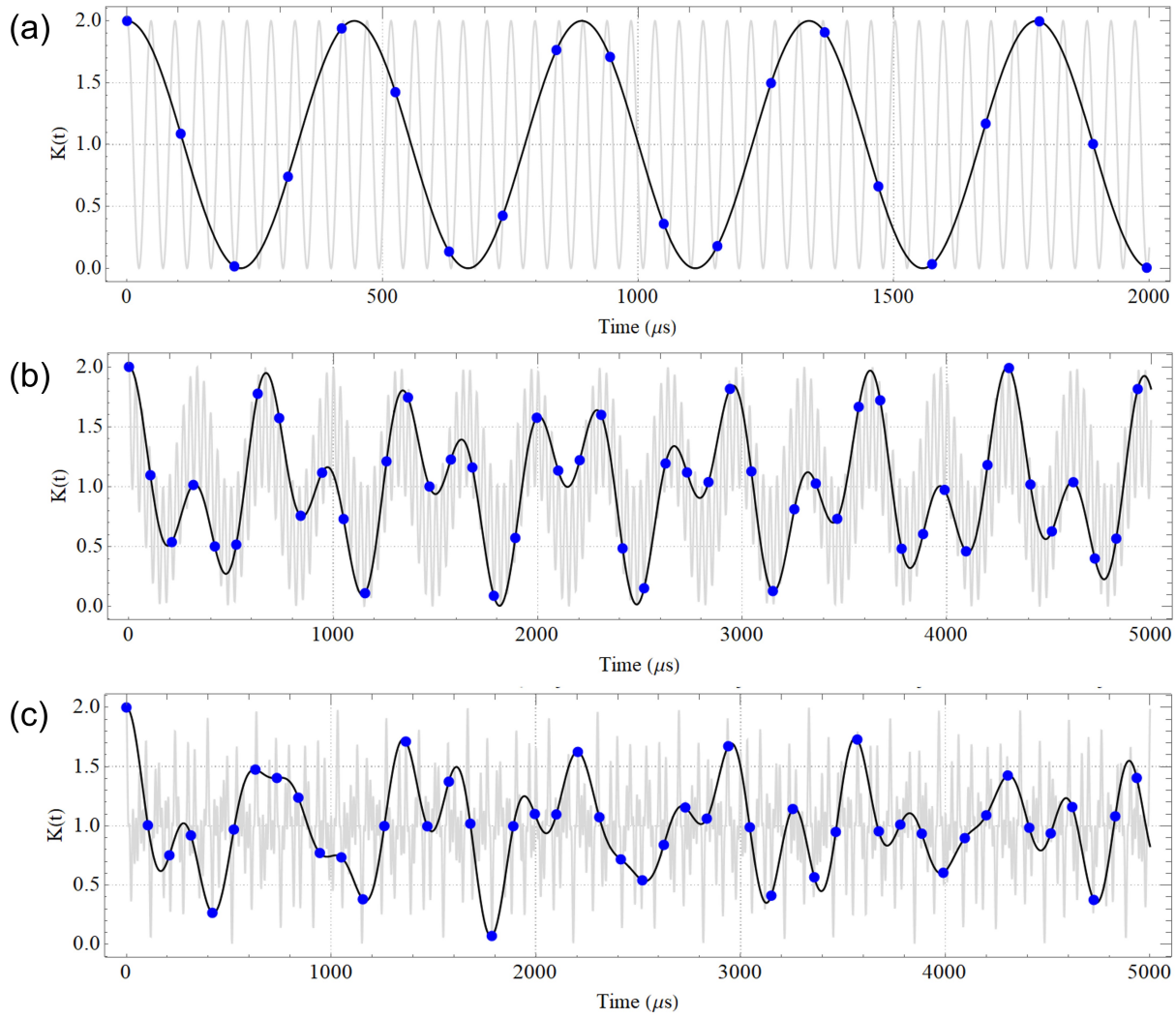

Figure 6.5: Modulated kick strengths for engineering higher-dimensional Anderson models. The plots show some examples of the modulated kick strength with $\epsilon = 1$ used for (a) $d = 2$, (b) $d = 3$, and (c) $d = 4$ Anderson models. For $d = 2$, $\omega_2 = 2\pi \times \sqrt{5}$. For the $d = 3$ case, $\omega_2 = 2\pi \times \sqrt{2}, \omega_3 = 2\pi \times \sqrt{3}$. For the $d = 4$ case, $\omega_2 = 2\pi \times \sqrt{3}, \omega_3 = 2\pi \times \sqrt{5}, \omega_4 = 2\pi \times \sqrt{7}$. The faint grey lines are the functions of the modulated kick strength. The blue points mark the kick strength of the pulses at every kick period $T = 105\,\mu$s. The black lines are the aliased functions we use to trigger the function generator.

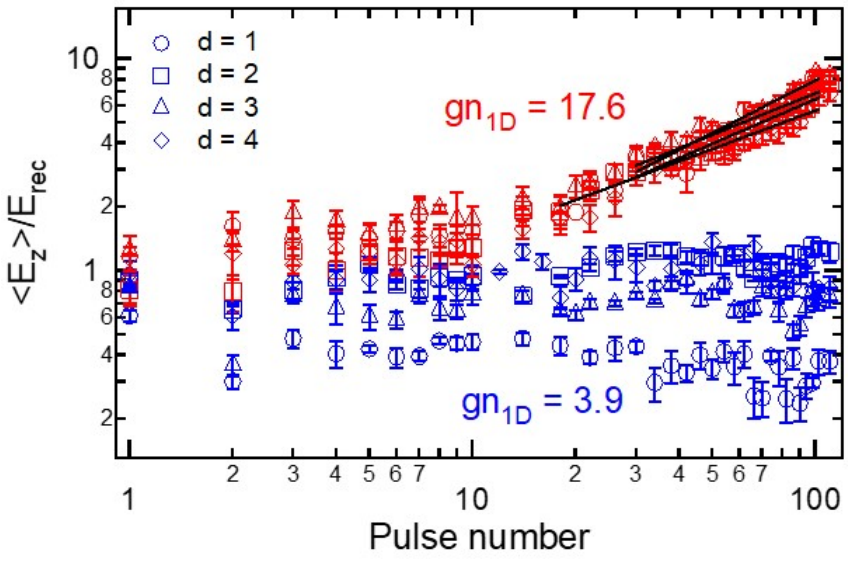

Figure 6.6: Interaction-driven delocalization in d-dimensional Anderson models in the synthetic momentum space. Evolution of the axial kinetic energy for the $d = 1-4$ Anderson models with weak interaction (red) and strong interaction (blue). For all cases, $t_p = 4\,\mu$s, $T = 105\,\mu$s, $\epsilon = 0.4$. The black solid lines are power-law fits $E = E_0 n_p^{\alpha}$ with fitted exponent $\alpha = \{0.65, 0.70, 0.83, 0.58\}$ for $d = \{1, 2, 3, 4\}$, respectively.

.

6.4 Summary and Outlook

Using the flexibility of the QPKR, we engineer the 3D Anderson model in the synthetic momentum space and observe the interaction-driven melting of the Anderson insulator. We study the delocalization behavior with different experimental parameters and find that the although the delocalization dynamics are sub-diffusive, there is no clear functional dependence of the diffusive exponents on the various parameters used. However, we verify that the onset time of delocalization is earlier with larger $gn_{1\mathrm{D}}, K$, or ϵ, and observe a clear phase transition with varying K in the presence of interactions. We also show that interactions can lead to dynamical delocalization in $d = 1 - 4$ Anderson models. Some potential future works include detailed studies of the dynamics across the phase transition and the interplay between dimensionality and interactions in the Anderson problem.

Chapter 7

CONCLUSIONS AND OUTLOOK

The work in this thesis has demonstrated that interactions destroy dynamical localization, inducing subdiffusive dynamics. Using a quantum kicked rotor setup on a 1D gas (thus suppressing transverse dynamics), we engineered the Anderson model up to $d = 4$ in the synthetic momentum space and examined the delocalization dynamics with different experimental parameters. Our measured values of the subdiffusion exponent are not universal and also do not show any systematic dependence on experimental parameters. However, we observed that delocalization starts earlier with stronger interactions, kicks, and modulations. Our work sheds light on interaction-driven transport in a disordered medium. We hope that our work will motivate further theoretical and experimental work on this interesting problem.

The difference between our observations and several theoretical predictions demands a better understanding of interaction-driven delocalization dynamics. The failure of mean-field theory to describe the dynamics close to the localization-delocalization transition boundary suggests richer underlying many-body physics. More experimental work on the transition is also needed to investigate if there is a novel critical phenomenon in the presence of interactions. The apparent random distribution of the subdiffusion exponents could also be studied in larger parameter space.

While the limited laser power and the lack of Feshbach resonance in Yb restrict us to a finite range of interaction strength, the intertube tunneling at low lattice depth also prevents us from finding out the critical interaction strength that triggers delocalization. The axial confinement of the tubes also limits how long we can kick the system. One can improve the setup by expanding the beam size of the lattice beam to reduce axial confinement. The ODT alignment and center-position modulation can also be optimized to produce a BEC with a

larger cross-sectional area to allow more tubes to be loaded. These improvements will reduce the atom number density in each tube for the same lattice depth and allow better control around the critical interaction strength. One could also consider using another atom species with a Feshbach resonance that enables more control of the interaction strength. In fact, this has been done concurrently with our work by the Weld group at the University of Santa Barbara and similar observations were made [86]. Although the use of Feshbach resonance obviates the need for a two-dimensional lattice, unwanted chemistry and dynamics in the transverse direction may deteriorate the signal. We think that combining the advantages of great control of scattering length using a Feshbach resonance and the suppressed transverse dynamics in 1D tubes is a promising way to systematically study the delocalization dynamics in a much larger parameter space. Even more ideally, a 1D ring geometry should be used, where spatial diffusion effects are removed. This will also permit one to study if a kicked Tonks-Girardeau gas will remain localized.

Our machine also supports experiments with ^{6}Li, which has a broad Feshbach resonance around 832 G . The lab is currently reviving the Li setup and attempting to study dynamical delocalization around the BEC-BCS crossover. The change in the effective mass of the particles across the crossover may lead to more exciting phenomena. One could also consider loading Li into the optical lattice, which would also open up other experiment possibilities such as the study of the Fermi-Hubbard model.

BIBLIOGRAPHY

[1] F. Bloch, Über die quantenmechanik der elektronen in kristallgittern, Z. Physik **52**, 555–600 (1929).

[2] P. W. Anderson, Absence of diffusion in certain random lattices, Phys. Rev. **109**, 1492–1505 (1958).

[3] A. Aspect and M. Inguscio, Anderson localization of ultracold atoms, Physics Today **62**, 30 (2009).

[4] D. Wiersma, P. Bartolini, A. Lagendijk, *et al.*, Localization of light in a disordered medium, Nature **390**, 671 (1997).

[5] M. Störzer, P. Gross, C. M. Aegerter, and G. Maret, Observation of the critical regime near Anderson localization of light, Phys. Rev. Lett. **96**, 063904 (2006).

[6] T. Schwartz, G. Bartal, S. Fishman, *et al.*, Transport and Anderson localization in disordered two-dimensional photonic lattices, Nature **446**, 52 (2007).

[7] S. Faez, A. Strybulevych, J. H. Page, *et al.*, Observation of multifractality in Anderson localization of ultrasound, Phys. Rev. Lett. **103**, 155703 (2009).

[8] J.-C. Garreau, Quantum simulation of disordered systems with cold atoms, Comptes Rendus Physique **18**, 31–46 (2017).

[9] C. Guan and X. Guan, A brief introduction to Anderson localization (2019).

[10] E. Abrahams, P. W. Anderson, D. C. Licciardello, and T. V. Ramakrishnan, Scaling theory of localization: Absence of quantum diffusion in two dimensions, Phys. Rev. Lett. **42**, 673–676 (1979).

[11] I. Bloch, J. Dalibard, and S. Nascimbène, Quantum simulations with ultracold quantum gases, Nature Physics **8**, 267–276 (2012).

[12] C. Gross and I. Bloch, Quantum simulations with ultracold atoms in optical lattices, Science **357**, 995–1001 (2017).

[13] G. Roati, C. D'Errico, L. Fallani, *et al.*, Anderson localization of a non-interacting Bose-Einstein condensate, Nature **453**, 895–898 (2008).

[14] D. H. White, T. A. Hasse, D. J. Brown, *et al.*, Observation of two-dimensional Anderson localization of ultracold atoms, Nature Communications **11**, 4942 (2020).

[15] F. Jendrzejewski, A. Bernard, K. Müller, *et al.*, Three-dimensional localization of ultracold atoms in an optical disordered potential, Nature Physics **8**, 398–403 (2012).

[16] D. Steck, *Quantum chaos, transport, and decoherence in atom optics*, PhD thesis, University of Texas at Austin (2001).

[17] T.-Y. Li and J. A. Yorke, Period three implies chaos, Am. Math. Monthly **82**, 985 (1975).

[18] E. Lorenz, Deterministic nonperiodic flow, Journal of the Atmospheric Sciences **20**, 103–141 (1963).

[19] F. L. Moore, J. C. Robinson, C. Bharucha, P. E. Williams, and M. G. Raizen, Observation of dynamical localization in atomic momentum transfer: A new testing ground for quantum chaos, Phys. Rev. Lett. **73**, 2974–2977 (1994).

[20] F. L. Moore, J. C. Robinson, C. F. Bharucha, B. Sundaram, and M. G. Raizen, Atom optics realization of the quantum δ-kicked rotor, Phys. Rev. Lett. **75**, 4598–4601 (1995).

[21] H. Ammann, R. Gray, I. Shvarchuck, and N. Christensen, Quantum delta-kicked rotor: Experimental observation of decoherence, Phys. Rev. Lett. **80**, 4111–4115 (1998).

[22] M. B. d'Arcy, R. M. Godun, M. K. Oberthaler, D. Cassettari, and G. S. Summy, Quantum enhancement of momentum diffusion in the delta-kicked rotor, Phys. Rev. Lett. **87**, 074102 (2001).

[23] S. Wimberger, I. Guarneri, and S. Fishman, Quantum resonances and decoherence for δ-kicked atoms, Nonlinearity **16**, 1381–1420 (2003).

[24] A. Ullah, S. Reddel, J. Currivan, and M. D. Hoogerland, Quantum resonant effects in the delta-kicked rotor revisited, Eur. Phys. J. D **66** (2012).

[25] G. J. Duffy, S. Parkins, T. Müller, M. Sadgrove, R. Leonhardt, and A. C. Wilson, Experimental investigation of early-time diffusion in the quantum kicked rotor using a Bose-Einstein condensate, Phys. Rev. E **70**, 056206 (2004).

[26] D. H. White, S. K. Ruddell, and M. D. Hoogerland, Phase noise in the delta kicked rotor: from quantum to classical, New Journal of Physics **16**, 113039 (2014).

[27] J. Chabé, G. Lemarié, B. Grémaud, D. Delande, P. Szriftgiser, and J. C. Garreau, Experimental observation of the Anderson metal-insulator transition with atomic matter waves, Phys. Rev. Lett. **101**, 255702 (2008).

[28] C. Hainaut, A. Rançon, J.-F. Clément, I. Manai, P. Szriftgiser, D. Delande, J. C. Garreau, and R. Chicireanu, Experimental realization of an ideal floquet disordered system, New Journal of Physics **21**, 035008 (2019).

[29] G. Lemarié, J. Chabé, P. Szriftgiser, J. C. Garreau, B. Grémaud, and D. Delande, Observation of the Anderson metal-insulator transition with atomic matter waves: Theory and experiment, Phys. Rev. A **80**, 043626 (2009).

[30] G. Lemarié, H. Lignier, D. Delande, P. Szriftgiser, and J. C. Garreau, Critical state of the Anderson transition: Between a metal and an insulator, Phys. Rev. Lett. **105**, 090601 (2010).

[31] S. Fishman, D. R. Grempel, and R. E. Prange, Chaos, quantum recurrences, and anderson localization, Phys. Rev. Lett. **49**, 509–512 (1982).

[32] N. Brenner and S. Fishman, Pseudo-randomness and localization, Nonlinearity **5**, 211–235 (1992).

[33] M. Saunders, P. L. Halkyard, K. J. Challis, and S. A. Gardiner, Manifestation of quantum resonances and antiresonances in a finite-temperature dilute atomic gas, Phys. Rev. A **76**, 043415 (2007).

[34] S. Wimberger and M. Sadgrove, The role of quasi-momentum in the resonant dynamics of the atom-optics kicked rotor, Journal of Physics A: Mathematical and General **38**, 10549–10557 (2005).

[35] C. Rylands, E. B. Rozenbaum, V. Galitski, and R. Konik, Many-body dynamical localization in a kicked lieb-liniger gas, Phys. Rev. Lett. **124**, 155302 (2020).

[36] R. Chicireanu and A. Rançon, Dynamical localization of interacting bosons in the few-body limit, Phys. Rev. A **103**, 043314 (2021).

[37] D. L. Shepelyansky, Delocalization of quantum chaos by weak nonlinearity, Phys. Rev. Lett. **70**, 1787–1790 (1993).

[38] G. Gligorić, J. D. Bodyfelt, and S. Flach, Interactions destroy dynamical localization with strong and weak chaos, EPL (Europhysics Letters) **96**, 30004 (2011).

[39] A. Russomanno, M. Fava, and R. Fazio, Chaos and subdiffusion in infinite-range coupled quantum kicked rotors, Phys. Rev. B **103**, 224301 (2021).

[40] S. Lellouch, A. Rançon, S. De Bièvre, D. Delande, and J. C. Garreau, Dynamics of the mean-field-interacting quantum kicked rotor, Phys. Rev. A **101**, 043624 (2020).

[41] N. Cherroret, B. Vermersch, J. C. Garreau, and D. Delande, How nonlinear interactions challenge the three-dimensional Anderson transition, Phys. Rev. Lett. **112**, 170603 (2014).

[42] F. M. Izrailev and D. L. Shepelyanskii, Quantum resonance for a rotator in a nonlinear periodic field, Theoretical and Mathematical Physics **43**, 553–561 (1980).

[43] C. Foot, *Atomic Physics* (Oxford University Press, 2005).

[44] R. Roy, A. Green, R. Bowler, and S. Gupta, Rapid cooling to quantum degeneracy in dynamically shaped atom traps, Phys. Rev. A **93**, 043403 (2016).

[45] R. Roy, *Ytterbium and Lithium Quantum Gases: Heteronuclear Molecules and Bose-Fermi Superfluid Mixtures*, PhD thesis, University of Washington (2017).

[46] M. Greiner, *Ultracold quantum gases in three-dimensional optical lattice potentials*, PhD thesis, Ludwig-Maximilians-Universität München (2003).

[47] D. S. Petrov, G. V. Shlyapnikov, and J. T. M. Walraven, Regimes of quantum degeneracy in trapped 1d gases, Phys. Rev. Lett. **85**, 3745–3749 (2000).

[48] M. Olshanii, Atomic scattering in the presence of an external confinement and a gas of impenetrable bosons, Phys. Rev. Lett. **81**, 938–941 (1998).

[49] T. Kinoshita, T. Wenger, and D. Weiss, Observation of a one-dimensional tonks-girardeau gas, Science **305**, 1125–1128 (2004).

[50] B. Paredes, A. Widera, V. Murg, O. Mandel, S. Folling, I. Cirac, G. Shlyapnikov, T. Hansch, and I. Bloch, Tonks–girardeau gas of ultracold atoms in an optical lattice, Nature **429**, 277–281 (2004).

[51] P. L. Kapitza and P. A. M. Dirac, The reflection of electrons from standing light waves, Mathematical Proceedings of the Cambridge Philosophical Society **29**, 297â300 (1933).

[52] S. Gupta, A. E. Leanhardt, A. D. Cronin, and D. E. Pritchard, Coherent manipulation of atoms with standing light waves, C. R. Acad. Sci.- IV - Phys. **2**, 479–495 (2001).

[53] D. Gochnauer, *Vertical Contrast Interferometry and Bloch-Band Approach to Atom Optics*, PhD thesis, University of Washington (2020).

[54] A. Hansen, *Interacting Quantum Gases of Lithium and Ytterbium*, PhD thesis, University of Washington (2013).

[55] M. Greiner, O. Mandel, T. Esslinger, *et al.*, Quantum phase transition from a superfluid to a Mott insulator in a gas of ultracold atoms, Nature **415**, 39–44 (2002).

[56] I. Bloch, J. Dalibard, and W. Zwerger, Many-body physics with ultracold gases, Rev. Mod. Phys. **80**, 885–964 (2008).

[57] J. J. García-Ripoll and J. I. Cirac, Quantum computation with cold bosonic atoms in an optical lattice, Philosophical Transactions: Mathematical, Physical and Engineering Sciences **361**, 1537–1548 (2003).

[58] X. Zhang and J. Ye, Precision measurement and frequency metrology with ultracold atoms, National Science Review **3**, 189–200 (2016).

[59] A. Kobyakov, M. Sauer, and D. Chowdhury, Stimulated brillouin scattering in optical fibers, Adv. Opt. Photon. **2**, 1–59 (2010).

[60] H. A. Gersch and G. C. Knollman, Quantum cell model for bosons, Phys. Rev. **129**, 959–967 (1963).

[61] M. P. A. Fisher, P. B. Weichman, G. Grinstein, and D. S. Fisher, Boson localization and the superfluid-insulator transition, Phys. Rev. B **40**, 546–570 (1989).

[62] D. Jaksch, C. Bruder, J. I. Cirac, C. W. Gardiner, and P. Zoller, Cold bosonic atoms in optical lattices, Phys. Rev. Lett. **81**, 3108–3111 (1998).

[63] L. Pitaevskii and S. Stringari, Bose-Einstein condensation and superfluidity (Oxford University Press, 2016).

[64] J. H. See Toh, K. C. McCormick, X. Tang, *et al.*, Many-body dynamical delocalization in a kicked one-dimensional ultracold gas, Nature Physics **18**, 1297–1301 (2022).

[65] M. Berry, I. Marzoli, and W. Schleich, Quantum carpets, carpets of light, Physics World **14**, 39 (2001).

[66] A. Lichtenberg and M. Lieberman, *Regular and Chaotic Dynamics* (Springer, New York, 1992).

[67] B. V. Chirikov, A universal instability of many-dimensional oscillator systems, Physics Reports **52**, 263–379 (1979).

[68] D. R. Grempel, R. E. Prange, and S. Fishman, Quantum dynamics of a nonintegrable system, Phys. Rev. A **29**, 1639–1647 (1984).

[69] B. Gadway, J. Reeves, L. Krinner, and D. Schneble, Evidence for a quantum-to-classical transition in a pair of coupled quantum rotors, Phys. Rev. Lett. **110**, 190401 (2013).

[70] M. Schreiber, S. S. Hodgman, P. Bordia, H. P. Lüschen, M. H. Fischer, R. Vosk,

E. Altman, U. Schneider, and I. Bloch, Observation of many-body localization of interacting fermions in a quasirandom optical lattice, Science **349**, 842 – 845 (2015).

[71] D. A. Abanin, E. Altman, I. Bloch, and M. Serbyn, Colloquium: Many-body localization, thermalization, and entanglement, Rev. Mod. Phys. **91**, 021001 (2019).

[72] A. Lukin, M. Rispoli, R. Schittko, *et al.*, Probing entanglement in a many-body-localized system, Science **364**, 256 – 260 (2019).

[73] C. Zhang, J. Liu, M. G. Raizen, and Q. Niu, Transition to instability in a kicked Bose-Einstein condensate, Phys. Rev. Lett. **92**, 054101 (2004).

[74] B. Deissler, M. Zaccanti, G. Roati, C. DâErrico, M. Fattori, M. Modugno, G. Modugno, and M. Inguscio, Delocalization of a disordered bosonic system by repulsive interactions, Nature Phys. **6**, 354 – 358 (2010).

[75] A. S. Pikovsky and D. L. Shepelyansky, Destruction of Anderson localization by a weak nonlinearity, Phys. Rev. Lett. **100**, 094101 (2008).

[76] S. Flach, D. O. Krimer, and C. Skokos, Universal spreading of wave packets in disordered nonlinear systems, Phys. Rev. Lett. **102**, 024101 (2009).

[77] S. Notarnicola, A. Silva, R. Fazio, and A. Russomanno, Slow heating in a quantum coupled kicked rotors system, Journal of Statistical Mechanics: Theory and Experiment **2020**, 024008 (2020).

[78] V. Vuatelet and A. Rançon, Effective thermalization of a many-body dynamically localized bose gas, Phys. Rev. A **104**, 043302 (2021).

[79] E. Lucioni, B. Deissler, L. Tanzi, G. Roati, M. Zaccanti, M. Modugno, M. Larcher, F. Dalfovo, M. Inguscio, and G. Modugno, Observation of subdiffusion in a disordered interacting system, Phys. Rev. Lett. **106**, 230403 (2011).

[80] H. P. Lüschen, P. Bordia, S. Scherg, F. Alet, E. Altman, U. Schneider, and I. Bloch, Observation of slow dynamics near the many-body localization transition in one-dimensional quasiperiodic systems, Phys. Rev. Lett. **119**, 260401 (2017).

[81] G. Casati, I. Guarneri, and D. L. Shepelyansky, Anderson transition in a one-dimensional system with three incommensurate frequencies, Phys. Rev. Lett. **62**, 345–348 (1989).

[82] D. Shepelyansky, Some statistical properties of simple classically stochastic quantum systems, Physica D: Nonlinear Phenomena **8**, 208–222 (1983).

[83] E. Doron and S. Fishman, Anderson localization for a two-dimensional rotor, Phys. Rev. Lett. **60**, 867–870 (1988).

[84] J. Wang and A. M. García-García, Anderson transition in a three-dimensional kicked rotor, Phys. Rev. E **79**, 036206 (2009).

[85] G. Lemarié, B. Grémaud, and D. Delande, Universality of the Anderson transition with the quasiperiodic kicked rotor, EPL (Europhysics Letters) **87**, 37007 (2009).

[86] A. Cao, R. Sajjad, H. Mas, *et al.*, Interaction-driven breakdown of dynamical localization in a kicked quantum gas, Nature Physics **18**, 1302–1306 (2022).